Nanoscale Engineering and Characterization of Synthetic and Biological Ferroelectrics

Yuanming Liu

A dissertation

submitted in partial fulfillment of the

requirements for the degree of

Doctor of Philosophy

Reading Committee:

Jiangyu Li, Chair

Guozhong Cao

Jae-Hyun Chung

University of Washington

2012

Program Authorized to Offer Degree: Mechanical Engineering

University of Washington

Abstract

Nanoscale Engineering and Characterization of Synthetic and Biological Ferroelectrics

Yuanming Liu

Chair of the Supervisory Committee:

Associate Professor Jiangyu Li

Department of Mechanical Engineering

The works presented in this dissertation focus on the characterization, manipulation, and engineering of synthetic and biological ferroelectrics using piezoresponse force microscopy (PFM) and nanoimprint lithography (NIL). Various PFM techniques are introduced first, and are then applied to probe and manipulate inorganic perovskite ferroelectric films and crystals, organic polyvinylidene fluoride trifluoroethylene [P(VDF-TrFE)] films and nanostructures, as well as biological aortic walls and elastins. Using these techniques, sophisticated domain structures are imaged, domain switching characteristics are revealed, and biological ferroelectricity is discovered. The principle of scanning probe microscopy (SPM) is introduced briefly first, followed by detailed discussions on PFM. Damped harmonic oscillator model was also used to enable quantitative analysis of PFM signal. The switching of polarization by conductive SPM tip is then demonstrated, PFM hysteresis and butterfly loops characteristics are also obtained.

These PFM techniques are applied to probe inorganic perovskite ferroelectric films and crystals. These studies revealed characteristic domain structures in ferroelectric films and crystals. It also confirmed excellent piezoelectric and ferroelectric properties in PZT

nanostructures and stretchable PZT ribbons that are comparable to the flat PZT films on rigid silicon substrates, making it possible to use these PZT structures in a wide range of applications. We also use PFM to study P(VDF-TrFE) films. The effects of processing parameters on film properties are investigated first, and then the thermal stability of P(VDF-TrFE) polar structures are probed at a series of temperatures across Curie point. It is observed that the piezoresponse remains relatively stable up to 110 ^{o}C, and then drops rapidly to zero. Furthermore, a rapid nanoimprinting technique is also developed to pattern P(VDF-TrFE) copolymers in just 3 minutes without any post-imprinting annealing.

Using PFM, we discovered that the porcine aortic walls are not only piezoelectric, but also ferroelectric, confirmed by tip induced hysteresis and butterfly loops characteristic of polarization reversal. In addition, we also discovered that elastin is switchable by an electric field. Furthermore, it is observed that the ferroelectricity in elastin is largely suppressed by glucose, and such loss of ferroelectricity may have important physiological and pathological implications to elastin's functionalities.

ACKNOWLEDGEMENTS

I would like convey my deep appreciation to my adviser, Jiangyu Li for his guidance over the past five years. His advice has been invaluable, and I am extremely grateful for his patience and insight.

I would like to thank Prof. Guozhong Cao, Prof. Jae-Hyun Chung, and Prof. Qiuming Yu for serving on my supervisory Committee. I am grateful for their careful reading of my dissertation. Special thanks needs to be given to Prof. Yanhang Zhang, Prof. Xiaoqing Pan, and Prof. Xue Feng for their collaboration on the samples. I would also like to thank Dr. Roger Proksch and Jason Li of Asylumresearch for their training in SPM system.

Many thanks go to my co-workers in Multifunctional Materials Laboratory. Also, this dissertation would never have been completed without the encouragement and devotion of my family and friends

LIST OF FIGURES

Table of Contents

Chapter 1 Introduction

1.1 Ferroelectrics

1.1.1 Ferroelectricity

Piezoelectricity was first demonstrated in crystals, such as quartz and Rochelle salt (sodium potassium tartrate tetrahydrate), by Jacques and Pierre Curie in 1880. Valasek[1], who studied the dielectric properties of Rochelle salt in analogy with the magnetic properties of ferromagnetics, suggested the name of 'ferroelectrics' in 1920. Since then, interest in ferroelectrics has grown due to their unique properties in various fields. Today, ferroelectric materials show promise for a wide range of applications, including: sensing[2] and actuation, data storage[3-6], photonics[7], spintronics[8], and energy conversion and storage[9].

Most dielectric materials are polarized linearly by an external electric field, and they can be categorized as either nonferroelectric (normal dielectric or paraelectric) or ferroelectric. In paraelectric materials, electric polarization occurs when an electric field is applied to the materials. If a material possesses spontaneous polarization in the absence of the electric field, it is called a pyroelectric. Some pyroelectric materials can have their spontaneous polarization reversed by the external electric field; these kinds of materials are ferroelectric. Ferroelectric materials have the electric polarization in their equilibrium

states. This spontaneous polarization is also temperature dependent. In general, above the critical temperature, called the phase transition temperature (T_c), the spontaneous polarization disappears. In other words, at T_c, ferroelectric materials undergo a phase transition from the ferroelectric to the paraelectric as temperature increases.

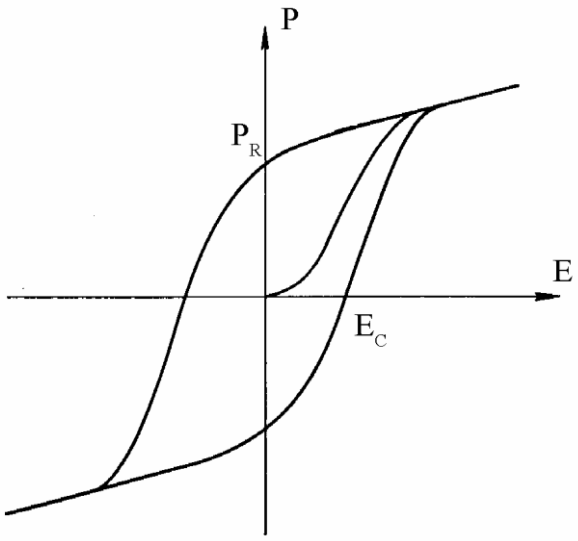

Figure 1.1 Schematics of the ferroelectric (P-E) hysteresis loop[10].

A distinguishing feature of ferroelectric materials is that the direction of the spontaneous polarization can be reversed by an applied electric field, yielding a hysteresis loop, as shown in Figure 1.1[10]. When the external electric field is applied to the ferroelectric material, the response of the polarization initially increases linearly. In this stage, the field is not large enough to switch domains and the response is linear. As the electric field increases further, domains with polarization disfavored by the electric field start to switch as closely as possible to the direction of the field, and the measured

polarization rapidly increases at the same time. Once all of the domains have polarization aligned with the applied field after saturation, the response of the polarization increases linearly again along the electric field. When decreasing the field, some domains will switch back, while others will not, and the polarization maintains a positive value at the zero field, which is called remanent polarization. When a negative electric field of sufficient strength is reached, the nucleation of the reversed polarization begins. The polarization decreases non-linearly until reversed saturation is reached. The field strength is then reduced to zero and completes the cycle. The field necessary to switch the polarization is called the coercive field.

1.1.2 Ferroelectric Materials

Ferroelectric phase transitions are often characterized as either displacive (such as $BaTiO_3$) or order-disorder (such as $NaNO_2$), and phase transitions often demonstrate elements of both behaviors. For barium titanate, if the Ti ion is displaced from equilibrium slightly, the force from the local electric fields, due to the ions in the crystal, increases faster than the elastic-restoring forces; this leads to an asymmetrical shift in the equilibrium ion positions, and hence, a permanent dipole moment.

An important ferroelectric material is *lead zirconate titanate* (PZT), which is a ceramic perovskite material that shows a significant piezoelectric effect. It develops a

voltage when compressed, and deformed when an external electric field is applied due to its piezoelectric character. Meanwhile, PZT will yield a voltage difference across two surfaces under a temperature change by its pyroelectric character. PZT ceramics is wildly used for transducer applications[11-13] because they have many advantages, including: (1) higher electromechanical coupling coefficients and phase transition temperatures, which allow high temperatures operation or higher temperatures processing of devices; (2) low coercive field, making them easily poled; (3) possessing a wide range of dielectric constants; and (4) forming solid-solutions with many different constituents, thus allowing a wide range of achievable properties.

Another class of ferroelectric materials is ferroelectric polymers, such as polyvinylidene fluoride (PVDF) and its copolymers. These materials, first discovered by Kawai[14] in 1969, are crystalline and exhibit clear ferroelectric phase transitions. The vinylidene fluoride monomers form a linear carbon-carbon chain with the structure $-(CH_2-CF_2)-$. For the polymer chains $(CH_2-CF_2)_n$, there are two common stable conformations: all-trans TTTT, and trans-gauche TGTG'. The crystal structure of the all-trans conformation is called β phase, and it is ferroelectric[15]. β phase is an orthorhombic m2m structure with chains along the crystal c-axis and dipoles approximately aligned along the crystal b-axis[16]. The evidence of ferroelectric properties of PVDF came from studying its copolymers with trifluoroethylene (TrFE), which is one of the most

commonly-used copolymers of PVDF. As shown in Figure 1.2, PVDF does not show the ferroelectric-to-paraelectric transition because the Curie temperature is higher than the melting temperature (200 ºC), and as a result, there is no Curie temperature for PVDF. The degree of crystallinity for both α phase and β phase of PVDF is approximately 50%. However, the crystallinity of copolymers of P(VDF-TrFE) can be improved to over 90% by mechanical stretching or electrical polarization. This results in a larger piezoelectric response. The d_{33} values for P(VDF-TrFE) have been recorded to be as high as -38 pC/N.

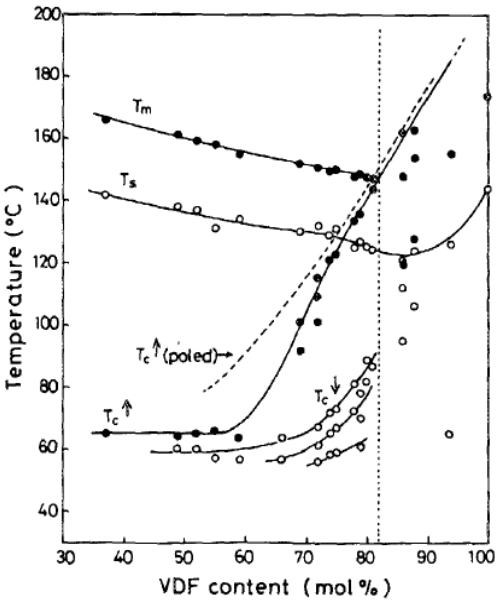

Figure 1.2 Phase transitions versus VDF molar content of copolymer of P(VDF-TrFE).[15]

1.1.3 Ferroelectric Applications

Ferroelectric materials are employed in a vast range of applications, including: accelerometers, electro-optical devices, embedded smart systems, and ferroelectric

random access memories (FeRAMs)[17]. The nonlinear feature of ferroelectric materials can be used in capacitors. The permittivity of ferroelectrics depends on the electric field and can be tuned especially when close to the phase transition temperature. The spontaneous polarization of ferroelectric materials implies a hysteresis effect, which can be used for data storage. Components based on ferroelectric materials could also be developed for various sensor and actuator applications and for tunable microwave circuits.

Thin films of ferroelectric materials are typically used, which allows a small voltage to switch the polarization. Integrated Si and thin film processing stimulated the interests of nonvolatile memories using ferroelectric thin films from the late 1960s[18-20]. To date, ferroelectric films are used in a number of commercial products; these applications include: memories, microwave electronic components, and microdevices with pyroelectric and piezoelectric microsensors/actuators.

1.2 Nanoimprint Lithography

The term ‘nanotechnology’ was originally created by Norio Taniguchi in 1974 to describe the production technology with a very high precision. According to the National Science Foundation and the National Nanotechnology Initiative (NNI), Nanotechnology is the ability to understand, control, and manipulate matter at the atomic and molecular

level. Today, nanotechnology usually indicates research and technology development of structures between 1-100 nm in at least one dimension.

Nanoimprint Lithography (NIL) has emerged as one of the most important techniques to fabricate nanostructures. It was originally developed by Prof. Stephen Chou and his students in 1996, as reported in a paper in Science[21]. After that, researchers and the industry have quickly recognized NIL as a potential low-cost, high throughput lithographic method for a range of applications. After the Science paper, many researchers developed different variations and implementations. NIL has also been added to the International Technology Roadmap for Semiconductors (ITRS) as a next generation lithography candidate for 32 and 22 nm nodes[22]. In the past few years, NIL has been used to fabricate devices for electrical, optical, photonic, and biological applications. For optics and photonics, a number of studies have been conducted using NIL to fabricate sub wavelength resonant grating filters, polarizers, integrated photonics circuits, and plasmontic devices[23]. Sub-10 nm nanofluidic channels, which were used for DNA stretching experiments, have also been fabricated using NIL[24].

Two types of nanoimprint lithography are most common: *thermoplastic nanoimprint lithography* and *photo nanoimprint lithography*[25]. Thermoplastic nanoimprint lithography (T-NIL) is the original nanoimprint lithography developed by Prof. Stephen Chou's

group. In a standard T-NIL process, a thin layer of imprint resist (thermoplastic polymer) is spin coated onto the sample substrate. Then, the mold with designated patterns is brought into contact with the sample, and they are pressed together under certain pressure. When heated above the glass transition temperature of the polymer, the pattern on the mold is pressed into the softened polymer film[21]. The mold is separated from the sample after cooling, and the patterned resist is left on the substrate. Photo-nanoimprint lithography consists of two main steps: imprinting and pattern transfer. The imprint process is usually performed under atmospheric conditions. Ultraviolet (UV) curable liquid resist is applied to the sample substrate and the mold is normally made of a transparent material like quartz. The mold is pressed into the photocurable polymer and UV radiation is then irradiated through the mold while maintaining the imprint pressure, and the resist is cured in UV light and becomes solid. The pattern is obtained after the mold is released.

1.3 Piezoresponse Force Microscopy

The scanning probe microscopy (SPM) based measurements of piezoelectric materials have been used by a number of investigators to probe local properties at the nanoscale. One of the most important derivatives of SPM is piezoresponse force microscopy (PFM). PFM is a powerful tool for probing local piezoelectric and

ferroelectric properties of materials at the nanoscale. In 1991, the Dransfeld group used a scanning tunneling microscope (STM) to measure the bias-induced deformation due to piezoelectricity in a vinylidene fluoridetrifluoroethilene (VDF-TrFE) sample provided with a top gold electrode[26]. Following this, a series of pioneering results have been obtained by Takata et al. using strain imaging via tunneling acoustic microscopy[27]. In 1992, the use of AFM to investigate piezoelectric properties was also attempted by Güthner and Dransfeld. Franke et al. were the first to observe a poled region in PZT[28]. Gruverman *et al*. were the first to observe the grown domain structure within the PZT grains and also presented the first results on the poling of BTO and PZT in 1996[29]. Gruverman *et al*. were also the first researchers to report on the nanoscale properties of fatigue in PZT thin films[29]. In 1996, the formation and nanoscale domains of PZT thin films were performed by Hidaka *et al*[30]. The work by Gruverman *et al*. is particularly important because it demonstrates imaging and switching in common ferroelectrics, and it creates the terms 'Piezoresponse' and 'PFM', which are now standard. In 1999, Eng *et al*. reported the use of PFM to measure the 3D polarization distribution in $BaTiO_3$ ceramics[31]. In 2000, Christman *et al*. reported the spatial variation of ferroelectric properties in PZT capacitors using SPM-based techniques[32]. More review and further development of PFM techniques were presented by Kalinin et al[33]. Today, PFM is the premier tool for probing static and dynamic properties of ferroelectric materials at the

nanoscale, as evidenced by a number of recent papers and books. Some novel techniques of PFM have also been developed, including: Dual Frequency PFM[34], Switching Spectroscopy PFM[35], and Band-Excitation PFM[36]. The principles and various applications of PFM will be detailed in Chapter 2.

1.4 Electromechanical Coupling in Biological Systems

Coupling between electrical and mechanical phenomena in living tissue was first discovered by Galvani in 1771. He recorded the phenomenon while dissecting a frog at a table where he had been conducting experiments with static electricity. One of the important phenomena of electromechanical behavior is piezoelectricity. Since the 1950s, piezoelectricity in biological tissue has attracted significant scientific interest. Piezoelectricity was first discovered in bones in 1957[37] and was subsequently reported in a variety of biological systems, including teeth[38], wood[39], and seashells[40]. A subset of piezoelectrics is known as pyroelectric with spontaneous polarization, and such pyroelectricity was observed in bones and tendons in 1966[41]. Experimentally, it was observed that the piezoelectric constant of biopolymers is on the order of 1–5 pm/V, which is comparable to inorganic piezoelectrics, such as quartz[42]. Piezoelectricity in biological systems is believed to play a significant role in controlling the mechanisms of local tissue development. For example, sustained applications of an electrical potential

could stimulate both resorption and growth of bone[43]. Recently, piezoelectricity has also been suggested to be one of the toughening mechanisms in seashells[40]. However, due to the complex hierarchical structure of biological systems, the effect and implications of piezoelectricity in biological systems remain largely unresolved, and it is important to understand the relationship between physiologically generated electric fields and mechanical properties on the molecular, cellular, and tissue levels.

On the other hand, so far there is very limited evidence for ferroelectricity in biological systems, especially in soft tissue, even though it has long been speculated in biology[44]. Given the seemingly ubiquitous piezoelectricity in biological tissue, it is quite surprising that ferroelectricity has not yet been observed in biopolymers.

As discussed above, many biological materials are piezoelectric. To understand the electromechanical coupling in biological materials on the nanoscale and to relate it to biological functionality and other properties, a nanoscale probe of local piezoelectricity is needed. Piezoresponse force microscopy (PFM) is a powerful tool to probe electromechanical coupling in piezoelectric and ferroelectric systems at the nanoscale. In recent years, it has been applied to study a variety of biological tissue and materials. These include: human bones[45] and teeth[38], tooth dentin and enamel[46], collagen fibrils[47], insulin and lysozyme amyloid fibrils, deer antlers, breast adenocarcinoma cells[48],

butterfly wings, and bacteriorhodopsin[49]. PFM can detect the differences between organic and mineral components of biological systems and provides information on the material's microstructure and piezoelectric properties. The use of vector PFM may also enable protein orientation to be determined in real space. While these studies established piezoelectricity in biological tissue at the nanoscale, biological ferroelectricity remains elusive.

1.5 Objective and Scopes of the Studies

This work seeks to achieve a fundamental understanding of ferroelectric nanostructures and enable their engineering applications by developing systematic methodologies to fabricate, manipulate, and probe ferroelectrics at the nanoscale. The characterization of ferroelectricity of various inorganic materials, using the PFM system, is discussed in Chapter 3 and Chapter 4. Nanostructures of organic P(VDF-TrFE 65:35) copolymers are developed using the nanoimprinting process outlined in Chapter 5, and their ferroelectric properties are confirmed by PFM in this chapter, as well. Then, the biological ferroelectricity in the aortic walls and the elastin network is studied in Chapter 6. The dissertation concludes with a summary and an outlook for future work.

Reference

[1] J. Valasek, Physical Review (1920).

[2] Q. M. Zhang, V. Bharti, and X. Zhao, Science **280,** 2101 (1998).

[3] J. F. Scott, Science **315,** 954 (2007).

[4] S. Clemens, S. Rohrig, A. Rudiger, T. Schneller, and R. Waser, Nanotechnology **20** (2009).

[5] Z. J. Hu, M. W. Tian, B. Nysten, and A. M. Jonas, Nature Materials **8,** 62 (2009).

[6] L. Liao, H. J. Fan, B. Yan, Z. Zhang, L. L. Chen, B. S. Li, G. Z. Xing, Z. X. Shen, T. Wu, X. W. Sun, J. Wang, and T. Yu, Acs Nano **3,** 700 (2009).

[7] J. F. Scott, M. Dawber, A. Q. Jiang, and F. D. Morrison, Ferroelectrics **286,** 945 (2003).

[8] Y. H. Chu, L. W. Martin, M. B. Holcomb, M. Gajek, S. J. Han, Q. He, N. Balke, C. H. Yang, D. Lee, W. Hu, Q. Zhan, P. L. Yang, A. Fraile-Rodriguez, A. Scholl, S. X. Wang, and R. Ramesh, Nature Materials **7,** 478 (2008).

[9] B. J. Chu, X. Zhou, K. L. Ren, B. Neese, M. R. Lin, Q. Wang, F. Bauer, and Q. M. Zhang, Science **313,** 334 (2006).

[10] F. Jona and G. Shirane, (1962).

[11] G. Shirane, K. Suzuki, and A. Takeda, Journal of the Physical Society of Japan **7,** 12 (1952).

[12] B. Jaffe, R. S. Roth, and S. Marzullo, Journal of Applied Physics **25,** 809 (1954).

[13] B. Jaffe, W. R. C. Jr., and H. Jaffe, Academic Press, New York Chapter 1 (1971).

[14] H. Kawai, Japanese Journal of Applied Physics **8,** 975 (1969).

[15] K. Koga and H. Ohigashi, Journal of Applied Physics **59,** 2142 (1986).

[16] M. D. K. Tashiro, Ferroelectric polymers (chemistry, physics, and applications) New York 63 (1995).

[17] J. F. Scott, Ferroelectrics **236,** 247 (2000).

[18] D. W. Chapman, Journal of Applied Physics **40,** 2381 (1969).

[19] Francomb.Mh, Thin Solid Films **13,** 413 (1972).

[20] B. S. Sharma, S. F. Vogel, and P. I. Prentky, Ferroelectrics **5,** 69 (1973).

[21] S. Y. Chou, P. R. Krauss, and P. J. Renstrom, Science **272,** 85 (1996).

[22] International Technology Roadmap for Semiconductors, http://public.itrs.net/.

[23] L. J. Guo, Journal of Physics D-Applied Physics **37,** R123 (2004).

[24] Q. F. Xia, K. J. Morton, R. H. Austin, and S. Y. Chou, Nano Letters **8,** 3830 (2008).

[25] M. Colburn, A. Grot, B. J. Choi, M. Amistoso, T. Bailey, S. V. Sreenivasan, J. G. Ekerdt, and C. G. Willson, Journal of Vacuum Science & Technology B **19,** 2162 (2001).

[26] P. GUTHNER, J. GLATZREICHENBACH, and K. DRANSFELD, JOURNAL OF APPLIED PHYSICS **69,** 7895 (1991).

[27] K. TAKATA, T. HASEGAWA, and S. HOSAKA, APPLIED PHYSICS LETTERS **55,** 1718 (1989).

[28] K. Franke, J. Besold, W. Haessler, and C. Seegebarth, Surface Science **302,** L283 (1994).

[29] A. Gruverman, O. Auciello, and H. Tokumoto, Applied Physics Letters **69,** 3191 (1996).

[30] T. Hidaka, T. Maruyama, M. Saitoh, N. Mikoshiba, M. Shimizu, T. Shiosaki, L. A. Wills, R. Hiskes, S. A. Dicarolis, and J. Amano, Applied Physics Letters **68,** 2358 (1996).

[31] L. M. Eng, Nanotechnology **10,** 405 (1999).

[32] J. A. Christman, S. H. Kim, H. Maiwa, J. P. Maria, B. J. Rodriguez, A. I. Kingon, and R. J. Nemanich, Journal of Applied Physics **87,** 8031 (2000).

[33] S. V. Kalinin, B. J. Rodriguez, S. Jesse, E. Karapetian, B. Mirman, E. A. Eliseev, and A. N. Morozovska, in *Annual Review of Materials Research*; *Vol. 37* (Annual Reviews, Palo Alto, 2007), p. 189.

[34] B. J. Rodriguez, C. Callahan, S. V. Kalinin, and R. Proksch, Nanotechnology **18,** 475504 (2007).

[35] S. Jesse, A. P. Baddorf, and S. V. Kalinin, Applied Physics Letters **88** (2006).

[36] S. Jesse, S. V. Kalinin, R. Proksch, A. P. Baddorf, and B. J. Rodriguez, Nanotechnology **18** (2007).

[37] E. Fukada and I. Yasuda, Journal of the Physical Society of Japan **12,** 1158 (1957).

[38] A. Gruverman, D. Wu, B. J. Rodriguez, S. V. Kalinin, and S. Habelitz, Biochemical and Biophysical Research Communications **352,** 142 (2007).

[39] V. A. Bazhenov, Piezoelectric Properties of Wood**,** Pp. xii+180. New York: Consultants Bureau (1961).

[40] T. Li and K. Zeng, Acta Materialia **59,** 3667 (2011).

[41] S. B. Lang, Nature **212,** 704 (1966).

[42] V. E. Bottom, Journal of Applied Physics **41,** 3941 (1970).

[43] S. R. Pollack, E. Korostoff, W. Starkebaum, and W. Lannicone, edited by C. T. Brighton, J. Black, and S. R. Pollack (Grune & Stratton, New York) (1979).

[44] S. B. Lang, Ieee Transactions on Dielectrics and Electrical Insulation **7,** 466 (2000).

[45] C. Halperin, S. Mutchnik, A. Agronin, M. Molotskii, P. Urenski, M. Salai, and G. Rosenman, Nano Letters **4,** 1253 (2004).

[46] S. V. Kalinin, B. J. Rodriguez, S. Jesse, T. Thundat, and A. Gruverman, Applied Physics Letters **87** (2005).

[47] M. Minary-Jolandan and M.-F. Yu, ACS Nano **3,** 1859 (2009).

[48] A. Gruverman, B. J. Rodriguez, and S. Kalinin, Scanning Probe Microscopy: New York: Springer Science+Business Media (2007).

[49] S. V. Kalinin, B. J. Rodriguez, S. Jesse, K. Seal, R. Proksch, S. Hohlbauch, I. Revenko, G. L. Thompson, and A. A. Vertegel, Nanotechnology **18** (2007).

Chapter 2 Piezoresponse Force Microscopy

Piezoresponse force microscopy (PFM) is a mode of Atomic Force Microscopy (AFM) that allows for the imaging and manipulation of ferroelectric domains, and it is a powerful tool for probing local piezoelectric and ferroelectric properties of materials at the nanoscale. In this chapter, we will illustrate the general operating principle of scanning probe microscopy (SPM), followed by a more detailed description of various SPM modes. The PFM operating principle and setup will then be explained in detail, as well as the description of several specific applications, such as lateral PFM, switching spectroscope PFM and PFM lithography.

2.1 Scanning Probe Microscopy

2.1.1 Introduction

The class of SPM instruments has grown steadily since the invention of the Scanning Tunneling Microscope (STM), by Binning and Rohrer, for which they were awarded the Nobel Prize in Physics, in 1986[1]. STM is based on quantum tunneling to generate real-space images of surfaces with an atomic resolution by applying a bias between an ultra-sharp metallic tip and a conductive sample surface[1]. SPM, on the other hand, includes a wider range of technologies having a sharp tip carrying out near field probe imaging on sample surfaces through lateral scanning. This is achieved by moving the tip line by line

and recording the spatial variation between interactions. Various interactions between the sample surface and the probe can be measured, including electrical, magnetic, and mechanical. For example, SPM-based measurements of piezoelectric thin films have been used by a number of investigators to probe their local properties at the nanoscale[2-5].

2.1.2 The Atomic Force Microscope

Binning *et al.* invented the first atomic force microscope (AFM), which was based on the mechanical detection of the Van der Waals forces between the tip and the surface, using a soft cantilever in 1986[6]. AFM is currently the most broadly employed tool in the SPM family, since it can measure a wide range of surface properties on any kind of material. Moreover, the measurements are performed at normal temperatures and pressures, without special requirements on environmental conditions.

2.1.2.1 AFM Operating Principle

The AFM consists of a cantilever with a sharp tip (probe), which is typically silicon or silicon nitride, with a height on the order of micrometers and a radius of curvature of generally 10-20 nm. As the tip approaches a surface, the cantilever reacts to the forces between the tip and the investigated sample surface according to Hooke's law. Various kinds of atomic forces are involved in such an interaction. Forces that are measured in AFM include: mechanical contact force, van der Waals forces, capillary forces, chemical

bonding, electrostatic forces, and magnetic forces. A feedback loop correcting the cantilever's deflection keeps the tip either at a constant distance to the surface or at a constant force with the surface, depending on the scanning modes employed. A piezoelectric element is used to drive the probe downwards or upwards, and the cantilever can react to the topography of the sample. Since the piezoelectric elements can precisely generate very sensitive and tiny movement, AFM can perform very precise scanning.

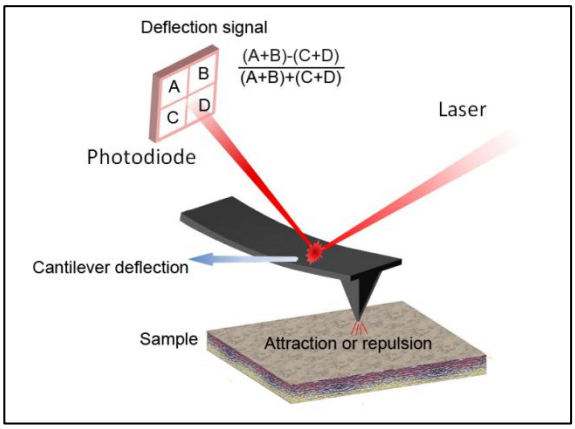

Figure 2.1 Representation of AFM in contact mode.

As shown in Figure 2.1, AFM systems usually include a thin cantilever with an ultra-sharp probing tip, a 3D piezoelectric scanner, and an optical system to measure the deflection of the cantilever. When the tip is driven by piezoelectric elements to the sample surface, it will be affected by a combination of the surface forces (repulsive and attractive). Those forces cause cantilever bends or twists, and these deformations of the cantilever are detected by measuring the displacement of the laser spot. The deflection of

the cantilever is typically detected by measuring the reflected laser beam on a four sector photodetector (Figure 2.1). Angular displacement of the cantilever results in one photodiode collecting more light than the other photodiode. The output signal is proportional to the deflection of the cantilever with a sensitivity of less than 1Å. The photodetector converts the separate vertical and lateral change into an electrical signal:

$$Deflection = V_{top} - V_{bottom} = (V_A + V_B) - (V_C + V_D)$$
$$Lateral = V_{left} - V_{right} = (V_A + V_C) - (V_B + V_D)$$

The deflection signal is the difference between the voltages generated in the top and bottom halves of the detector. Similarly, the differential signal between the sum of the two left elements and the sum of the two right elements provides a measure of the lateral signal (torsion) in the cantilever. The variation deflection signal is recorded, sent to the computer, and processed to show a real topography image, meanwhile the deflection signals showing error information are also used as feedback signals to the piezoelectric element to control the cantilever's Z position to track the topographic change of the sample surface.

2.1.2.2 Tapping Mode

Tapping Mode (or AC Mode) is the most widely used AFM mode for topography imaging. The cantilever is driven to oscillate up and down near its resonance frequency

by a small piezoelectric element in the AFM tip holder. Meanwhile, the amplitude is used as feedback for the vertical adjustment of the piezoscanner to record the height image. A tapping AFM image is, therefore, produced by imaging the force of the intermittent contacts of the tip with the sample surface.[7] When the cantilever approaches the sample surface from free air, the repulsive or attractive forces from the surface will act on the cantilever and change its amplitude and phase. The cantilever is driven down until the amplitude signal reaches the setpoint, upon which it will hold a constant distance from the sample. While scanning, the phase changes are also captured in the phase image acquired by the photodetector, and the amplitude value is kept at a constant at the setpoint value by the vertical movements of the scanner.[8] The tapping mode has a few advantages, including: higher resolution on most samples (near 1 nm), lower forces, and less damage to soft samples imaged in the air.

2.1.2.3 Contact Mode

Contact mode is the basic option for a variety of measurements of surface properties. The probe is driven toward the surface by extending the Z scanner. In this mode, the tip is in contact with the sample and keeps a constant height with the surface. When the tip is engaged and makes contact with the surface, the cantilever starts bending and the extension of the Z scanner starts to decrease after the cantilever deflection reaches the

setpoint.The feedback is turned on by keeping the cantilever and sample with a correlative contact force. The surface features change the deflection of the cantilever while the tip scans, and the feedback loop adjusts the scanner's vertical Z position up and down to maintain the deflection constant to the setpoint. Finally, the Z scanner movement information is captured and it gives the topography image. The piezoresponse force microscopy (PFM) is built based on the contact mode.

2.1.2.4 Force Curve

The contact force can be determined by performing the force plot procedure. The Z scanner and probe have a two-step movement: 1) approaching the surface, and then 2) retracting from it. The deflection of the cantilever is plotted versus this movement as a force plot. The schematic is shown in Figure 2.2 (a). Starting from a non-contact position (a), the probe approaches the surface freely (red line, A-B), and then the tip is attracted by the van der Waals forces, which makes the cantilever bend toward the opposite direction (red line, B-C). Lowering the probe further will increase the repulsive force (red line, C-D). At the release procedure (blue line), the deflection decreases until the spring force of the cantilever overcomes the attractive forces at the pull-off point, E, in Figure 2.2 (a), and the cantilever finally gets back to the free position. The deflection of the cantilever Δx can be used to calculate the force acting on the tip via Hook's law, $F = k \cdot \Delta x$, where k is the spring constant of the cantilever. The actual force-curve from an AFM on

PVDF copolymer is shown in Figure 2.2 (b), which indicates that the force between the tip and the surface changes with their separation distance. The two curves trace the force and distance as the tip approaches the surface and is retracted from the surface. The dip on the retracting curve is due to adhesion to the surface.

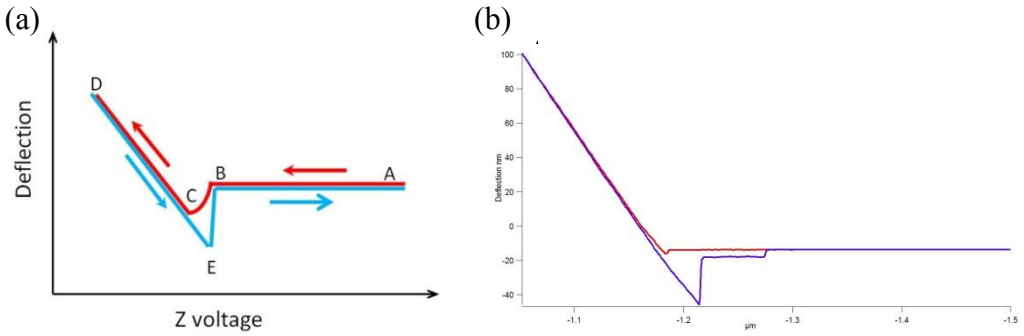

Figure 2.2 (a) A schematic of the force curve, and (b) an actual force-curve for the PVDF copolymer. In the schematic force curve, the red and blue lines represent the response of the tip approaching to and retracting from the surface.

2.1.3 SPM Techniques for Ferroelectrics

In recent years, with the ever-increasing interests in oxide electric devices, such as microelectro-mechanical systems (MEMS), non-volatile ferroelectric memories (FeRAMs), and multiferroics, study of the local ferroelectric properties at the nanometer level is highly desired. This has motivated the development of various scanning probe microscopy techniques used for the characterization of ferroelectric materials, as summarized below.

Electrostatic Force Microscopy (EFM): EFM is a type of dynamic non-contact AFM where the electrostatic force is probed[9]. This force arises due to the attraction or repulsion of separated charges, which is used to characterize the electrostatic fields above the ferroelectric surface induced by surface polarization charge. A bias voltage is applied to a conductive cantilever tip and sample, and the force between bias and sample surface potential can be detected as far as 100 nm. The obtained signal contains information regarding both the surface topography and surface electrical property. In the Nap mode, the even scan is performed to obtain the topography by scanning the tip near the surface as it is done in general AFM, in the region where the van der Waals forces are dominant. In the odd scan, the system uses parameters, which can have a delta height applied, in order to place the tip in the region where the electrostatic forces are dominant. The tip is then biased and scanned without feedback, parallel to the topography line obtained from the first scan and, therefore, maintain constant tip-sample distance. So, from the odd scan, the EFM signal can be obtained.

Kelvin Probe Force Microscopy (KPFM): KPFM is also based on an AFM set-up, and the work principle is based on the measurement of the electrostatic forces between the small AFM tip and the sample[10]. Unlike EFM, KPFM can measure the potential offset between a probe tip and a surface using the same principles as a macroscopic Kelvin probe. When there is a direct-current (DC) potential difference between the tip and the

surface, the AC and DC voltage offset will cause the cantilever to vibrate. The vibration of the cantilever will be detected by the usual SPM method. Then, a null circuit is used to drive the DC potential of the tip to a value which minimizes the vibration of the cantilever. The surface potential can be understood by mapping this nulling DC potential. Both EFM and KPFM require the use of conductive cantilevers and are sensitive mostly to out-of-plane polarization components. EFM is much more sensitive to topographic artifacts than KPFM, while KPFM gives information about the composition and electronic state of the sample surface.

As an example, we have used KPFM to simultaneously study structural and electronic properties of the porcine aortic wall. As shown in Figure 2.3, the topography of the 10×10 μm^2 aortic wall, as well as its surface potential, are acquired using the KPFM mode. The surface potential mapping overlaid on the 3D topography image is shown in Figure 2.3 (c).

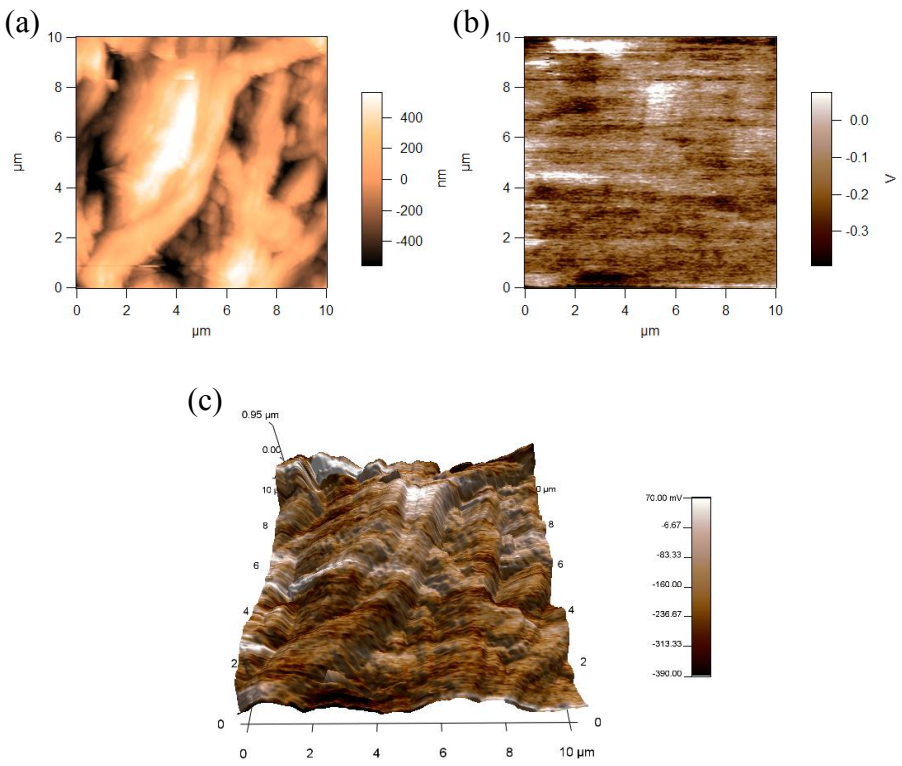

Figure 2.3 KPFM mapping of the 10×10 µm^2 porcine aortic wall: (a) topography, (b) surface potential, and (c) surface potential mapping overlaid on the 3D topography image.

2.2 Piezoresponse Force Microscopy

Piezoresponse Force Microscopy (PFM), a derivative of the contact mode of the AFM, is a powerful tool for probing local piezoelectric and ferroelectric properties of materials at the nanoscale[11,12]. Some novel techniques of the PFM have also been developed, including Dual Frequency PFM[13], Switching Spectroscopy PFM[14], and Band-Excitation PFM[15]. In this section, various PFM methods will be introduced.

2.2.1 Vertical PFM

PFM techniques are based on the piezoelectric effect, where a piezoelectric material expands or contracts in accordance to the external electric field applied. The representation in Figure 2.4 (a) shows the PFM setup, including all of the components of the measurement equipment. The AFM probes a sample's mechanical response to an applied electric field. The AFM tip used is usually made of, or is coated with, a conductive material. An AC bias to the probe tip is applied, in order to excite deformation of the sample through the piezoelectric effect. The resulting deflection of the probe cantilever is detected through a standard photodiode detector method, and then demodulated using a lock-in amplifier. In this way, topography and ferroelectric domains can be imaged simultaneously with high resolution.

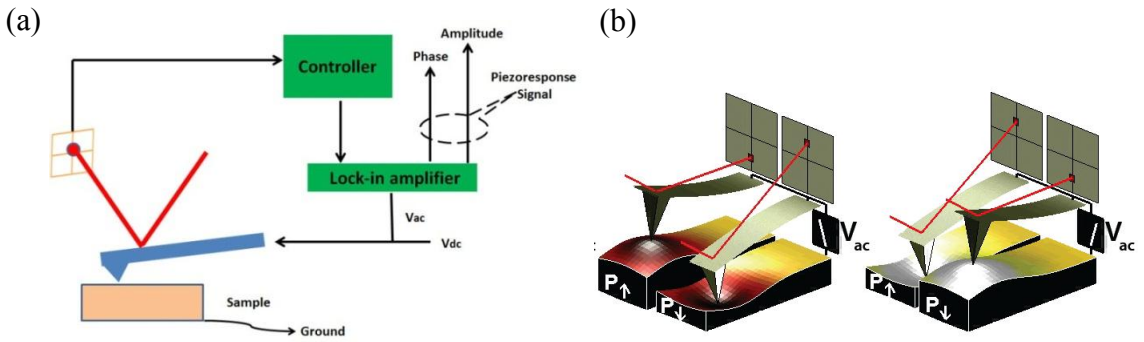

Figure 2.4 Schematic of the Piezoresponse Force Microscopy principle (a) and polarization direction dependence of the sample strain (b) (figure (b) courtesy of S. Jesse, ORNL.).

In vertical PFM measurements, an AC driving voltage, $V_{ac} = V_0 e^{i\omega t}$, is applied to the

specimen, which induces a surface vibration, $u_{ac} = d_{33}V_0 e^{i(\omega t+\varphi)}$, of the specimen due to its piezoelectricity, where d_{33} is the out-of-plane piezoelectric coefficient of the material[16]. As shown in Figure 2.4 (b), if the polarization and the applied electric field are parallel, the deformation is positive (expansion) and the piezoresponse signal is in phase with V_{ac}. On the contrary, if the applied electric field is antiparallel to the spontaneous polarization, this will cause the piezoelectric to contract with the consequent lowering of the cantilever, and thus, the electric field and the piezoresponse signal are shifted in phase by 180°.

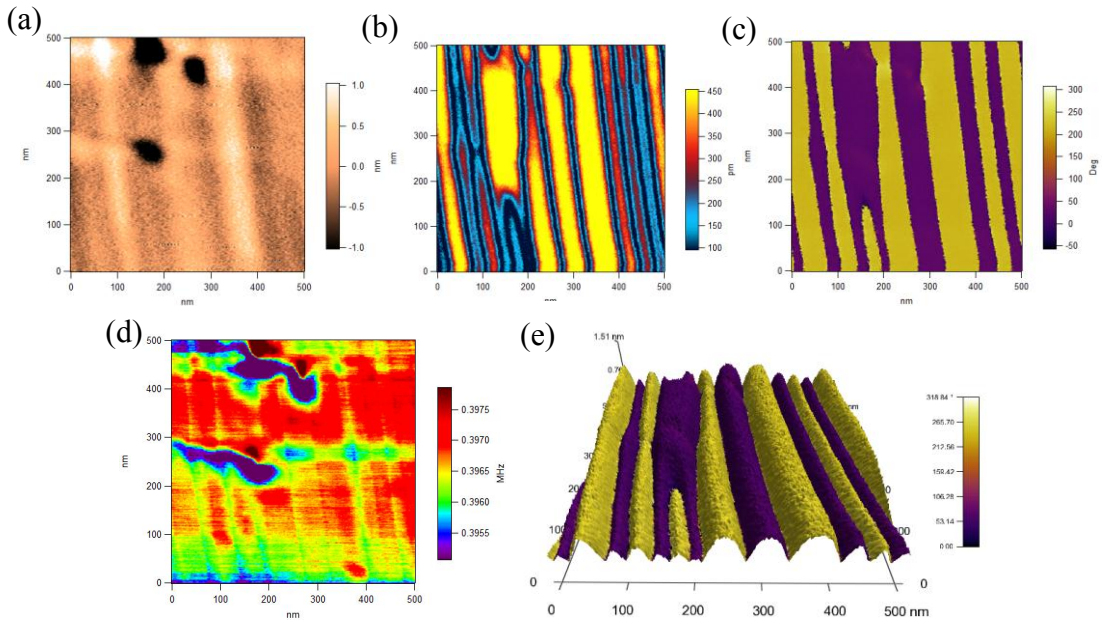

Figure 2.5 PFM images of the 500×500 nm^2 epitaxial $BiFeO_3$ thin film: (a) topography, (b) amplitude, (c) phase, (d) frequency, and (e) phase mapping overlaid on the 3D amplitude image.

For example, PFM images for a 100-nm (001) oriented $BiFeO_3$ ferroelectric thin film provided by Prof. Xiaoqing Pan at the University of Michigan are shown in Figure 2.5.

The amplitude, phase, as well as resonant frequency, of the out-of-plane polarization domains are imaged, simultaneously. Generally, the amplitude image represents the strength of the spontaneous polarization at various locations, and the phase signal reflects the direction of the spontaneous polarization; for a pair of anti-parallel polarizations, the difference of the phase signal is 180^{o}. At the boundary of two different polarization domains (i.e., domain walls), the amplitude signal drops significantly. In the phase image, the different color contrast corresponds to different polarization domains. In order to determine the polarization direction of different domains, an external DC source should be used to switch a local area, and the polarization direction can then be determined by analyzing the change in contrast to the PFM phase image. From the image of phase mapping overlaid on the 3D amplitude (Figure 2.5 (e)), it is clearly shown that, when crossing the oppositely polarized domains, the amplitude values are similar to each other.

2.2.2 Lateral PFM

Lateral PFM based on the piezoelectric coefficient, d_{15}, has also been developed to map the in-plane polarization distribution[17]. Detection of the lateral components of the tip vibrations provides information on the in-plane surface displacement, known as the lateral PFM. Similar to the vertical PFM, the direction of the polarization for the in-plane polarized ferroelectric domain can be deduced via a shear piezoelectric coefficient, d_{15}

(Figure 2.6). In this case, the applied electric field causes a shear deformation of the domain, which is transferred to the torsional movement of the cantilever. Similar to the vertical PFM, the amplitude of the in-plane polarization response is given by $A_L=d_{15}V_{ac}$, and the polarization direction can be determined by lateral phase image. It should be noticed that this lateral oscillation can only be generated by an AC drive voltage when the in-plane polarization vector is perpendicular to physical axis of cantilever. Then, in order to obtain complete mappings of the in-plane polarization distribution, physical rotation of the sample by 90^o will be necessary, and two components of the displacement vector can be determined by the imaging of the same region of the sample before and after the rotating sample. Provided that the vertical and lateral PFM signals are properly calibrated, the complete electromechanical response vector can be determined, and the three-dimensional PFM can be obtained by combining vertical and lateral PFM together[18].

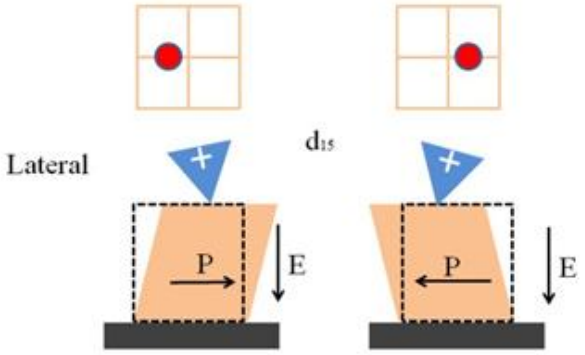

Figure 2.6 Schematic of the lateral polarization in the ferroelectric sample investigated by the PFM.

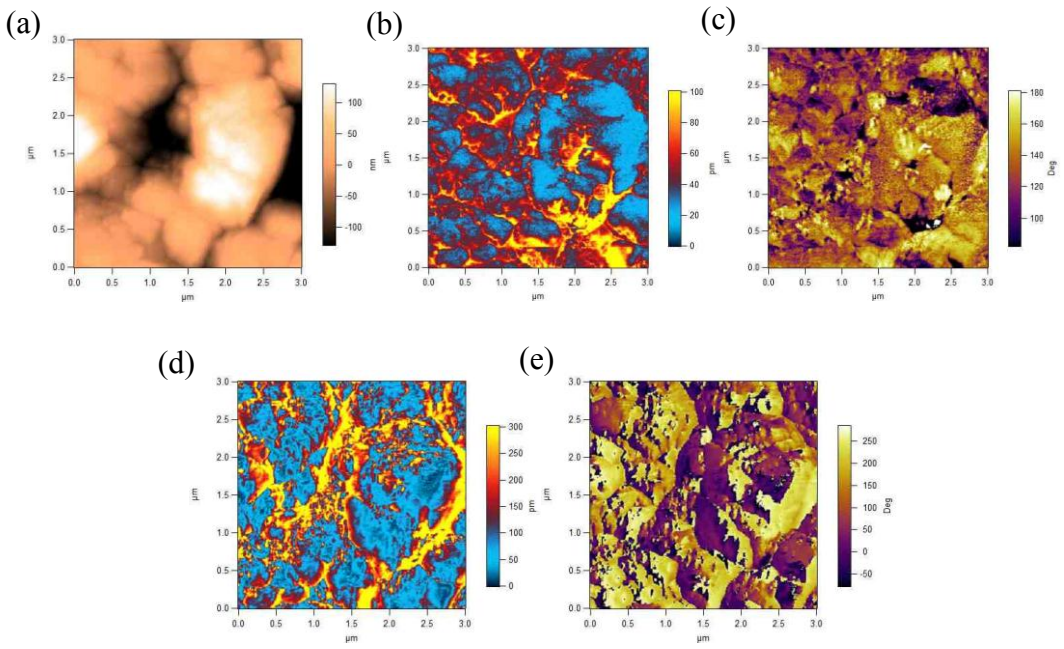

Figure 2.7 Topography (a), vertical amplitude (b), vertical phase (c), lateral amplitude (d), and lateral phase (e) of the PZT film with a 3×3 μm^2 scan area.

For example, Figure 2.7 presents the experimental results on the simultaneous acquisition of vertical and lateral piezoresponse images, as well as topography of the PZT thin film, with a sample provided by Prof. Qifa Zhou of USC. The stronger lateral amplitude image, as shown in Figure 2.7 (c), suggests predominantly in-plane orientation of the polarization vector. It should also be noted that the amplitude and phase images correspond to each other very well for both the vertical and lateral PFMs, and those images present the domain structure along two directions of the PZT thin film.

2.2.3 Single Frequency Resonance and Dual Frequency Resonance Tracking Technique (DFRT)

As illustrated schematically in Figure 2.8 (a), the cantilever–sample system can be viewed as a damped harmonic oscillator in a typical PFM measurement. In order to enhance the piezoresponse sensitivity, the AC voltage is often driven near the resonance of the cantilever-specimen system, magnifying the piezoresponse amplitude, $A = d_{33}V_0Q$, by orders of magnitude. Under the damped harmonic oscillator model, the PFM amplitude A, the phase ϕ, the quality factor Q, and the resonant and applied frequencies, ω_0 and ω, are related by the following equations[19]:

$$A = \frac{d_{33}V_0}{\sqrt{(1-\omega^2/\omega_0^2)^2 + (\omega/\omega_0 Q)^2}}, \quad \phi = \tan^{-1}\frac{\omega\omega_0}{Q(\omega_0^2 - \omega^2)},$$

which can be used for quantitative analysis, as is discussed later.

The traditional single frequency technique used by the PFM, as is discussed earlier, suffers a number of drawbacks. If the AC modulation voltage is driven at the resonance frequency, the tip deflection is magnified by an unknown factor of Q, compared to the quasi-static response, according to the equation above, as is schematically shown in Figure 2.8 (b) and is confirmed by our fitting of the experimental data. Since Q is generally unknown and usually varies from sample to sample, this makes quantitative

analysis difficult.

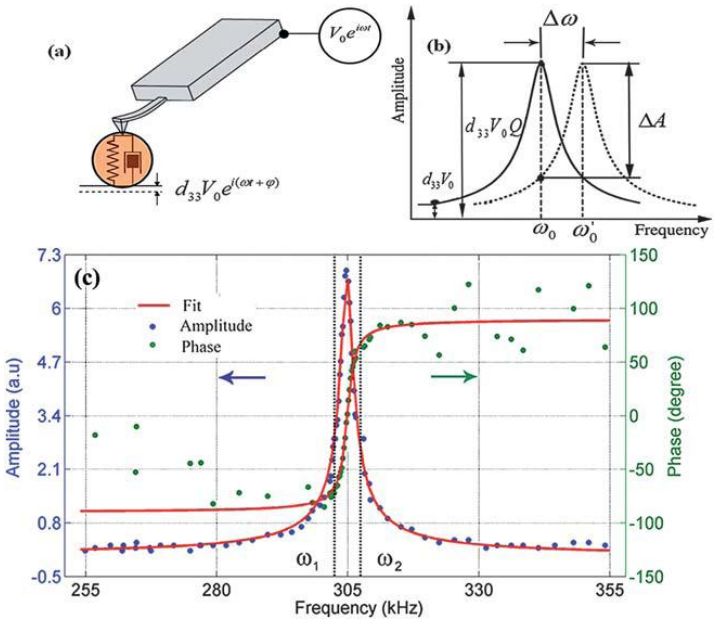

Figure 2.8 Schematics of the dual frequency resonance tracking (DFRT) technique: (a) tip-sample harmonic oscillation system, (b) resonance enhancement using a single frequency, and (c) schematics of the dual frequency resonance tracking using actual experimental data of piezoresponses versus AC driving frequency.

A dual-excitation method for resonant-frequency tracking in the scanning probe microscopy, based on amplitude detection, was developed by Oak Ridge National Laboratory and the Asylum Research Company[13]. The principle of the dual-frequency resonance-tracking (DFRT) method is that a potential of the conductive cantilever is separated into two oscillating drive voltages and frequencies at or near the resonance. In the DFRT mold, the response is measured at two drive frequencies, ω_1 and ω_2, yielding amplitudes A_1 and A_2. The difference between these two frequencies, $\Delta\omega = \omega_2 - \omega_1$, is typically chosen, such that the amplitudes A_1, $A_2 \sim A_r/2$, where A_r is the amplitude at

resonance and $A_2 - A_1 \approx 0$. Then, the measured amplitude $A_{1,2}$ and phase shift $\varphi_{1,2}$ at two distinct frequencies $\omega_{1,2}$ across the resonance, as schematically shown in Figure 2.8 (c) using actual experimental data, gives us four measurements, making it possible to solve for ω_0, Q, A_n, and φ_n simultaneously from the measured $A_{1,2}$ and $\varphi_{1,2}$ using the equation above. The DFRT technique has several unique advantages. The PFM scan is operated at a near contact resonance that increases the electromechanical response 10-100 times compared to the one farther away from the resonance, while at the same time, it avoids crosstalk with topography and structure heterogeneity by tracking the resonance frequency. Even more significantly, it can help us to determine the quality factor Q quantitatively.

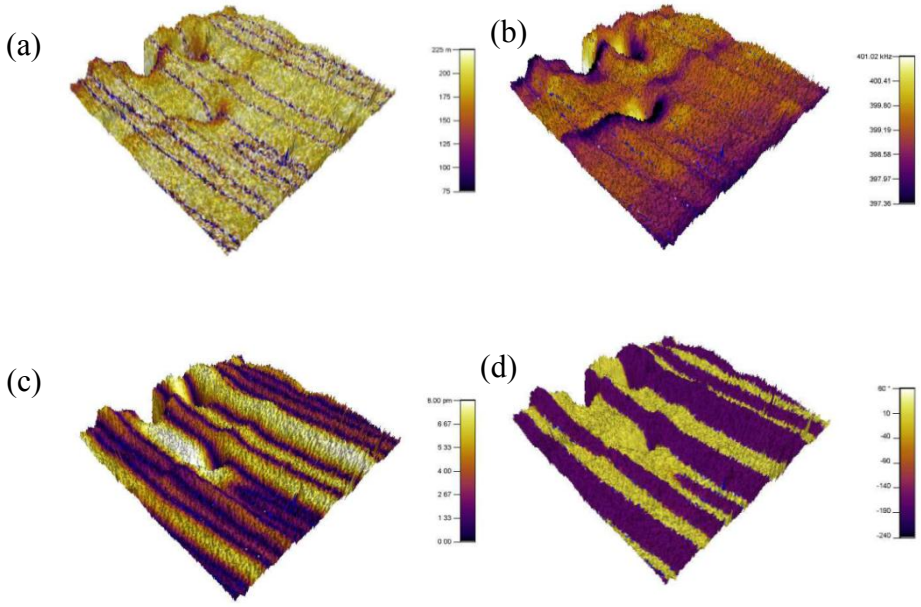

Figure 2.9 Mapping of the: (a) quality factor, (b) resonant frequency, (c) amplitude, and (d) phase of the epitaxial $BiFeO_3$ superimposed on its three-dimensional topography.

To demonstrate this technique, we applied the proposed quantitative DFRT PFM to probe an epitaxial $BiFeO_3$ thin film provided by Prof. Xiaoqing Pan of the University of Michigan. A 500 nm by 500 nm PFM scan was carried out using DFRT under the AC modulation voltage of 4.4 V, from which mappings of amplitude $A_{1,2}$ and phase shift $\varphi_{1,2}$ are obtained under $\omega_{1,2}$. These two frequencies vary spatially due to the variation of the contact stiffness of the sample and are adjusted to track the resonance via feedback control. This allows us to solve for ω_0, Q, φ_n, and A_n at each point and map their spatial distributions, as shown in Figure 2.10, where the mappings of quality factor Q (a), resonance frequency ω_0 (b), amplitude A_n/Q (c) and phase shift φ_n (d) are imposed on top of the three dimensional thin film topographies.

From the calculated PFM mapping, we observed a large variation in the quality factor, Q, which ranged from 90 to 180, as shown in Figure 2.9 (a). This underscores the importance of accurate determination of the quality factor for the quantitative PFM characterization. In addition, it can also be observed from Figure 2.5 (b) that the resonance frequencies vary over the surface of the sample, ranging from 397 kHz to 401 kHz. While this seems to be a rather small variation, it can result in a large reduction of the sensitivity if a conventional single frequency resonance enhancement technique is used during scanning. For example, if we lock in at 401 kHz, while the actual resonance at a particular point is 397 kHz, then the piezoresponse is approximately $43d_{33}V$

according to the equation above for a typical quality factor of 100, instead of $100d_{33}V$ as is expected at this resonance. This would not only result in the loss of sensitivity, but also lead to a false contrast in the piezoresponse mapping. The PFM phase contrast is clearly observed in Figure 2.9 (c) and corresponds to the amplitude mapping in Figure 2.9 (d) as well, indicating different polarity in different domains. The cross-talk due to the shift in the resonance frequency has been minimized. Furthermore, the intrinsic piezoresponse of the sample can now be determined by correcting the quality factor, making it possible to map the spatial distribution of the piezoelectric coefficient, d_{33}, quantitatively, as shown in Figure 2.9 (d). It is observed that the maximum piezoresponse amplitude, after the correction, is only 8.0 pm.

2.2.4 Local Domain Switching and SSPFM

Domain switching PFM is a technique to quantitatively investigate the local switching characteristics of ferroelectric materials. The tip approaches the surface vertically in the contact mode until the deflection set point is achieved. Local hysteresis loop is collected at a fixed location using the wave function, as shown in Figure 2.10. They are obtained by sweeping the DC voltage from zero to the positive and then the negative coercive voltage. A sine wave is carried by a square wave that steps in magnitude with time. Between each ever-increasing voltage step (state "On"), the offset

is stepped back to zero (state "Off") with the AC bias still applied to determine the resulting deflection. Both "On" and "Off" states reveal the electric interactions between the AFM tip and sample surfaces, while the "Off" state is usually more preferred because it significantly minimizes the electrostatic effect. From the hysteresis loops, the ferroelectric parameters, such as the positive and negative coercive biases, saturation response, and work of switching can be obtained.

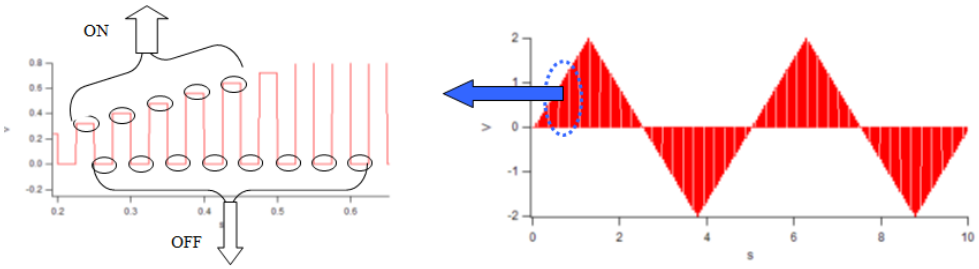

Figure 2.10 DC voltage waveforms for the domain switching PFM.

As a typical example of the local domain switching PFM, we apply a sequence of DC bias imposed by a 2.2 V AC driving voltage to an annealed P(VDF-TrFE) film, with the AC driving voltage set to be much smaller than the coercive voltage of the film to avoid interference with switching instability. The hysteresis and butterfly loops are shown in Figure 2.11, which are measured during the "ON" and "OFF" states under DC bias. In the "OFF" state, the tip-surface electrostatic interaction is reduced, and the ferroelectricity and piezoelectricity are investigated without the influence of the DC voltage previously applied. The actual remnant piezoresponse is detected, so the retention

characteristics of the ferroelectric are revealed. Note that the measured piezoresponse phase versus the DC voltage does not give conventional hysteresis of polarization versus the electric field, but phase changing along with DC bias.

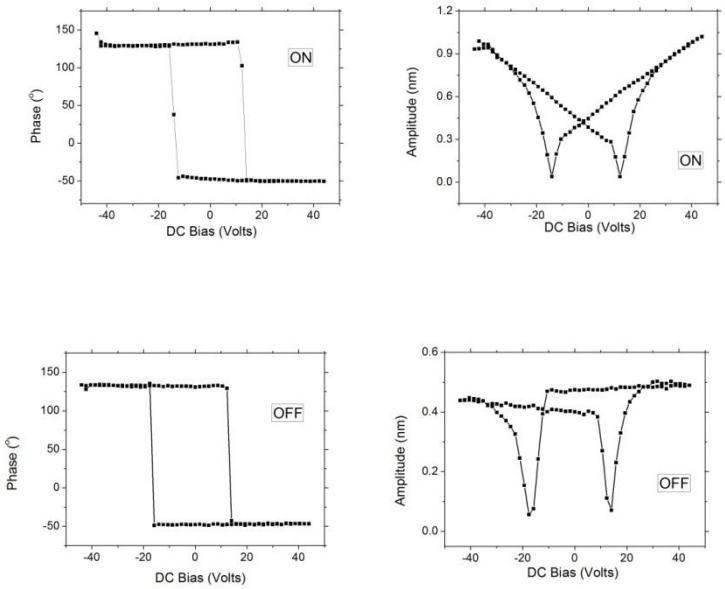

Figure 2.11 Typical "ON" and "Off" states hysteresis characteristics as a function of the bias voltage on the P(VDF-TrFE) thin film. Displayed are the phase (left) and amplitude (right).

After acquisition of data of the local domain switching at one location, the cantilever can be controlled to move to the next location, and the process is repeated until a mapping of evenly spaced points is acquired. The hysteresis loops are collected at each point. After analyzing all of the hysteresis loops for the whole scanned area, a distribution of the local switching properties can be obtained; this is the so-called switching spectroscopy piezoresponse force microsocopy (SSPFM)[14]. For example, SSPFM was

carried out on a porcine aortic wall and hysteresis and butterfly loops similar to those in Figure 2.6 were obtained on a fine grid of 32×32 points over a 2×2 um^2 area. The resulting mapping of the piezoresponse amplitude at zero DC voltage is shown in Figure 2.12, overlaid on a chain-like topographic structure. From the SSPFM results, the two dimensional maps of the positive and negative coercive voltages, as well as nucleation bias, can be obtained. A detailed study of the switching behavior of the aortic wall will be presented in Chapter 6.

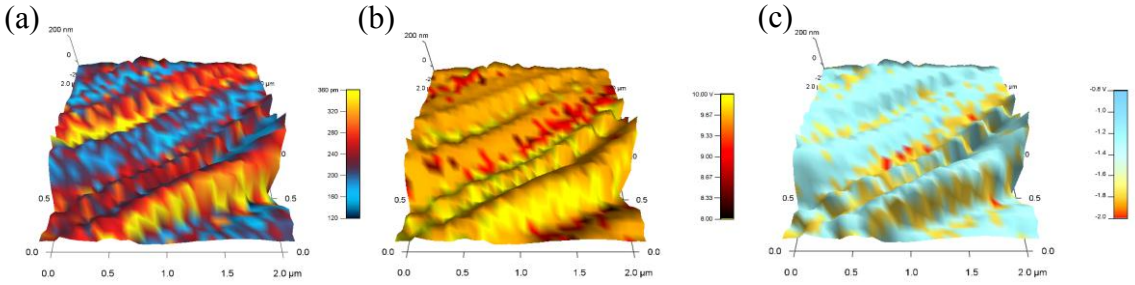

Figure 2.12 SSPFM mapping of the inner aortic wall by the PFM: remnant PFM amplitude (a), coercive voltage (b), and switching asymmetry (c) in a 2×2 μm^2 area.

2.2.5 Nanolithography

PFM can also been used as a *nanolithography* tool to write a pre-designed domain structure by applying a distribution of positive and negative voltages based on a template while scanning the sample. When the applied field is large enough, it can induce ferroelectric polarization reversal, and thus, pole the sample accordingly as designed. Using this method, it is possible to create domain arrays and more complex patterns in the sub μm range without changing the surface topography.

Here, we carry out nanolithography on the annealed P(VDF-TrFE) thin film using the University of Washington seal as a template to demonstrate such a concept, as shown in Figure 2.13. Positive or negative voltages, corresponding to the white and black area of the seal, are applied to the conductive AFM tip while scanning the area in the PFM nanolithography mode. The polarization is reorientated beneath the tip when the electric field exceeds the coercive field of the P(VDF-TrFE) film. Domains patterns in the 100 nm size range have been produced using this technique, as shown in Figure 2.13(b) and (c). Due to the small radius of the tip, the size of the engineered domain is limited by the crystalline structure of the material, allowing us to write a pattern with a feature size of 10s nanometers.

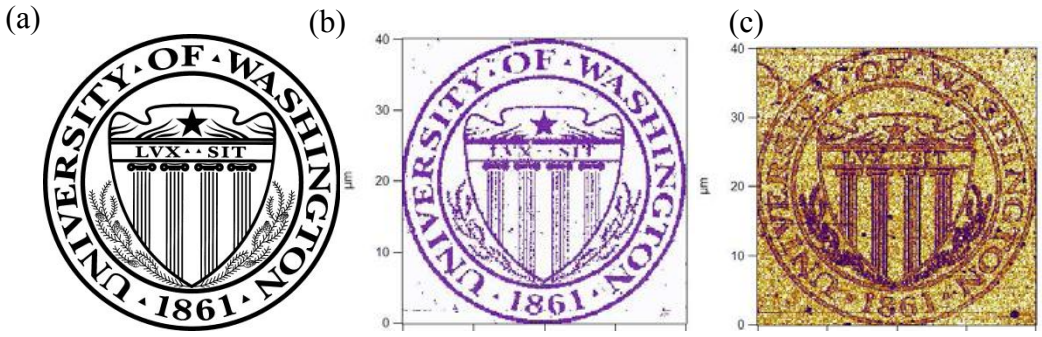

Figure 2.13 A 'UW' seal (a) that is patterned by the PFM nanolithography on the ferroelectric surface, as demonstrated by the PFM phase image (b), and the corresponding amplitude image (c).

2.3 Asylum MFP-3D PFM System

A commercial scanning probe microscopy (SPM) system in our Mutifunctional Materials Laboratory, Asylum Research (AR) MFP-3D system, is shown in Figure 2.14,

including the microscope head (Figure 2.14 (a)), controllers (Figure 2.14 (b)), and signal access module with an internal lock-in amplifier. The internal lock-in amplifier is used to perform quantitative characterizations by connecting with the SPM system. The signals from and to the microscope are acquired by the lock-in amplifier via the signal access module. The output data from the lock-in amplifier are retrieved, elaborated, and stored by the computer.

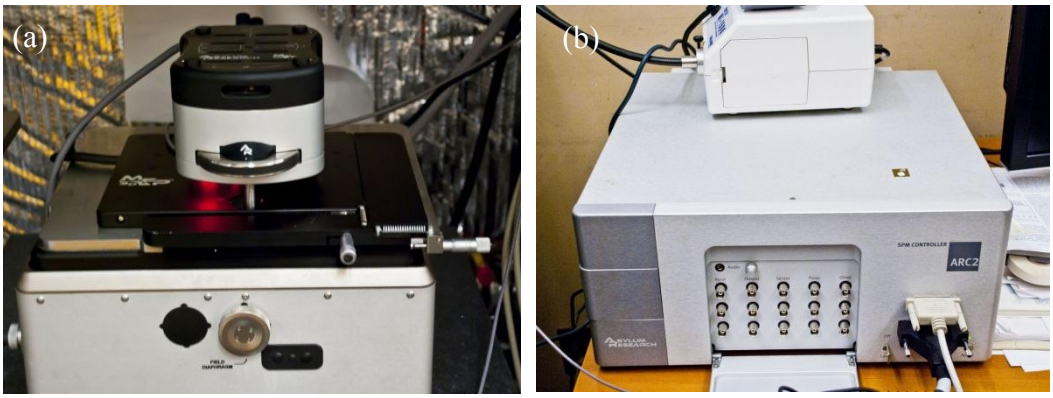

Figure 2.14 The atomic force microscope MPF-3D system from Asylum Research; the base and head (a) and the controller (b).

As shown in Figure 2.15, in PFM mode of the MFP-3D system, the applied driving bias is generated by the direct digital synthesizer (DDS) and linked to the "Chip", which is connected to the cantilever chip through the spring clip on most tip holders. The cantilever's deflection signal is connected to "InFast" in the controlling software and input to the Lock-in Amplifier. The R signal from the lock-in amplifier is also use as feedback to adjust the sensor Z. Finally, the PFM Phase and amplitude will be obtained after the digital signal processor.

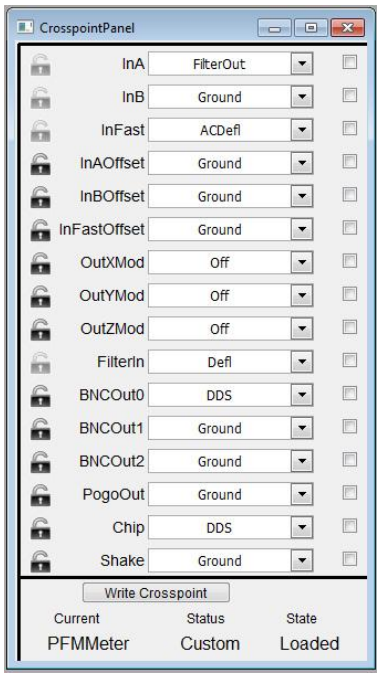

Figure 2.15 CrossPoint Panel in the AR MFP-3D system.

A typical PFM experiment procedure using the AR system is given as follows: The sample is loaded onto the sample holder, a NSC 18/Pt/ALBS (Pt coated tip with Al coated backside) cantilever is made by Umasch Co. with a 75 kHz frequency resonance, and a 3.5N/m spring constant is inserted to the cantilever holder. Then, the 'Asylum Research' software is launched, and the 'PFM'-'DART' mode is selected from the 'Mode Master' panel, with the 'Image Mode' set to PFM Mode. The light source is aligned to the appropriate position of the cantilever, and the deflection is adjusted to near zero. The engage process is started by pressing the engage button located in the 'Sum and Deflection Meter' panel, and the feedback loop is turned on. The head is lowered by turning the large front thumbwheel counter-clockwise until the tip approaches the sample

surface, with Z voltage around 70 volts. The DART Tuning parameters are set by pressing the ‘One Tune’ button, where the ‘Cantilever Tune’ window will appear and the software will look for the cantilever resonance frequency between the low and high tune values. Once the peak frequency and ‘Center Phase’ are selected, and the primary scan parameters, including: scan size, scan rate, scan speed, XY offset, scan angle, etc., are set, it is ready for PFM scan. The local piezoelectric response is detected as the first harmonic component of the tip deflection. The phase φ of the electromechanical response of the surface yields information on the polarization direction below the tip. The cantilever deformation is measured by laser deflection onto a four quadrant detector.

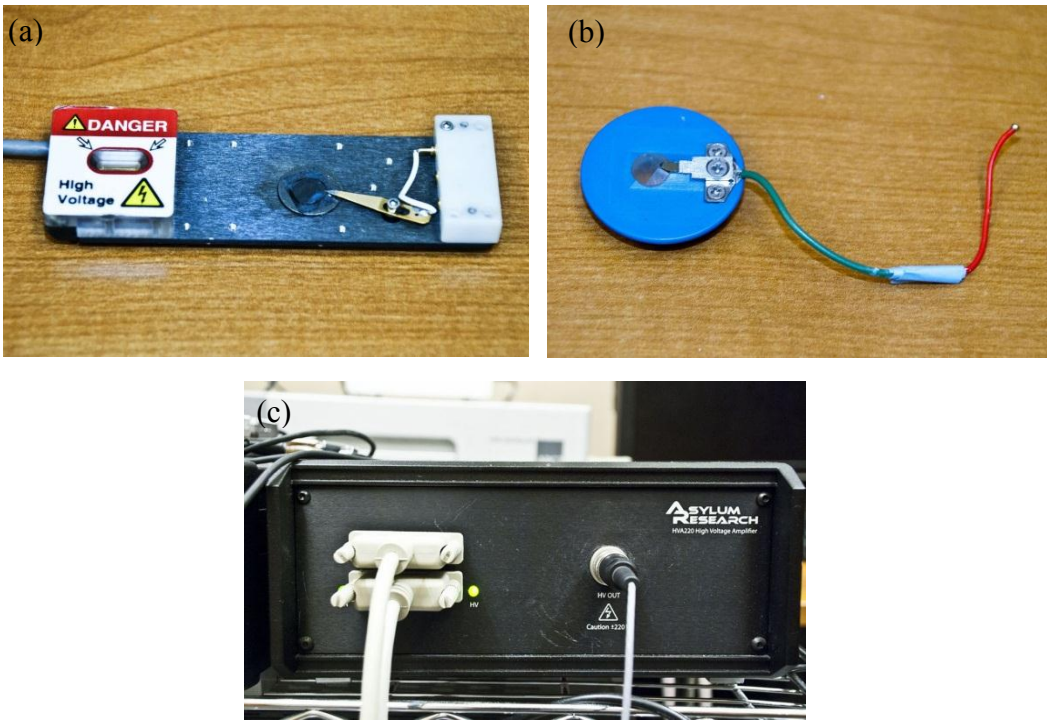

Figure 2.16 PFM sample holder (a), cantilever holder (b) and high voltage controller (c).

In additional to basic components, AR also developed several other important accessories. PFM requires detection of small tip displacements induced by relatively high amplitude and high frequency voltages, for which AR developed a *high voltage PFM module*, including specially designed head and the high voltage sample holder, as shown in Figure 2.16. This module enables high voltage PFM measurements up to 220V. In addition, AR developed a *PolyHeater*, shown in Figure 2.17, which is a modular heating stage designed specifically for elevated temperature studies from ambient to 300° C in the air or a controllable gaseous environment. It supports samples of up to 20 mm in diameter. The heating stage was controlled by the environmental controller. The polyheater can be used in combination with the high voltage PFM module, allowing us to study ferroelectric materials at elevated temperatures.

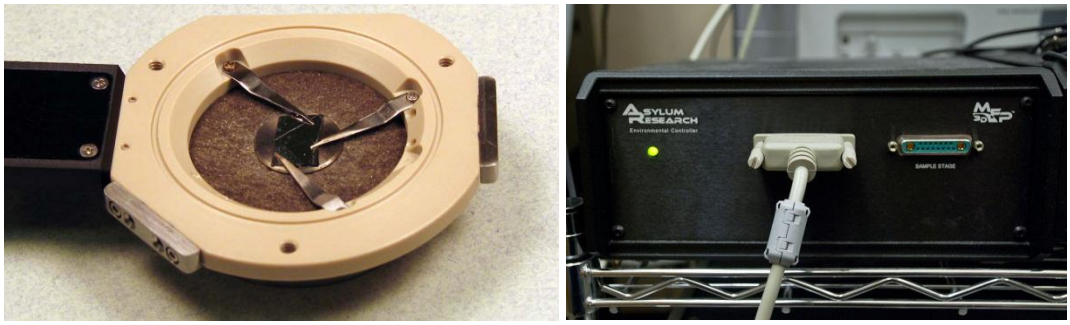

Figure 2.17 Picture of the PolyHeater (left) and environmental controller (right) for MPF-3D system from the Asylum Research.

Reference

1 G. Binnig, H. Rohrer, C. Gerber, and E. Weibel, Applied Physics Letters **40,** 178 (1982).

2 A. Gruverman, O. Auciello, and H. Tokumoto, Integrated Ferroelectrics **19,** 49 (1998).

3 J. Seidel, S. Grafstrom, C. Loppacher, S. Trogisch, F. Schlaphof, and L. M. Eng, Applied Physics Letters **79,** 2291 (2001).

4 T. Hidaka, T. Maruyama, M. Saitoh, N. Mikoshiba, M. Shimizu, T. Shiosaki, L. A. Wills, R. Hiskes, S. A. Dicarolis, and J. Amano, Applied Physics Letters **68,** 2358 (1996).

5 A. Gruverman, O. Auciello, R. Ramesh, and H. Tokumoto, Nanotechnology **8,** A38 (1997).

6 G. Binnig, C. F. Quate, and C. Gerber, Physical Review Letters **56,** 930 (1986).

7 N. Geisse, Asylum Research. Retrieved 2 (September 2011).

8 Q. Zhong, D. Inniss, K. Kjoller, and V. B. Elings, Surface Science **290,** L688 (1993).

9 J. M. R. Weaver and D. W. Abraham, Journal of Vacuum Science & Technology B **9,** 1559 (1991).

10 M. Nonnenmacher, M. P. Oboyle, and H. K. Wickramasinghe, Applied Physics Letters **58,** 2921 (1991).

11 A. Gruverman and S. V. Kalinin, Journal of Materials Science **41,** 107 (2006).

12 S. V. Kalinin, A. Gruverman, B. J. Rodriguez, J. Shin, A. P. Baddorf, E. Karapetian, and M. Kachanov, Journal of Applied Physics **97** (2005).

13 B. J. Rodriguez, C. Callahan, S. V. Kalinin, and R. Proksch, Nanotechnology **18,** 475504 (2007).

14 S. Jesse, A. P. Baddorf, and S. V. Kalinin, Applied Physics Letters **88** (2006).

15 S. Jesse, S. V. Kalinin, R. Proksch, A. P. Baddorf, and B. J. Rodriguez, Nanotechnology **18** (2007).

16 Q. M. Zhang, W. Y. Pan, and L. E. Cross, Journal of Applied Physics **63,** 2492 (1988).

17 L. M. Eng, Nanotechnology **10,** 405 (1999).

18 S. V. Kalinin, B. J. Rodriguez, S. Jesse, J. Shin, A. P. Baddorf, P. Gupta, H. Jain, D. B. Williams, and A. Gruverman, Microscopy and Microanalysis **12,** 206 (2006).

19 J. E. Sader, Journal of Applied Physics **84,** 64 (1998).

Chapter 3 Piezoresponse Force Microscopy of Perovskite Ferroelectric Materials

This chapter focuses on experiments that use various PFM techniques, which are introduced to better understand the piezoelectric response and polarization switching behavior of perovskite ferroelectric thin films and single crystals at the nanoscale level. In chapter 2, we briefly discussed PFM experiments on ferroelectric materials. Now, we will characterize piezoelectricity and ferroelectricity of epitaxial $BiFeO_3$ thin films and PMN-PT single crystals by simultaneously imaging the surface morphology, the phase and magnitude of the piezoelectric response, as well as the piezoresponse hysteresis. The intricate domain structures will be unraveled, and the polarization switching dynamics will be discussed.

3.1 Epitaxial $BiFeO_3$ thin film

Bismuth ferrite ($BiFeO_3$), a so-called multiferroic material, is an inorganic chemical compound with a perovskite structure[1-3]. It exhibits rare room temperature multiferroicity, with a ferroelectric Curie temperature of around 830^{o}C, and an antiferromagnetic Neel temperature of around 370^{o} C[4]. Naturally, it simultaneously shows antiferromagnetic and ferroelectric orders with the corresponding transition temperatures well above room temperature, which is promising for a broad range of applications in data storage, sensors,

and actuators. In addition, $BiFeO_3$ is a good environmentally friendly ferroelectric material compared to traditional Pb-based ferroelectrics.

The implementation of $BiFeO_3$ in non-volatile memory applications, is critically dependent on understanding its ferroelectric domain structure and polarization switching dynamics. In this section, we carry out PFM to investigate the domain structures of (001) oriented epitaxial $BiFeO_3$ films. The thin film has only around a 100 nm thickness and domain size. PFM is an attractive method capable of directly probing its piezoelectricity and ferroelectricity at the nanoscale level.

3.1.1 PFM of Epitaxial Thin Films

A 100 nm thick (001) oriented $BiFeO_3$ film on a 20 nm thick $LaSrMnO_3$ (LSMO) deposited on a $TbScO_3$ substrate was provided by Prof. Xiaoqing Pan at the University of Michigan. The LSMO thin film on the $TbScO_3$ substrate acts as a bottom electrode. Using the DFRT technique, a strip-like ferroelectric domain structure was observed in the out-of-plane vertical PFM modes, as shown in Figure 3.1. The amplitude and phase of the polarization domains, as well as the topography and the resonant frequency, are imaged simultaneously. The information provided by the amplitude image (Figure 3.1 (b)) reveals the magnitude of the piezoresponse, which clearly shows two tones, with the blue strips representing a low piezoresponse, indicating the presence of domain walls. The

phase image (Figure 3.1 (c)) provides information about the direction of the vertical component of the polarization. The yellow and purple stripes arranged alternatively represent a phase value of 71^{o} and 109^{o}, respectively; thus, the two domain types are 180^{o} apart in the phase. Furthermore, it is observed that the topography mapping (Figure 3.1 (a)) shows an ultra-flat surface that is only 2 nm in roughness, and the frequency mapping (Figure 3.1 (d)) indicates small variations in film stiffness.

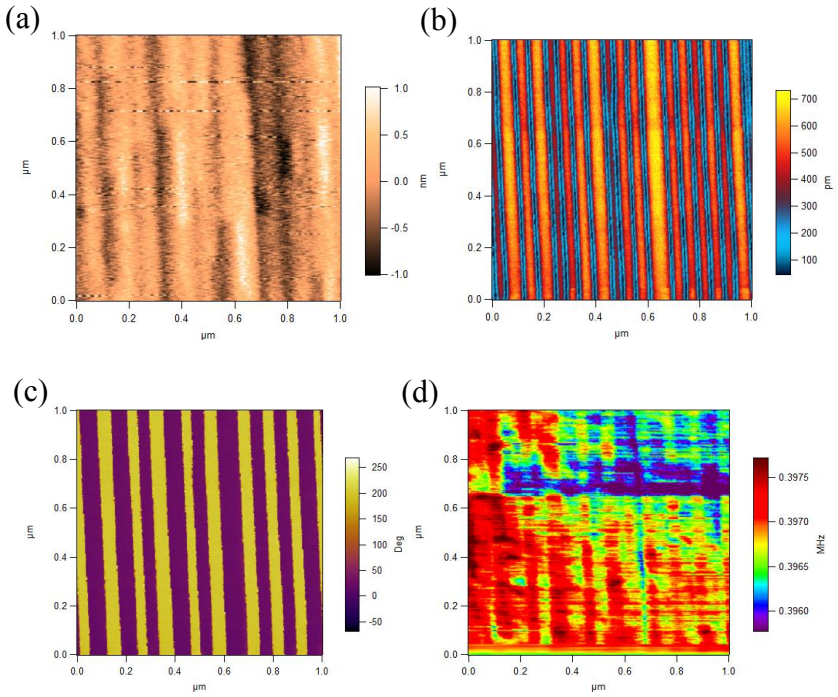

Figure 3.1 PFM images of 1×1 µm^2 epitaxial $BiFeO_3$ thin film: (a) topography, (b) amplitude, (c) phase, and (d) frequency.

As is discussed in Chapter 2, PFM can be employed to identify the external electric field-induced polarization switching. As such, we carried out nanolithography on the $BiFeO_3$ thin film using a square template to confirm its ferroelectricity. Such an approach

is illustrated in Figure 3.2 (a). To locally switch the polarization, a positive or negative 44 V DC bias was applied to the conductive PFM tip while scanning over the 1.0 ×1.0 μm area corresponding to the white and black area of the pattern (Figure 3.2 (a)). The polarization is reorientated beneath the tip when the electric field exceeds the coercive field of $BiFeO_3$, making it possible to pattern a polarization pattern based on the template.

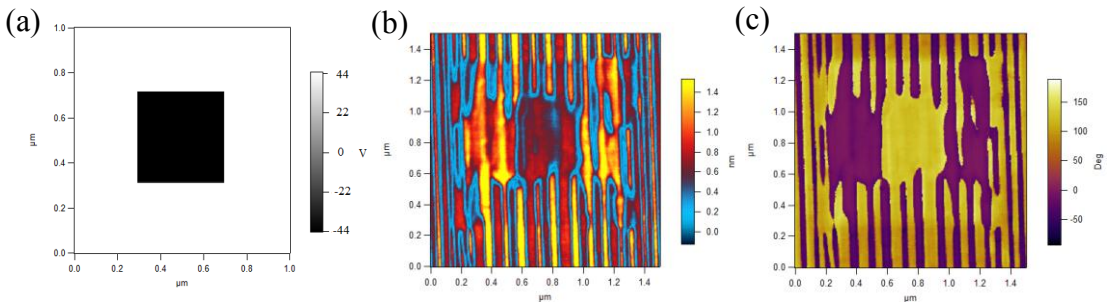

Figure 3.2 PFM lithography of epitaxial $BiFeO_3$ thin film: (a) bias template, (b) amplitude, and (c) phase.

After PFM lithography, amplitude and phase scans were performed to confirm the switching. The poled area is conspicuous in the PFM amplitude and phase images, as shown in Figure 3.2. It should be noted that the purple and yellow regions in the vertical PFM phase image (Figure 3.2 (c)) are domains with upward and downward out-of-plane polarization components, respectively. The modification of the domain pattern, as seen in Figure 3.2 (b), is due to polarization switching. As is shown in the phase image after poling, we were able to switch the central square completely, but part of the outer square remains unswitched, wherein the strip domains are still visible. This may be due to domain wall pinning by various defects in these regions.

We also examined the switching characteristics of the $BiFeO_3$ film by applying a sequence of DC voltages in a triangular wave form to switch its polarization, while simultaneously examining its piezoresponse by imposing an AC voltage. Typical phase-voltage hysteresis and amplitude-voltage loops are obtained, as shown in Figure 3.3, in the second cycle. Both small coercive voltage and clear 180^o switching were found. Such small coercive voltage is particularly important for data storage applications, as they require small voltage and power for data writing.

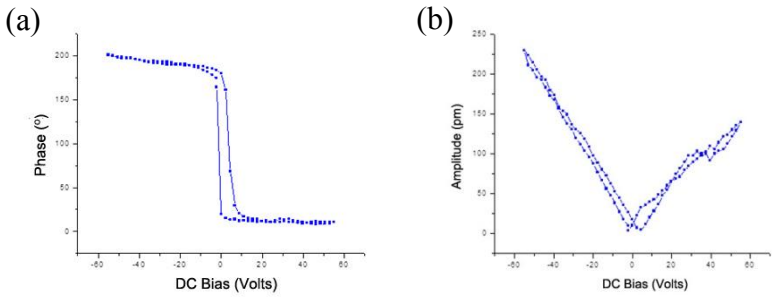

Figure 3.3 PFM "OFF" states hysteresis characteristics as a function of the bias voltage on the $BiFeO_3$ thin film. The phase (left) and amplitude (right) are displayed.

3.1.2 Domain Growth Dynamics of Epitaxial $BiFeO_3$ Thin Films

To gain further insight into the domain switching of the $BiFeO_3$ thin film, a bare surface sample was used to perform local ferroelectric switching and imaging with a stationary conductive tip as the top electrode, as shown in Figure 3.4 (a). Several studies have been carried out. For the first case, we keep the dwell time at 2s, which is the time that the tip remains in contact with the surface at each point. A sequence of biases were

then applied to the tip during each writing, from 11 V at the lower left corner, to 44 V at the upper right corner. Immediately after that, the area was scanned several times by the PFM mode. All the operations were performed in the air. The domain visualization was realized by applying an AC driving voltage of 1.1 V (much lower than the coercive field, a threshold for polarization inversion) through the conductive tip while scanning the surface. The DFRT technique was used to enhance sensitivity and minimize the cross-talk with topography. The PFM phase images corresponding to the instantaneous domain configurations after the polarization reversal for the different applied biases are presented in Figure 3.4b. It should be noted that the domain switching starts when bias reaches 33 V with a 2s exposed time. Furthermore, the polarization area switched by the bias of 44 V is slightly larger than 33 V. It is also observed that domains produced by a biased tip exhibit isotropic growth behavior consistent with the isotropic growth of the domains observed in the thin film in the high field range.

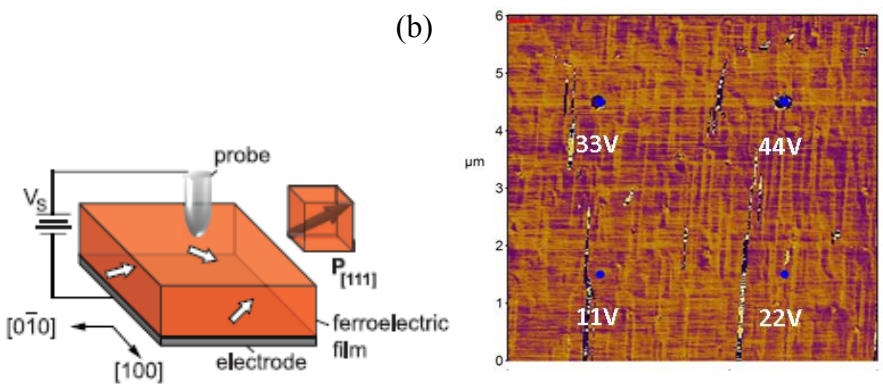

Figure 3.4 Thin film ferroelectric switching by a surface probe. (a) Schematic of local PFM switching, (b) An out-of-plane PFM phase image shows the reversed downward poled domain formed by application of bias to a probe on the surface of the 100nm $BiFeO_3$ film.

For the second case, we kept the same bias of 11 V and increased the exposed time gradually from 2s to 18s, as marked in Figure 3.5 (a). To compare local electromechanical response measured in two kinds of local switching experiments, this study was conducted on the same area as the previous one. The size of the ferroelectric domain formed below the tip varies with different bias and exposed time. From the phase image, very small size area was switched at the exposed time of 6s, and the size increased slightly until the exposed time reaches 12s. It is also observed that the domains shape under a small bias with a long exposed time is irregular when compared to a larger bias.

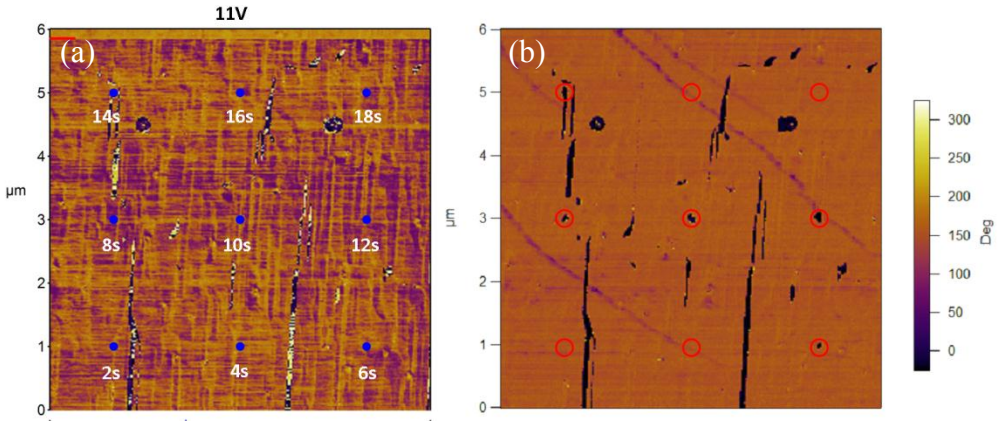

Figure 3.5 (a) Location marks on pre-scan phase image, (b) An out-of-plane PFM phase image of different exposed time to a probe on the surface of the $BiFeO_3$ film.

A finer measurement was carried out over a new area. The bias starts from 11 V at the left bottom corner and ends at 44 V at right up corner with a constant exposed time of 2s, as marked in Figure 3.6 (a). Compared to the topography before the lithography shown in Figure 3.6 (a), dramatic changes in the height at marked locations are observed after the lithography, as shown in Fig. 3.6 (b). From the PFM amplitude and phase (Figure 3.6 (c) and (d)) mappings, the domain begins to switch at the bias of 28.6 V, and the switching area becomes more significant when the bias reaches 33 V, which is consistent with the previous results. On the other hand, the shape of the switched domain is round, with a diameter of 200 nm when the bias is larger than 33 V. There is no obvious difference when the bias is increased after that, indicating that the size of the ferroelectric domain formed is stable when the localized bias is larger than a critical value. Figure 3.7 (a) and (b) show images of the red squared area of Figure 3.6 (a).

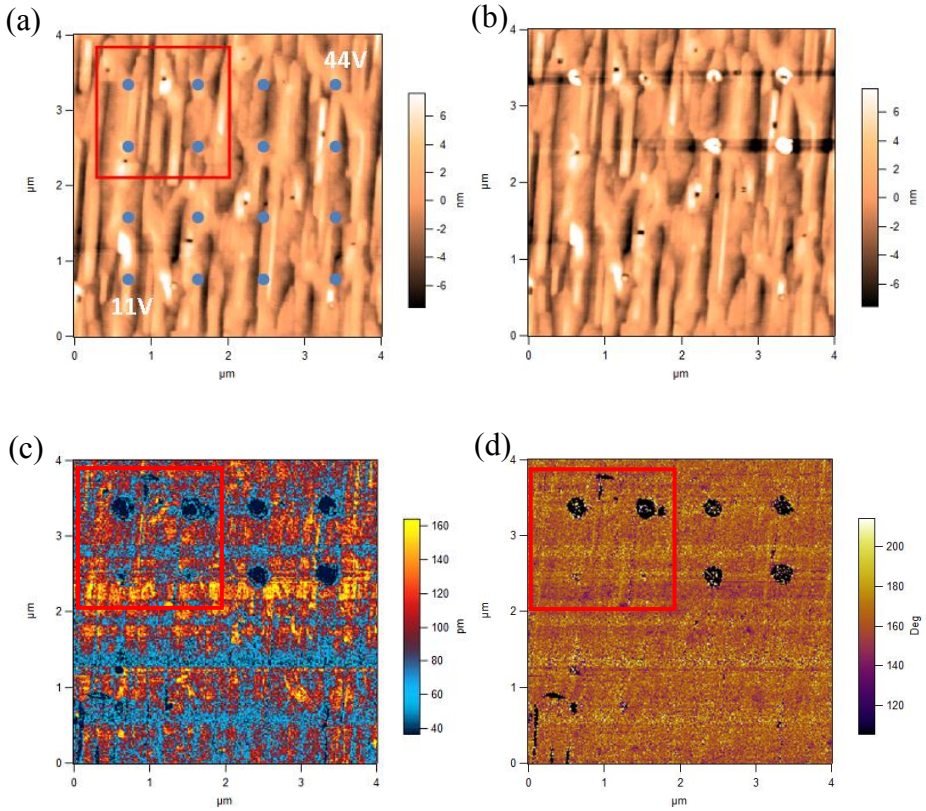

Figure 3.6 (a) Location marks on the pre-scan phase image, (b) topography after domain switching, (c) an out-of-plane PFM amplitude image, and (d) phase image of different exposed time to a probe on the surface of the $BiFeO_3$ film.

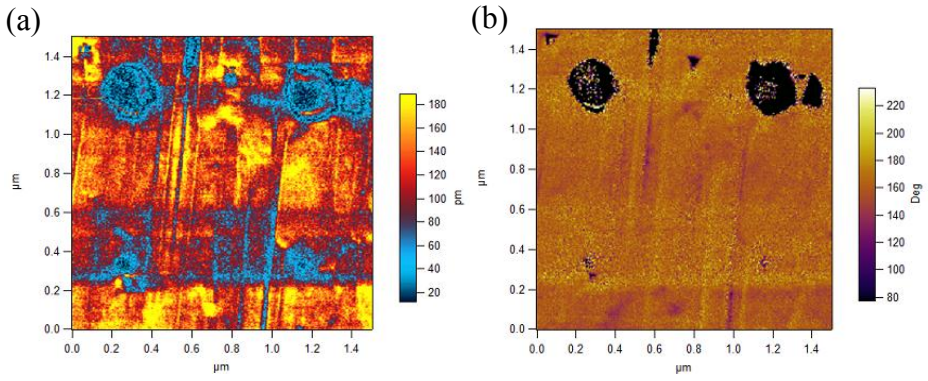

Figure 3.7 A second PFM scan over the red region in Figure 3.6: (a) PFM amplitude image and (b) phase image.

3.2 PMN-PT Single Crystal

Recently, the study of relaxor-based ferroelectric single crystal PMN-PT has attracted a great deal of attention, primarily due to their high piezoelectric coefficient and electromechanical coupling factor. The mechanism responsible for the excellent properties of PMN/PT was suggested to be domain engineering[5-7], polarization rotation[8], and induced metastable phases, such as an orthorhombic phase[9] or a monoclinic phase. In this section, we will investigate the PMN-PT single crystals using PFM. It is believed that this kind of study will be useful in deepening the understanding of the microstructure and the properties of PMN-PT single crystals.

The domain structure of various compositions of PMN-PT in (001) the crystal orientation has been observed by Bai, et al[10]. In this section, we will carry out the PFM study on structures of ferroelectric domains, domain switching behavior, domain evolution under the influence of temperature, as well as aging. The PFM amplitude and phase images reveal the [001] orientation and the evolution of the domain structure during the complicated phase transition under different temperatures.

3.2.1 Domain Structrue of PMN-PT

DFRT techniques have been applied to determine the out-of-plane and in-plane polarization distribution. Figure 3.8 shows the vertical PFM images of the grown (001)-

cut PMN-30%PT crystal, where the ferroelectric domains were observed. PMN-30%PT was selected for PFM investigation due to the fact that this composition corresponds to morphotropic phase boundary and possesses excellent piezoelectric properties.

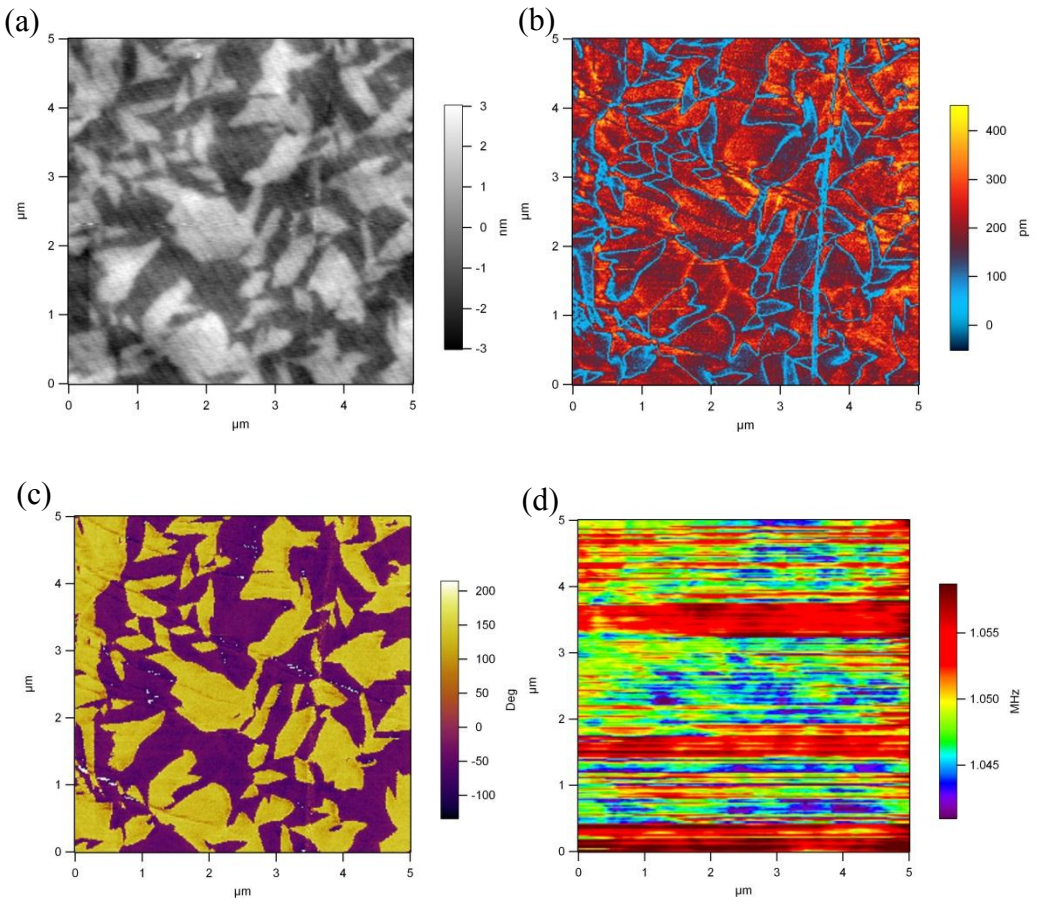

Figure 3.8 PFM images of the 1×1 μm^2 epitaxial PMN-30%PT single crystal: (a) topography, (b) amplitude, (c) phase, and (d) frequency.

In the PFM results, the topography image (Figure 3.8 (a)) corresponds to the domain structures very well. The higher region in the topography correspond to the bright PFM phase region. It is also observed that at the boundary between two different polarization domains (i.e., domain walls), the amplitude signal drops significantly. By comparing the

amplitude and phase images (Figure 3.8 (b) and (c)), a very nice correspondence is clearly shown, and it should also be noted that when crossing the oppositely polarized domains, the amplitude values are similar to each other. In addition, the PFM resonance frequency mapping reflects the variation of contact stiffness of the tip-surface junction and the local mechanical properties

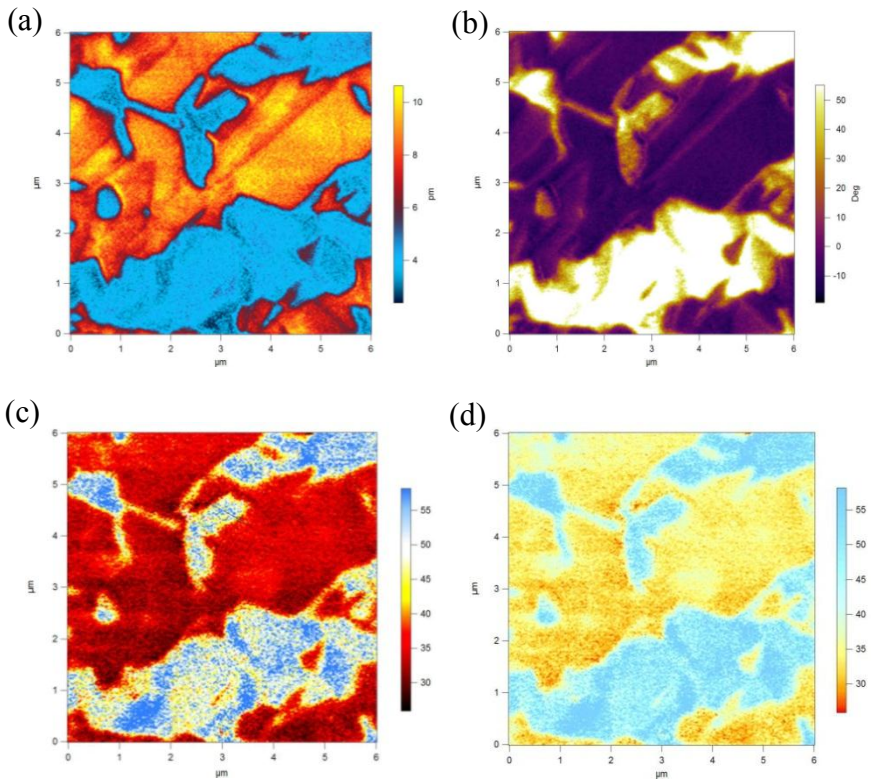

Figure 3.9 The PFM amplitude image (a), phase image (b), mappings of the resonance amplitude corrected by thequality factor (c), and mappings of the resonance phase corrected by the quality factor (d).

The DFRT technique was adoped to make it possible to quantitatively determine its intrinsic piezoelectric coefficient. Using such a technique, we re-examined the piezoresponse of the PMN-30%PT single crystal, as shown in Figure 3.9. The PFM

amplitude contrast is clearly observed in Figure 3.9 (a) and corresponds to the phase mapping in Figure 3.9 (b) very well, indicating different polarity of domains. The intrinsic piezoresponse of the sample can now be determined by correcting the quality factor, making it possible to map the spatial distribution of the piezoelectric coefficient, d_{33}, quantitatively, as shown in Figure 3.9 (c) and (d). It is observed that the maximum piezoresponse amplitude after the correction is only 55 pm, and the intretisic piezoelectric coefficient is estimated to be 20 pmV^{-1}.

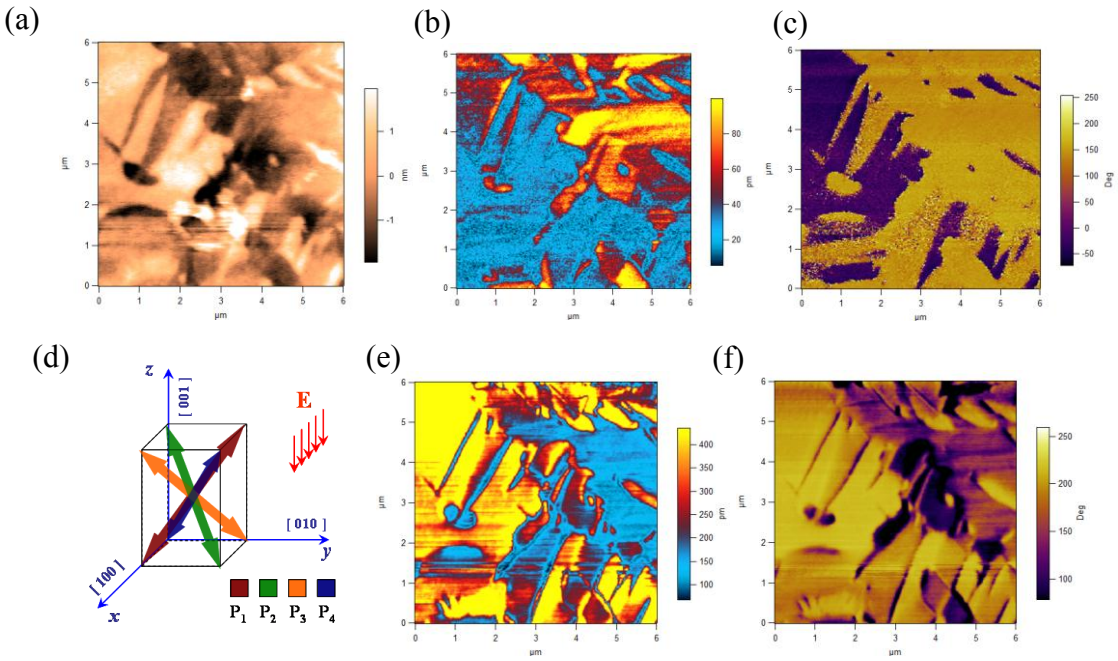

Figure 3.10 (a) Topography, (b) the vertical PFM amplitude image, (c) vertical phase image, (d) the schematic diagram of 4 polar direction in rhombohedral unit cell, (e) lateral PFM amplitude image, and (f) lateral PFM phase image.

For three dimensional domain analysis, vertical and lateral PFM techniques have been applied to determine the out-of-plane and in-plane polarization distributions

simultaneously. Figure 3.10 presents the experimental results on the simultaneous acquisition of vertical and lateral piezoresponse images, as well as the topography of PMN-PT. The stronger lateral amplitude image, as shown in Figure 3.10 (e), suggests the in-plane orientation of the polarization vector. It should also be noted that the amplitude and phase images correspond to each other very well for both vertial and lateral PFM images, and those images present domain structures along two directions of the PMN-PT. In addition, it is interesting to note that for the out-of-plane amplitude image, there is a large blue region with low vertical piezoresponse amplitude, which corresponds to a large in-plane piezoresponse, as shown in Figure 3.10 (e), indicating that the polarization of this region is primarily in-plane instead of out-of-plane. Schematical image of the structure of the rhombohedral PMN-PT in Figure 3.10 (d) will be helpful to understand the piezoresponse. The phase images (Figure 3.10 (c) and (f)) provide a great deal of information about the direction of polarization in the domains, but scans along different crystallographic directions are necessary to completely reconstruct the vector direction.

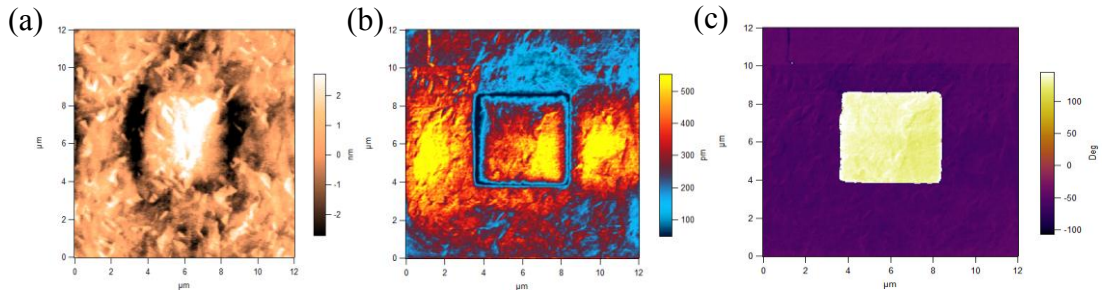

Figure 3.11 A square pattern that is patterned by PFM nanolithography on the ferroelectric surface, as demonstrated by: (a) topography, (b) PFM amplitude image, and (c) the corresponding phase image.

The nanolithography mode of a PFM was used to write ferroelectric domain patterns on the PMN-PT single crystal, where DC voltages of -66 and 66 V were applied to the conductive tip according to the predetermined pattern while scanning the sample surface, which poled the sample into different polar domains. The polarization is reorientated beneath the tip when the electric field exceeds the coercive field of the PMN-PT single crystal. The piezoresponse of the out-of-plane amplitude and phase images are revealed, as shown in Figure 3.11.

This poled domain structure is not energetically stable; therefore, the depolarization usually occurs when time increases. We carried out continous PFM scans over the poled area of PFM lithography to study time-dependent depolarization. Figure 3.12 presents the stable PFM images on the simultaneous acquisition of the vertical and lateral piezoresponse of the same area as Figure 3.11 after 4 times scan (20 mins).

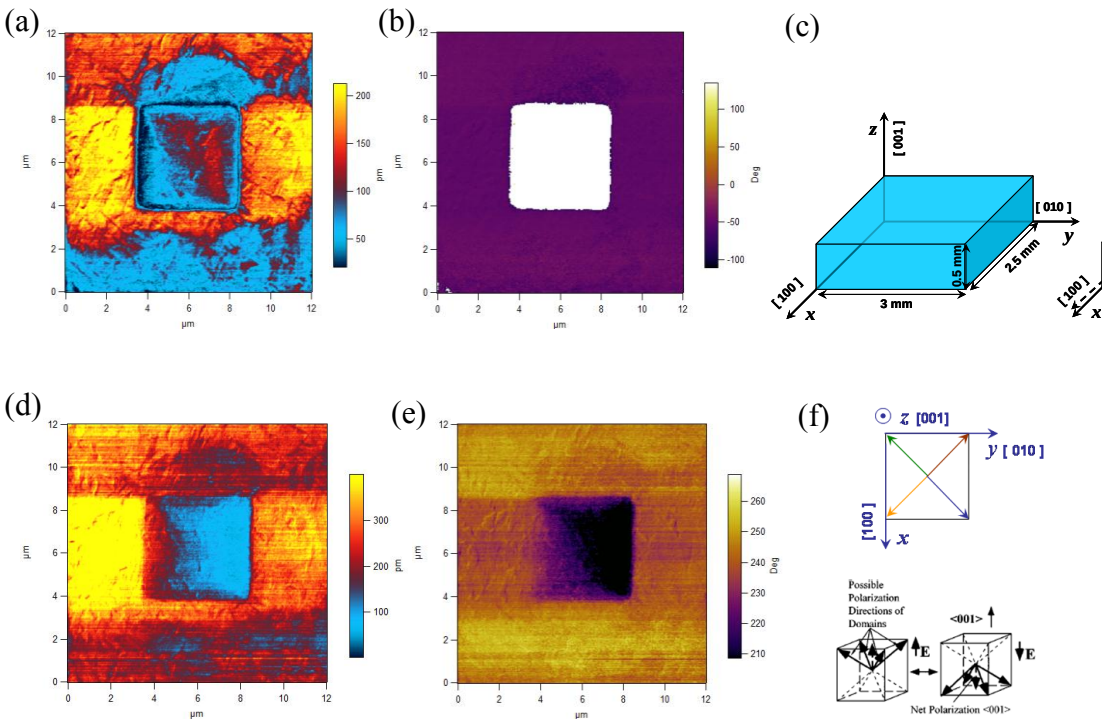

Figure 3.12 Stable PFM results after lithography, (a) vertical PFM amplitude image; (b) vertical phase image, (c) lateral PFM amplitude image, (d) lateral PFM phase image, (e) the schematic sample dimension, and (f) schematics of possible polar diretions after upward and downward poling.

It should be noted that the amplitude and phase images correspond to each other very well for vertial PFMs, and the downward poled area (inside square) shows very low pizoresponse, but clear phase contrast. Furthermore, the weaker lateral amplitude image and clear trianglar dark phase area, as shown in Figure 3.12 (c) and (d), suggests in-plane orientation of the polarization vector. To understand the polarization configuration, we first assumed that the domains with an upward P_i^+ and downward P_i^- polarizations give rise to opposite contrasts in vertical PFM (white and dark) respectively, as schematically shown in the structure of PNM-PT single crystal in Figure 3.12 (f). It should be noticed

that the PFM cantilever is oriented along [010]. Secondly, domains with polarization vectors along the cantilever's long axis do not give rise to lateral PFM signal for they do not produce any torque required for lateral imaging. Thirdly, domains with polarization pointing to the right direction with respect to the cantilever's long axis will produce a bright lateral phase, and domains with polarization pointing to the left direction appear dark in lateral PFM. Then, the polarization switching can be identified by vertical PFM phase contrast changes. It is concluded that the unchanged brigher tone of the inside square (left part triangular) corresponds to $P_1 \rightarrow P_3^-$ (71° switching), the light to dark corresponds to $P_4^+ \rightarrow P_3^-$(109° switching), and all dark to white corresponds to $P_1^- \rightarrow P_1^+$ (180° switching). Therefore, we can identify all three possible polarization switching processes (71°, 109°, and 180°) by comparing the vertical PFM images acquired before and after poling. It is interesting to note that ferroelastic switching of 71° and 109° is generally not observed in this structure.

A larger vertical PFM scan presents the domain configuration of the poled and unpoled area, as shown in Figure 3.13. The out-of-plane PFM images indicate that the boundary between the regions are biased by the surface probe at the positive (outer square) and negative (inner square), as well as the poled region and unpoled region. The change in phase (color), but not amplitude (height), indicates a 180° rotation. Those domain boundaries do not follow the template perfectly. This may be due to the domain

wall pinning by various defects in these regions.

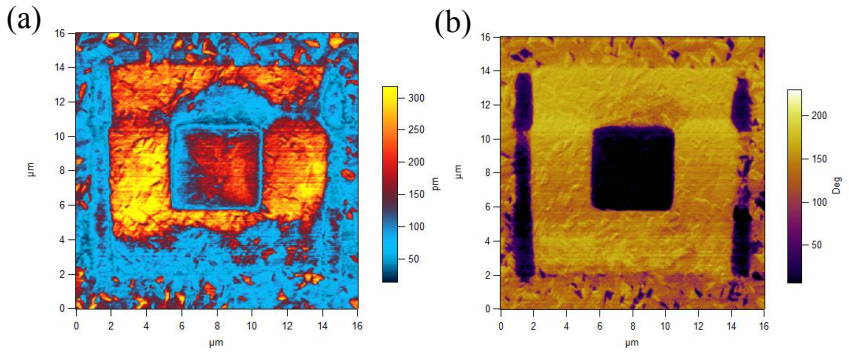

Figure 3.13 Large scan over the area after PFM lithography of PMN-30%PT single crystal: (a) amplitude, and (b) phase.

To investigate the domain switching in the PMN-PT single crystal, we apply a sequence of DC bias imposed by a 1.0 V AC driving voltage to the PNM-PT single crystal, with the AC driving voltage set to be much smaller than the coercive voltage to avoid interference with switching instability. The hysteresis and butterfly loops are shown in Figure 3.14, which are measured in "OFF" states to minimize the electrostatic interaction. The actual remnant piezoresponse is detected, so the retention characteristics of the ferroelectric are revealed. The cyan and magenta curves are obtained from the first and second cycle respectively. From the hysteresis loop and butterfly loop, the coercive voltage can be estimated as 22.5 V. The hysteresis loop is nearly symmetric, indicating that the PMN-PT does not show any significant macroscopic imprint, which is the tendency of one polarization state to become more stable than the opposite. There does not appear to be a preference for positive or negative domains in the PMN-PT single

crystal.

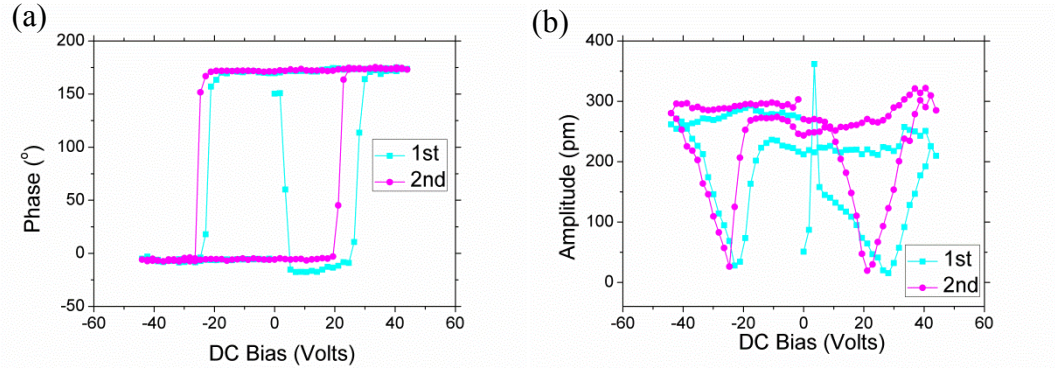

Figure 3.14 PFM "OFF" states hysteresis characteristics as function of the bias voltage on PMN-PT single crystal. Displayed are the phase (left) and amplitude (right).

To study the dynamics of the domain walls while the domain switches with a high resolution, the PFM step lithography mode was employed; a DC bias voltage was applied while contacting the conductive tip on the sample surface. By this mode, we investigated the coercive voltage and domain dynamics of the PMN-PT single crystal. First, we kept the dwell time at 2s at each point, a sequence of biases were then applied to the tip during each write from 0.44 V at location '1', to 4.4 V at location '16' (Figure 3.15 (a)). Immediately after that, the area was scanned in the PFM mode several times. Domain visualization was realized by applying an AC driving voltage, ranging from 0.22 to 0.66 V, through the conductive tip while scanning the surface. The PFM phase images corresponding to the instantaneous domain configurations during polarization reversal for different applied biases are presented in Figure 3.15. From the PFM phase image (Figure 3.15 (c)), the domain switching appears at location '12', where the bias is 3.34 V with a

2s exposed time. The polarization area switched by the bias of 4.4 V is slightly larger than the 3.34 V. A clear domain was created at location '15' (as shown in Figure 3.15 (b)), where the diameter of the dot-sized domains is around 60 nm.

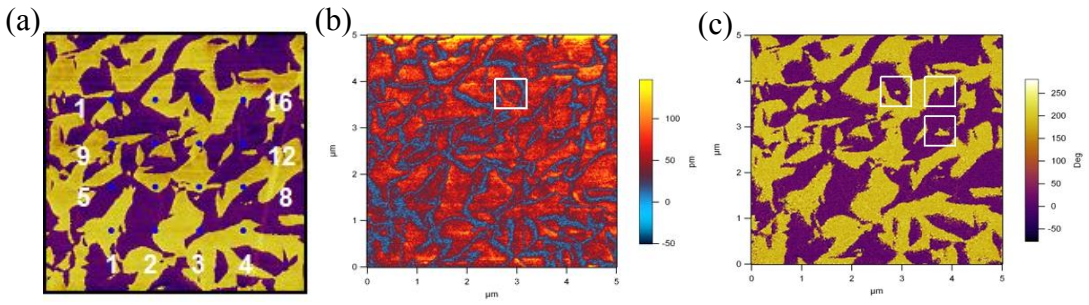

Figure 3.15 Ferroelectric switching of the PMN-PT by a surface probe. (a) Location marks on pre-scan phase image, (b) out-of-plane PFM amplitude image, and (c) phase image.

3.2.2 Temperature-dependent Domain Evolution in PMN-PT Single Crystal

PMN-PT has a complex perovskite structure with an ABO_3-type unit cell and exhibits a diffused ferroelectric phase transition in a wide temperature range. In this section, we will examine the piezoelectric and ferroelectric properties of the microscopically poled PMN-PT single crystal at a series of temperatures approaching phase transition using PFM, in combination with single and DFRT techniques, respectively. The temperature-dependent ferroelectric domain structure and evolution under DC bias was then be studied.

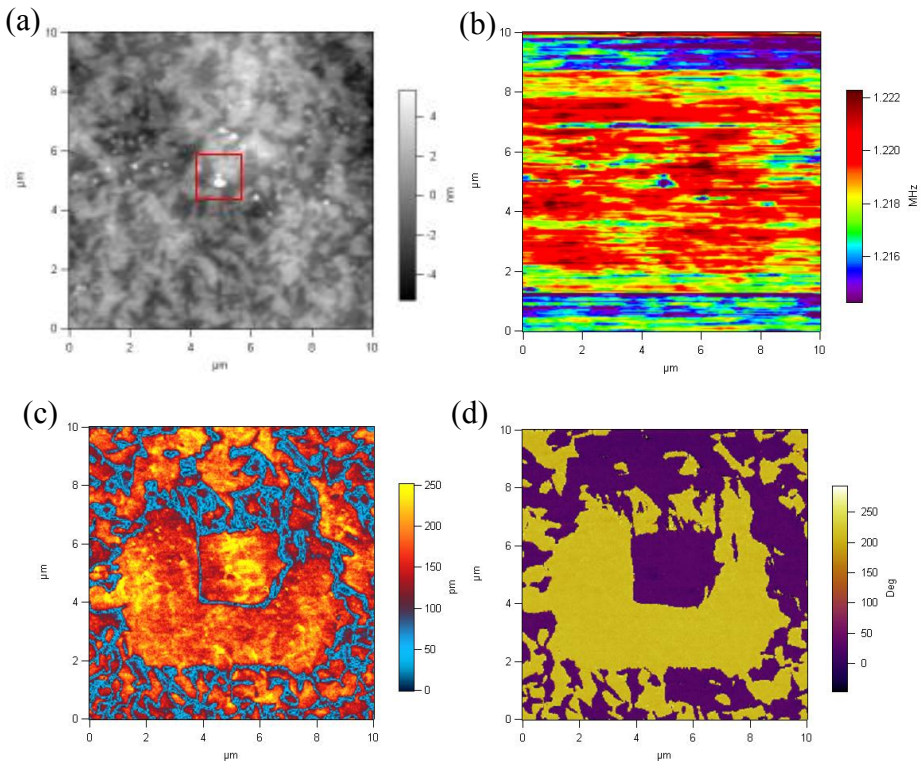

Figure 3.16 Square domain pattern after the PFM lithography, (a) topography, (b) mapping of frequency, (c) amplitude image, and (d) phase image.

Nanolithography mode of scanning probe microscopy was used to write ferroelectric domain patterns on a PMN-PT single crystal. DC voltages of -20 V and 20 V were applied to the conductive tip according to the predetermined pattern while scanning the sample surface, which poled the PMN-PT into different polar domains. PFM phase and amplitude images were observed at RT first, and then again after they were subjected to the thermal process. The sample was heated to different temperatures of up to 200^{o}C using an Asylum Research polyheater. Each of the temperature steps were maintained for 10 min, and then the crystal was cooled down to RT naturally by turning off the heater.

The temperature on the surface of the sample was measured and calibrated by the thermocouple (Fluke 52 K/J Thermalmeter). The DFRT technique was also used where the AC voltage of 2.2 V was applied to the conductive tip while scanning the sample surface under two frequencies of 323kHz±5kHz near the resonance, which generated two piezoresponse amplitudes during tuning process. This allows tracking resonances while scanning over the samples with varying stiffness.

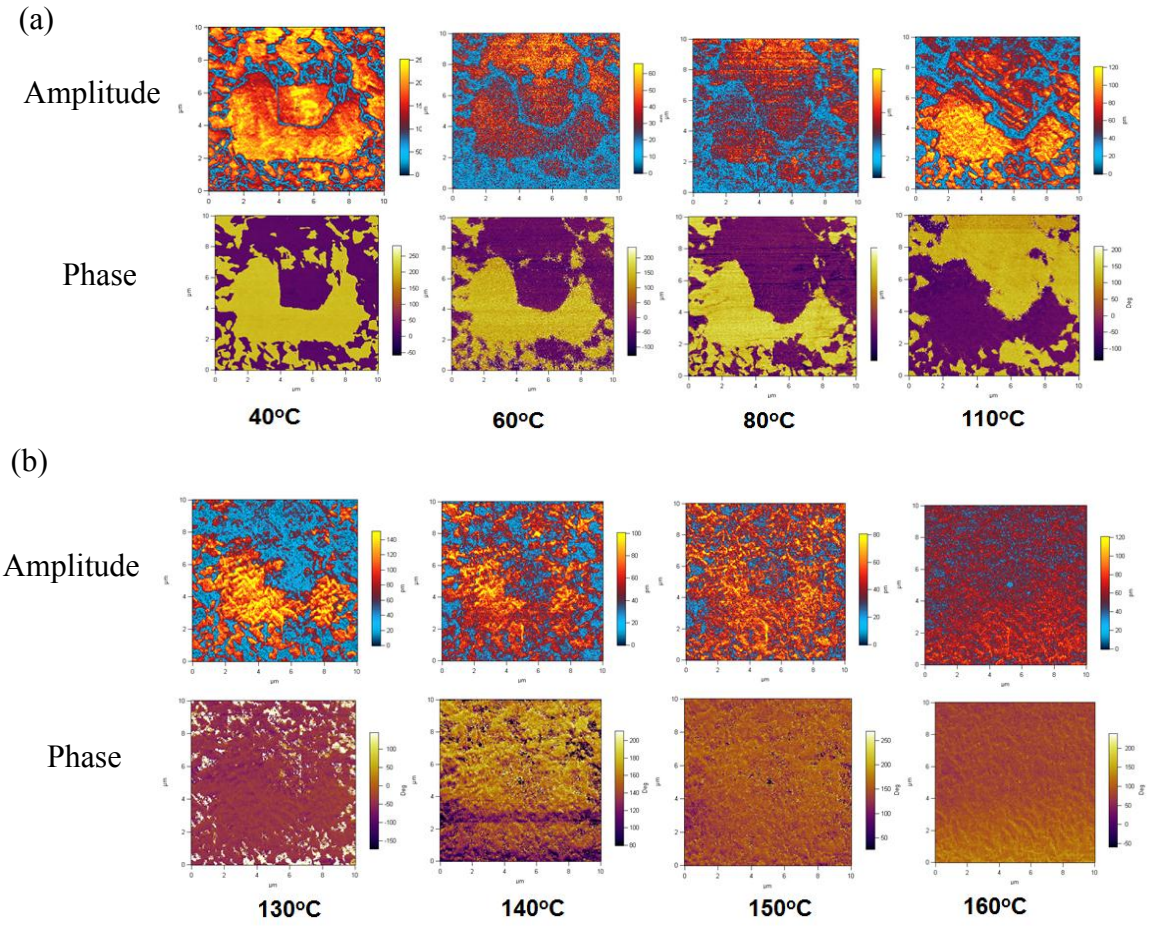

Figure 3.17 (a) PFM amplitude images and phase images of written domains of PMN-PT at 27 °C, 60 °C, 80 °C, 110 °C, 130 °C, 140 °C, 150 °C, 160 °C; the inner positively polarized square has length of 3 μm, while the outer negatively polarized square has length of 8 μm, and the scanning area is 10×10 μm^2.

A ferroelectric domain pattern is first written on a PMN-PT at room temperature, with a positively polarized square of 8×8 μm^2 embedded into a negatively polarized square of 3×3 μm^2, and its piezoresponse is examined in a 10×10 μm^2 area at different temperatures, as shown in Figure 3.16 for both PFM phase and amplitude. At 27^{o}C (RT), the observed PFM phase and amplitude images reflect the original written pattern very well, having a clear interface between the positively polarized square (inner) and negatively polarized square (outer) with phase contrast of around 180^o, indicating their opposite polarities. Large PFM amplitudes as high as 250 pm is observed, indicating its excellent piezoelectricity, and the positively polarized square appear to have slightly higher piezoresponse. Outside the negatively polarized square, the PFM amplitude is similar to the poled area, suggesting that the poling process only switches the PMN-PT domains, rather than enhance its piezoelectricity. With temperatures increasing to 60^{o}C, little change is observed for both the PFM phase and amplitude. Lower amplitude values suggest a decrease in piezoelectricity. When the temperature is increased to 80^{o}C, changes in both PFM phase and amplitude images are observed. In particular, some areas in the poled domain and unpoled area on the top of the square emerged, and PFM amplitude have been sharply reduced, indicating the reduction of the piezoelectricity approaching the rhombohedral-to-tetragonal phase transition temperature. When the temperature was increased to 140^{o}C, contrasts in the PFM phase image largely disappear.

The PFM amplitude also largely vanishes when temperatures approach 160^{o}C suggesting a loss of piezoelectricity around the Curie temperature.

3.3 Conclusion

In this chapter, ferroelectric domain characteristics of $BiFeO_3$ epitaxial thin film and PMN-30%PT single crystal have been studied. In addition, the evolution of the ferroelectric domain structure during increasing temperature in the PMN-30%PT has been probed. Various PFM techniques were employed to investigate the domain configuration and switching of polarization, and this data will support further theoretical and experimental studies on $BiFeO_3$ epitaxial thin film and PMN-PT single crystals.

References

1 N. A. Spaldin and M. Fiebig, Science **309,** 391 (2005).

2 W. Eerenstein, N. D. Mathur, and J. F. Scott, Nature **442,** 759 (2006).

3 T. Zhao, A. Scholl, F. Zavaliche, K. Lee, M. Barry, A. Doran, M. P. Cruz, Y. H. Chu, C. Ederer, N. A. Spaldin, R. R. Das, D. M. Kim, S. H. Baek, C. B. Eom, and R. Ramesh, Nature Materials **5,** 823 (2006).

4 J. Wang, J. B. Neaton, H. Zheng, V. Nagarajan, S. B. Ogale, B. Liu, D. Viehland, V. Vaithyanathan, D. G. Schlom, U. V. Waghmare, N. A. Spaldin, K. M. Rabe, M. Wuttig, and R. Ramesh, Science **299,** 1719 (2003).

5 X. H. Du, U. Belegundu, and K. Uchino, Japanese Journal of Applied Physics Part 1-Regular Papers Short Notes & Review Papers **36,** 5580 (1997).

6 S. Wada, S. Suzuki, T. Noma, T. Suzuki, M. Osada, M. Kakihana, S. E. Park, L. E. Cross, and T. R. Shrout, Japanese Journal of Applied Physics Part 1-Regular Papers Short Notes & Review Papers **38,** 5505 (1999).

7 X. H. Du, J. H. Zheng, U. Belegundu, and K. Uchino, Applied Physics Letters **72,** 2421 (1998).

8 H. X. Fu and R. E. Cohen, Nature **403,** 281 (2000).

9 Y. Lu, D. Y. Jeong, Z. Y. Cheng, Q. M. Zhang, H. S. Luo, Z. W. Yin, and D. Viehland, Applied Physics Letters **78,** 3109 (2001).

10 F. M. Bai, J. F. Li, and D. Viehland, Applied Physics Letters **85,** 2313 (2004).

Chapter 4 Piezoresponse Force Microscopy of Lead Zirconate Titanate Films

Lead zirconate titanate (i.e., PZT) is one of the most widely used ferroelectric materials due to its excellent piezoelectric and ferroelectric properties. Various fabrication techniques have been developed to fabricate thick and patterned PZT films, and recently, stretchable PZT nanoribbons with wavy configurations have been developed. In this chapter, PFM was used to investigate the properties of various synthetic PZT films at the nanoscale.

4.1 PZT Thick Film

PZT ultrasonic transducers with high operating frequencies are desirable to enhance the spatial resolution in imaging applications[1-3]. To achieve such high operating frequency, films of a few micron meters thick are required[4]. Prof. Qifa Zhou's group at USC utilized a composite sol-gel technique to produce high quality PZT films in the micron thickness range, coated on a Pt(111)/Ti/SiO_2/Si(100) substrate. In this section, the local piezoelectric characteristics of these thick PZT films have been studied by PFM.

Vertical PFM was carried out on the PZT thick film to confirm its piezoelectricity. As shown in Figure 4.1, the amplitude and phase mappings of out-of-plane polarization domains were obtained simultaneously. The amplitude image shows a large

piezoresponse of about 700 pm, and the phase image of those high piezoresponse regions suggests that this area is only a single domain. From the image of amplitude mapping overlaid on 3D topography (Figures 4.1 (c)), it is clearly shown that large amplitude values exist inside of the grains. However, the phase mapping overlaid on the 3D topography (Figure 4.2 (d)) shows that the polarization orientation varies from grains to grains.

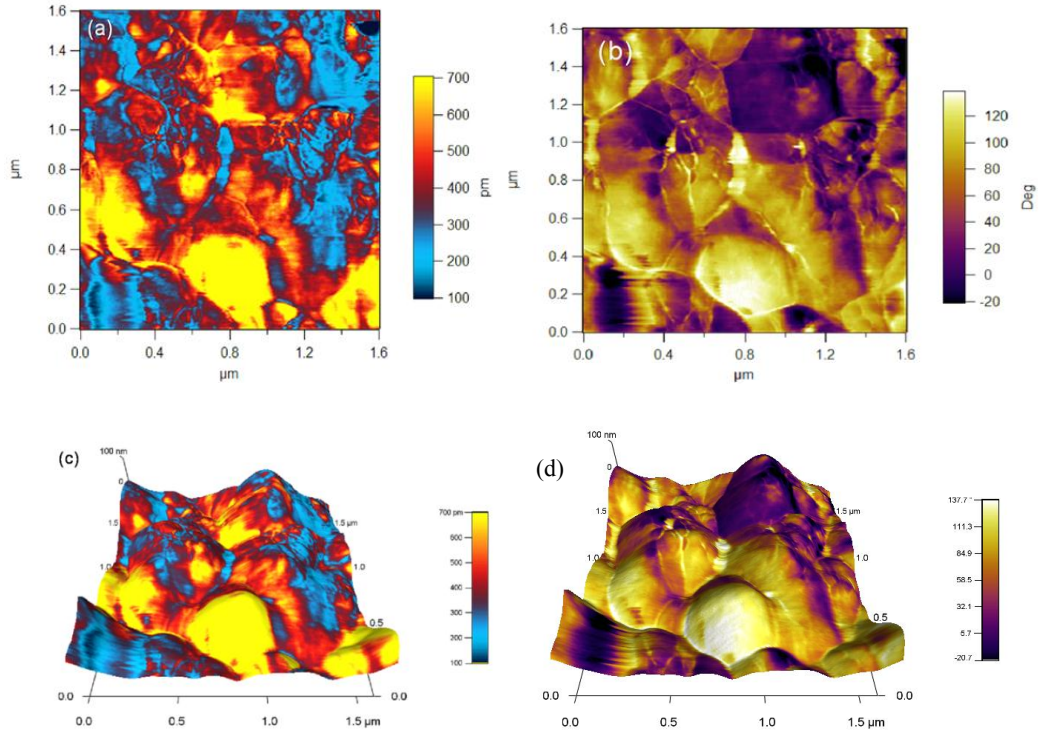

Figure 4.1 Vertical PFM images of 1.6 × 1.6 µm^2 PZT thick film: (a) amplitude, (b) phase, (c) amplitude mapping overlaid on 3D topography image, and (d) phase mapping overlaid on 3D topography image.

Besides the vertical PFM measurement, the in-plane polarization of the films was also characterized by the lateral PFM, which is based on the shear deformation deduced

via a shear piezoelectric coefficient, d_{15}. The lateral PFM images of the PZT thick films are shown in Figure 4.2. It exhibits strong lateral amplitude, as shown in Figure 4.2 (a) and (b), which suggests the predominantly in-plane orientation of the polarization vector. From the PFM amplitude image of the PZT in Figure 4.1 and Figure 4.2, it is observed that the average vertical PFM amplitude is approximately 446 pm under an AC modulation voltage of 10 V, while the average lateral PFM amplitude is found to be approximately 143 pm under an AC modulation voltage of only 3 V. They show that the PZT films exhibit superior piezoelectric properties.

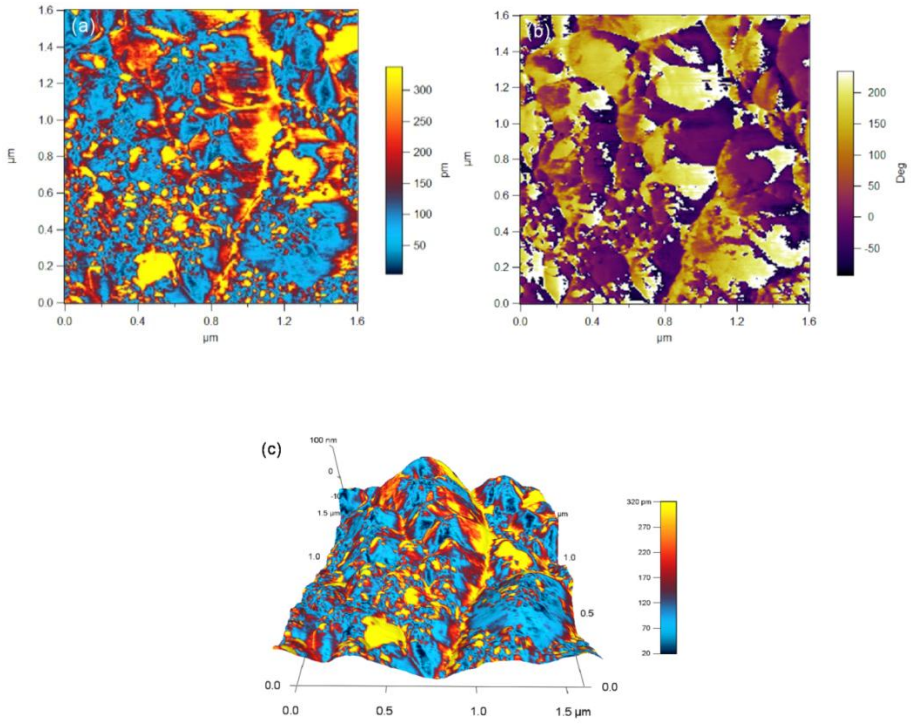

Figure 4.2 Lateral PFM images of 1.6 × 1.6 µm^2 PZT thick film: (a) amplitude, (b) phase, and (c) amplitude mapping overlaid on 3D topography image.

It is also important to switch the polarization of the thick PZT; we carried out switching PFM to obtain the characteristic hysteresis and butterfly loops. As shown in Figure 4.3 (a) and (b), a sequence of DC bias voltage of up to 40 V was applied through the conductive AFM tip to the films, which effectively polarized the films underneath the AFM tip. The resulted piezoresponse was measured using an AC modulation voltage of 2 V. The PFM phase-voltage hysteresis loop and amplitude-voltage butterfly loops were then acquired. The measurements were taken on three different locations of the films, with differences among these three points rather small. Furthermore, the effective piezoelectric coefficient of the thick film was evaluated by $A \bullet \cos(\phi)/V$, as shown in Figure 4.3 (c), where the amplitude, A, and phase, ϕ, are combined into a single term, and V is the amplitude of the AC modulation. A large piezoelectric coefficient of up to 600 pm/V is observed. Since the electric field in the PFM measurement is localized and the piezoresponse was measured near the resonance frequency, this effective piezoelectric coefficient cannot be considered as the intrinsic piezoelectric coefficients of the material. Nevertheless, the results are still impressive and confirmed that the composite sol-gel method can be used to prepare the high-quality PZT thick films.

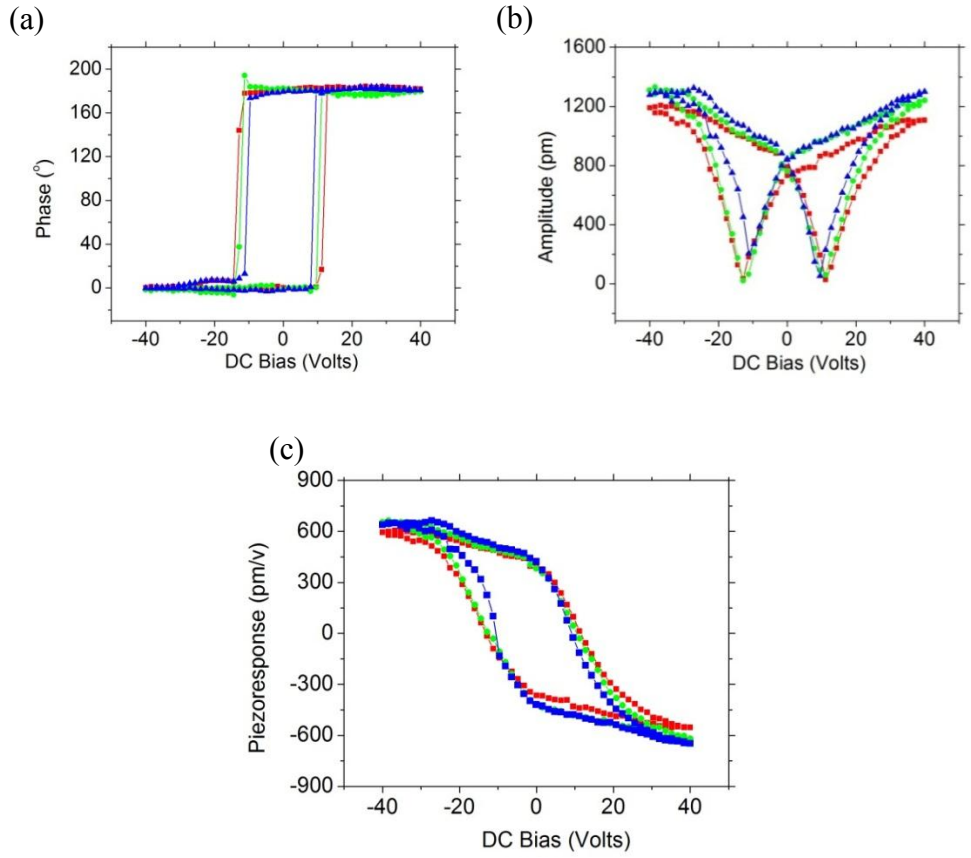

Figure 4.3 (a) Phase-voltage hysteresis loop, (b) amplitude-voltage butterfly loop, and (c) piezoelectric hysteresis loop of the PZT thick film.

We also used the PFM nanolithography to create a ferroelectric domain pattern of characters "USC" on the PZT film, as shown in Figure 4.4 (a). After the PFM lithography, amplitude and phase scans were performed to confirm the patterning of the polar structure. The observed PFM phase image reflects the pre-designed template very well, which indicates that the local polarization of the PZT film can be manipulated by the PFM tip with electric bias, and thus demonstrates good ferroelectricity of the PZT film.

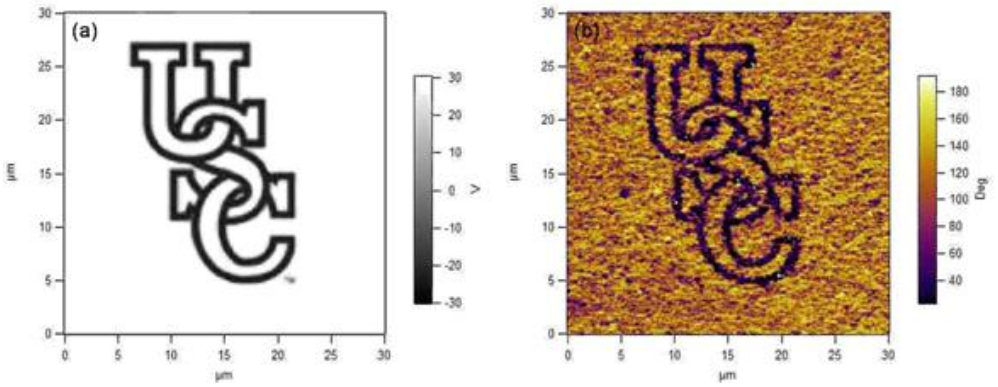

Figure 4.4 (a) A pre-designed pattern of characters 'USC', and (b) PFM phase image of the PZT film after polarized with the pattern.

4.2 PZT Film Patterned by Soft Lithography

With the ever-increasing demand for miniaturization of ferroelectric devices, there have been tremendous efforts in developing micro- and nano-structured ferroelectric patterns with smaller feature size, higher density, and improved sensitivity and functionality[5-9]. Various techniques have been developed to pattern ferroelectric micro- and nano-structures[10-14]. Lining Lan of Xiangtan University in China has employed soft lithography and polydimethylsiloxane (PDMS) to fabricate PZT film into microstructures with the feature size of 2 μm. In this section, PFM has been utilized to verify the good piezoelectricity and excellent ferroelectricity of the PZT microstructures.

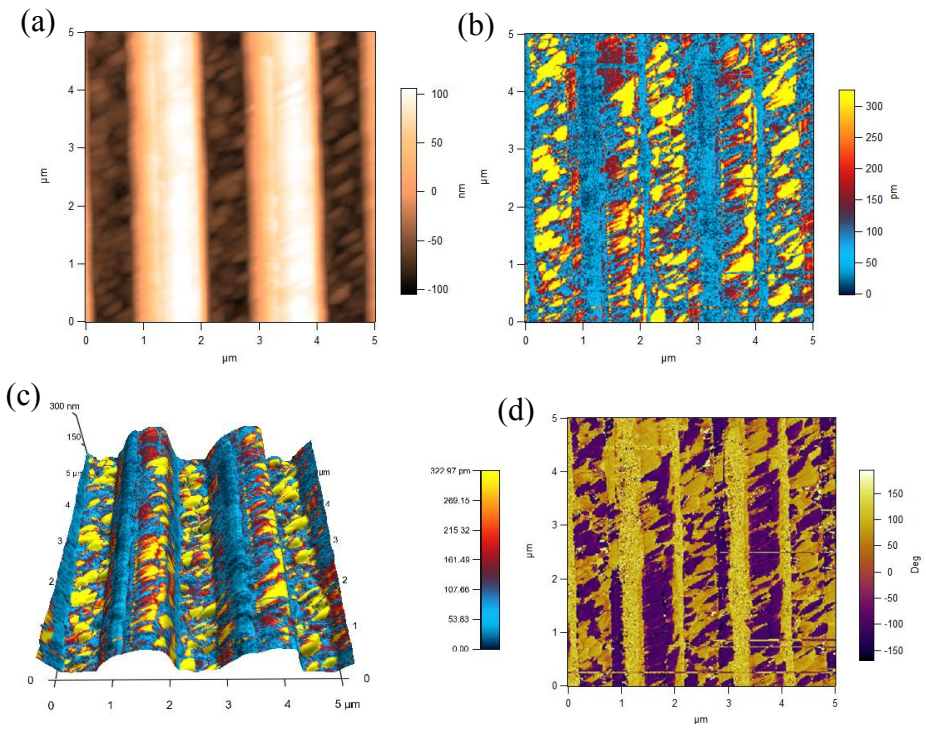

Figure 4.5 The piezoresponse force microscopy (PFM) of the patterned PZT microstructure: (a) Topography, (b) PFM amplitude image, (c) PFM amplitude image imposed on top of the three-dimensional (3D) topography image, and (d) PFM phase image.

PFM amplitude and phase images of the patterned PZT gratings are shown in Figure 4.5, where both conventional 2D and 3D images are shown to better illustrate the correlation between patterned topography and piezoresponse. The topography image (Figure 4.5 (a)) clearly shows the microstructures of patterned PZT after soft lithography. From the PFM amplitude image in Figure 4.5 (b), high PFM amplitude over 320 pm under an AC modulation voltage of 2.2 V was observed on the protruded PZT gratings, confirming the piezoelectricity of the patterned PZT microstructure. This is an excellent piezoresponse for a PZT microstructure without post-poling by an electric field. Away

from the protruded grating, as shown in Figure 4.5 (c), there are small amounts of PZT sol penetrated into the interface between the PDMS and substrate during the soft lithography process. A higher PFM amplitude was also measured in these bottom regions, since they are subjected to the largest pressure, which tends to promote the crystallization of the PZT film, resulting in enhanced ferroelectricity. Furthermore, there is excellent correspondence between the PFM amplitude and phase images both on the protruded and bottom PZT regions. The PFM phase image (Figure 4.5 (d)) displays clearly 180^{o} contrast, suggesting opposite distributions of polarization, and there are obvious boundaries between those domains.

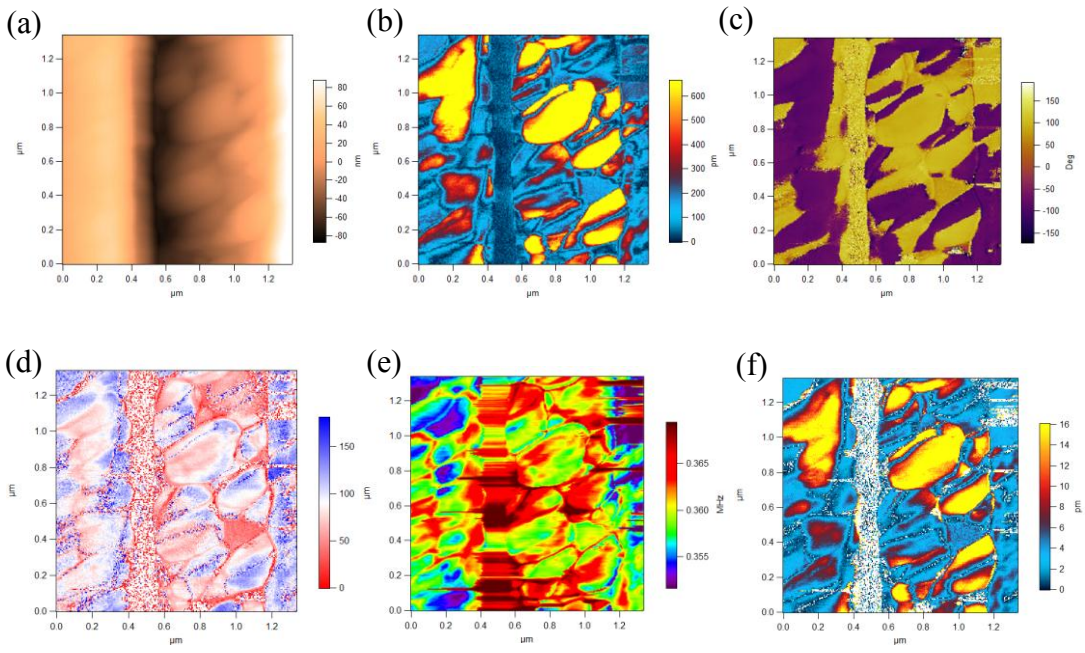

Figure 4.6 PFM of patterned PZT; (a) topography, (b) amplitude, (c) phase, (d) quality factor, (e) resonance frequency, and (f) resonance amplitude corrected by quality factor

To determine the intrinsic piezoelectric coefficient quantitatively, we examined the

piezoresponse of the PZT microstructure using DFRT. As shown in Figure 4.6, PFM mapping over a 1.3 μm × 1.3 μm area covered one period of the PZT pattern. The PFM topography, amplitude, and phase images are shown in Figures 4.6 (a) - (c), respectively. Note that domains with approximately 650 pm amplitude under an AC modulation voltage of 2.2 V formed on both the protruded and the bottom of the PZT pattern. Variations of quality factor and resonance frequency were displayed in the mappings of quality factor and resonance frequency (Figure 4.6 (d) and (e)). The intrinsic piezoresponse of the patterned PZT can then be determined by the mapping of resonance amplitude, corrected by the quality factor (Figure 4.6 (f)), making it possible to evaluate the piezoelectric coefficient, d_{33}, quantitatively. It is observed that the maximum piezoresponse amplitude, after the correction, is 16 pm. These results indicate that the sol-gel based soft lithography technique is able to pattern PZT films with perovskite crystalline structures and good piezoelectric properties.

It is also important to be able to switch the polarization of the patterned PZT microstructures, and this has been verified by switching PFM. A sequence of DC bias voltage of up to 17.6 V was applied through the conductive AFM tip to the protruded PZT grating, which effectively polarized the PZT sample underneath the AFM tip. The resulting piezoresponse was then measured using an AC modulation voltage of 3.3 V. The piezoresponse at the 'OFF' state, which corresponds to the piezoelectricity of the

PZT microstructure at the remnant state after polarization, was presented in Figure 4.7. The hysteresis loop between the PFM phase and DC bias characteristic of ferroelectricity was observed, as shown in Figure 4.7 (a). It confirms the ferroelectricity of the patterned PZT microstructure. For switching data obtained, the maximum bias-induced displacement is measured to be as large as 1.4 nm. It is important to note that the PFM amplitude is related to the piezoelectric coefficient, d_{33}, and magnified by the resonance enhancement. The PFM mapping shows that the quality factor of this patterned PZT film ranges from approximately 50 to 150. As such, the piezoelectric coefficient, d_{33}, of the patterned PZT microstructure is estimated to be between 28 and 42 pm/V, comparable to that of typical PZT films. This excellent piezoelectricity and ferroelectricity confirms that these patterned PZT microstructures are promising for device applications.

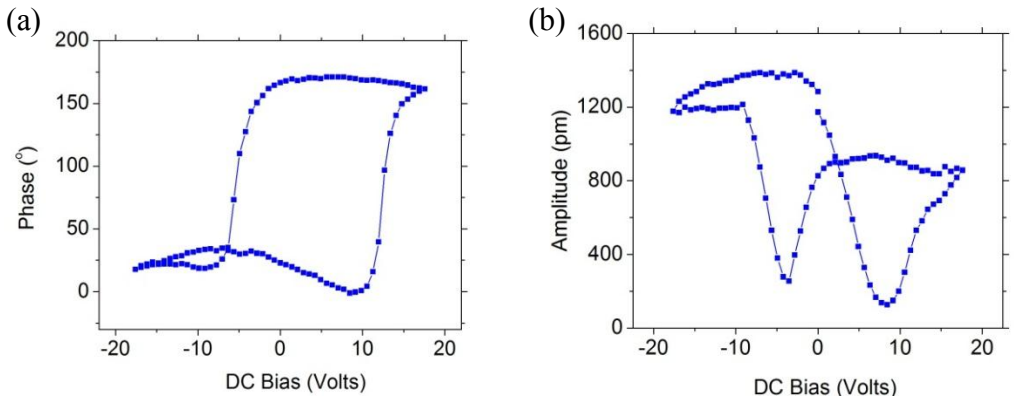

Figure 4.7 'OFF' state switching PFM of patterned PZT microstructure: (a) phase-voltage hysteresis loop, and (b) amplitude-voltage butterfly loop.

4.3 Stretchable PZT Ribbons

PZT films, like most other ceramics, are rather brittle, and they fracture at strain of less than 1%[15]. As a result, typical devices built with PZT can only be subjected to small strain deformations. Prof. Xue Feng of Tsinghua University and John Roger's group at UIUC developed a process for transferring PZT ribbons from host substrates onto flexible rubbers over macroscopic areas. The structures consist of nanoribbons of PZT in "wavy" configurations on soft substrates and are able to bend, stretch, and twist without fracture. In this section, the piezoelectric and ferroelectric properties of PZT ribbons are examined.

Figure 4.8 presents AFM topographical measurements of the nanoribbons immediately after the etching processes, but before the elimination of the SiO_2. The sample consists of Pt/Cr as the top electrode, the active PZT, and Pt/Ti as the bottom electrode coated on a silicon substrate. These AFM results indicate that most areas of PZT ribbons are smooth with a rootmean-square (rms) of 21.9 nm. The widths of the top electrodes and the PZT ribbons are 50 and 80 μm, respectively. It should be noted that variations in thickness across the ribbon are also significant, and the central region is much thicker than the edges, as shown in Figure 4.8 (b).

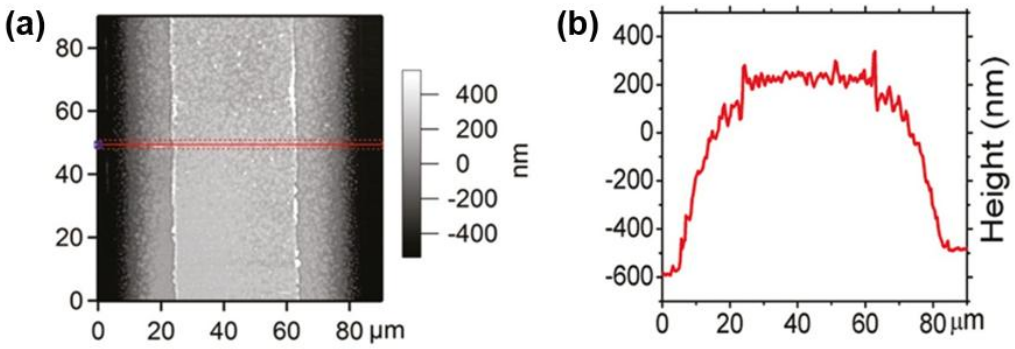

Figure 4.8 (a) AFM image of PZT nanoribbons with electrodes, and (b) height profile along the ribbon cross section; the red line in frame. The approximate position of this profile is indicated (a).

The ferroelectric and piezoelectric properties of these wavy PZT nanoribbons are crucial to their applications. PFM is employed to examine these aspects. The metal pads that connect to the bottom electrodes are grounded. An AC driving voltage of 6.6 V is applied to the specimen through a conductive tip during scanning. DFRT mode with a central frequency of 835 kHz is used to enhance the sensitivity and determine the quality factor, Q, simultaneously. The resulting amplitude and phase maps are overlaid on the AFM topography profiles for a single period of representative wavy structure, as shown in Figure 4.9. Half wavelength and the height of the wavy structure are approximately 53 μm and 1.25 μm, respectively.

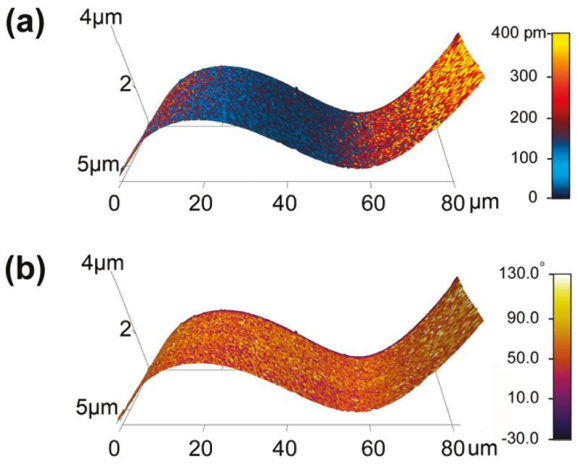

Figure 4.9 PFM measurement of wavy PZT ribbons with electrodes, for AC voltages at frequencies of 835±10kHz. (a) PFM amplitude image overlaid on AFM profile, and (b) PFM phase image overlaid on AFM profile.

As shown in Figure 4.9 (a), the piezoresponse varies along the ribbon, with a maximum response of 400 pm. Piezoresponse of the area near the left wave peak (blue) corresponds to a minimum. Approaching the right wave peak, the piezoresponse increases gradually and finally reaches a maximum. These variations correlate to local deformations associated with the wavy morphology. Moreover, strain varies both along the ribbon thickness (e.g., top surface on the crest in tension, and bottom surface on crest in compression due to bending) and length (e.g., top surface of crests and troughs in tension and compression, respectively) directions. As a result, piezoelectric effects induced by both the local strain and the strain gradient contribute to variations in the piezoresponse.

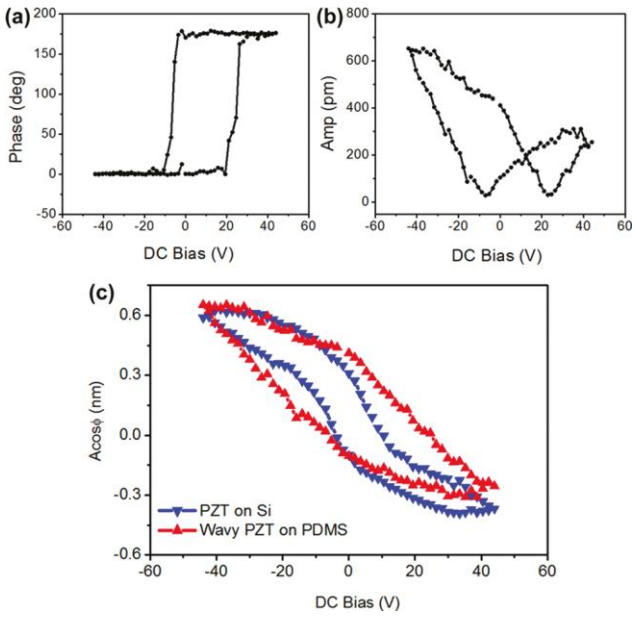

Figure 4.10 (a) PFM hysteresis phase loop, (b) PFM butterfly loop, and (c) PFM hysteresis loops of a wavy PZT ribbon on PDMS and a PZT film on Si, respectively.

To investigate the ferroelectricity of the PZT nanoribbons, a sequence of DC biases were imposed on top of the AC driving voltage, with the piezoresponse measured simultaneously. The phase-voltage hysteresis loop exhibits a well-defined, symmetric hysteresis loop, as in Figure 4.10 (a). The amplitude response presents an expected butterfly curve, shown in Figure 4.10 (b). Both phase and amplitude results are consistent with bulk PZT materials, thereby suggesting good ferroelectric properties of the wavy PZT nanoribbon. Comparison of the effective piezoelectric coefficient, d_{33}, before and after the transfer printing can be performed by the measured hysteresis and butterfly loops of the switching PFM for these two cases, as shown in Figure 4.10 (c). The hysteresis loops are symmetric with respect to the applied voltage, and the piezoresponse

of the wavy PZT nanoribbon on the PDMS is comparable to that of a corresponding flat film on the silicon substrate in magnitude, with a slightly bigger coercive field.

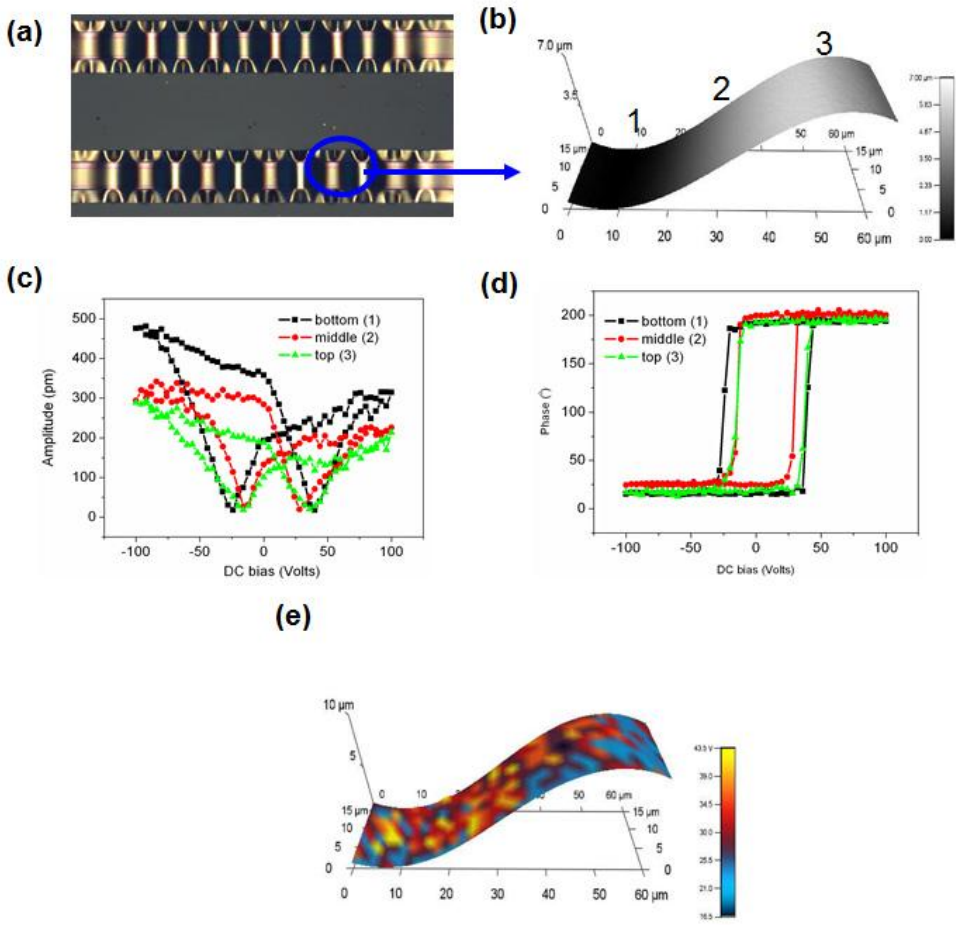

Figure 4.11 Wavy PZT nanoribbon on PDMS. (a) Optical image of a pair of wavy PZT nanoribbons on PDMS. (b) Three-dimensional AFM topography image of half wavelength PZT nanoribbon. (c) amplitude-voltage butterfly loop. (d) phase-voltage hysteresis loop measured at three typical locations. (e) SSPFM mapping of coercive voltage over the half wavelength PZT nanoribbon.

Wavy PZT samples without the top electrode were also fabricated to investigate the variations of ferroelectricity throughout the nanoribbons, which correlate to local deformations associated with the wavy morphology. A representative wavy structure is

shown in Figure 4.11 (a). No fracture or cracking of any part of the structure is noticed. From the three-dimensional AFM topography image, the half wavelength and the amplitude of the wavy structure are approximately 55 μm and 4.9 μm, respectively, which results from a lager prestrain of PDMS during transfer. As shown in Figure 4.11 (c) and (d), three representative butterfly and hysteresis loops were measured at the bottom, middle and top regions of the nanoribbon. Observed from hysteresis loops, the phase contrast is approximately 180^{o}, a clear indication of polarization switching when the coercive voltage is exceeded. The amplitude-voltage butterfly loops show that strain saturates at a relatively high voltage, suggesting that the response is piezoelectric. The maximum piezoresponse of butterfly loops increases gradually from the bottom of the sinusoidal-shape ribbon to the top, consistent with the PFM mapping results. In addition, detailed SSPFM mapping of the coercive voltage was obtained, as shown in Figure 4.11 (e), indicating that the average of the coercive field is approximately 22 V in the middle, 28 V on the top, and 33 V at the bottom area, suggesting areas in compression requires a larger external bias on domain switching.

PFM lithography is employed to confirm the good ferroelectricity and stability of the polarization and demonstrate that the wavy PZT can be used for flexible nonvolatile memory. In this process, the tip voltage is used to write a domain pattern with the distribution of positive and negative polarizations on the trough of a wavy nanoribbon,

forming a designed pattern of “Flex Ferro”. Such a pattern can then be read from the PFM phase image right after PFM lithography, as exhibited in Figure 4.12 (a), clearly showing phase contrasts. The phase image is also imposed on 3D topography to present the pattern location. It is noted that the writing process does not change the 3D topography. In order to confirm the stability of the written polarization, PFM was carried out again over the same area after a period of time. As shown in Figure 4.12 (b), PFM mapping after 24 hours reveals a clear domain configuration as the initial pattern, suggesting that no depolarization occurs after the PFM lithography, and confirms that the written domains remain stable at room temperature for a long time. To further investigate the polarization switching of the wavy nanoribbons, a new trough area was selected to write a same pattern using PFM lithography, and the entire region was imaged, shown in Figure 4.12 (c). It is also interesting that these written patterns can be rewritten by applying a different distribution of positive or negative voltage during scanning. Domains written using a different designed pattern of “FeRAM” over the same area produced another configuration, as shown in Figure 4.12 (d). Arbitrary polarization patterns could be repeatedly written and erased with a high resolution, showing that these wavy PZT are suitable for use in high-density nonvolatile memories and ferroelectric devices. Overall, the results confirm that the processing of this wavy PZT fabrication does not degrade ferroelectric and piezoelectric properties.

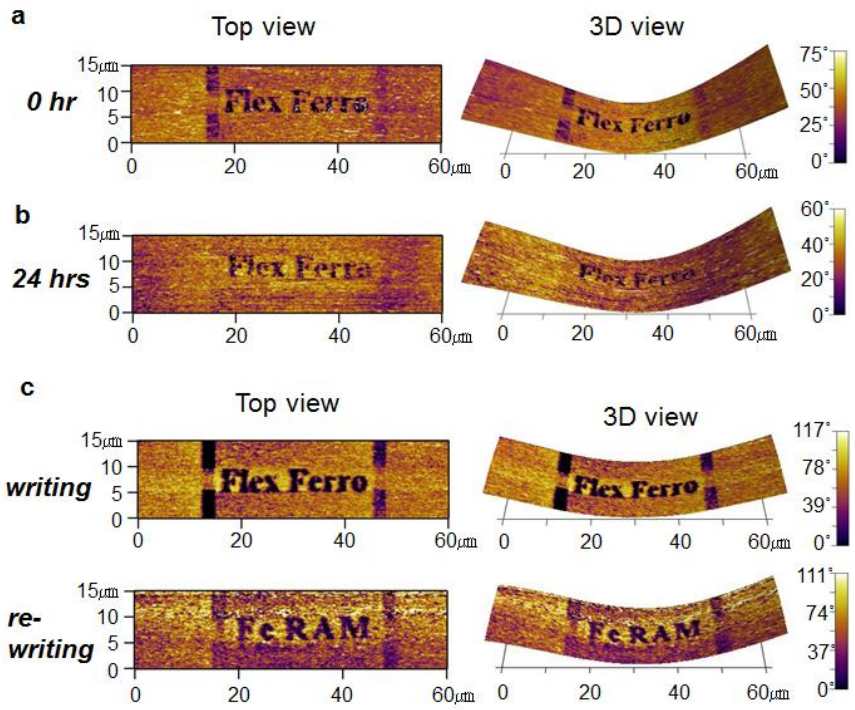

Figure 4.12 2D and 3D phase images of wavy PZT with patterns written by conductive AFM tips and read by PFM: (a) 0 hour, (b) 24 hours after PFM lithography, and (c) same domain pattern written on another PZT nanoribbon.

A key function of the wavy ribbons is to provide linear elastic responses to the applied strain. They provide true stretchability for strain in various in-plane directions. Piezoelectric effects, as well as ferroelectricity of the wavy PZT, should not be affected by the variations of both the local strain and the strain gradient. Hence, it is also very important to investigate if ferroelectric and piezoelectric properties degrade during elastic deformation. To study the ferroelectricity of wavy PZT nanoribbons under various strain, we performed uniaxial tensile stretching and compression along ribbon wavelength directions, as well as torsion tests using a calibrated mechanical stage. In this study, we

first write a domain pattern of “Flex Ferro” on the trough of a wavy nanoribbon using PFM lithography without inducing strain, as discussed above. Such a pattern was read from the PFM phase images. Then, compressive strain was applied along the wavelength direction of the wavy PZT, as schematically shown in Figure 4.13 (a). By calculating the cross section from the measured PFM topography images, strain for a single period of PZT ribbon was determined, as shown in Figure 4.13 (b). PFM is carried out while various strain remains. The resulting phase images of all strain states are imposed in 3D, as shown in Figure 4.13 (c). The wavelength decreases with compressive strain and recovers to its initial value upon release. Under large compressive strain, the observed PFM phase images reflect the original written pattern very well, having a clear interface between the positively polarized letter and the negatively polarized area. No change of domain pattern is observed for the PFM phase, indicating that the good ferroelectricity of wavy PZT remains.

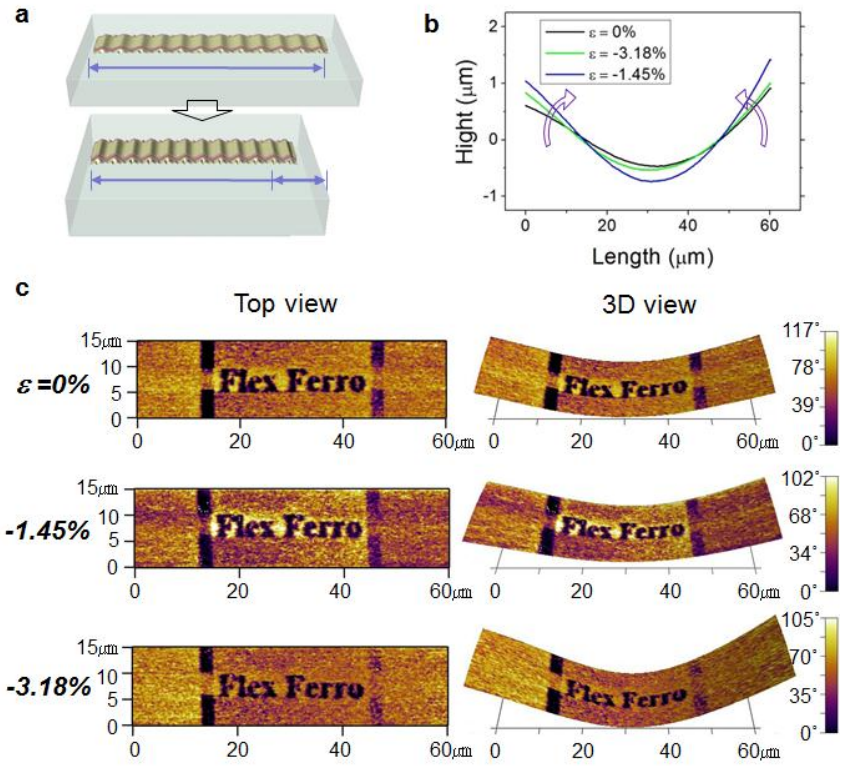

Figure 4.13 (a) Schematic illustration of wavy PZT nanoribbons under compressive uniaxial strain, (b) cross sections, and (c) PFM phase images of wavy PZT nanoribbons under various strain.

In addition, tensile strain was also applied, as schematically shown in Figure 4.14 (a). Tensile stain applied along the direction of the long waves caused the structure to "unfold", gradually resulting in the wavy geometry to a fully stretched state as shown in Figure 4.14(b). Similar to compressive case, the observed PFM phase images reflect the original written pattern very well, having a clear interface of domain structure. Little change is observed for the PFM phase contrast of opposite domain polarization from the PFM phase, indicating a little depolarization occurs under the repeated compressing and

stretching cycle test. In particular, for applied strain comparable to the prestrain (8.21%), the ribbon becomes flat and good domain configuration remains. The structure returns to its original wavy shape, with little change after release of the applied strain.

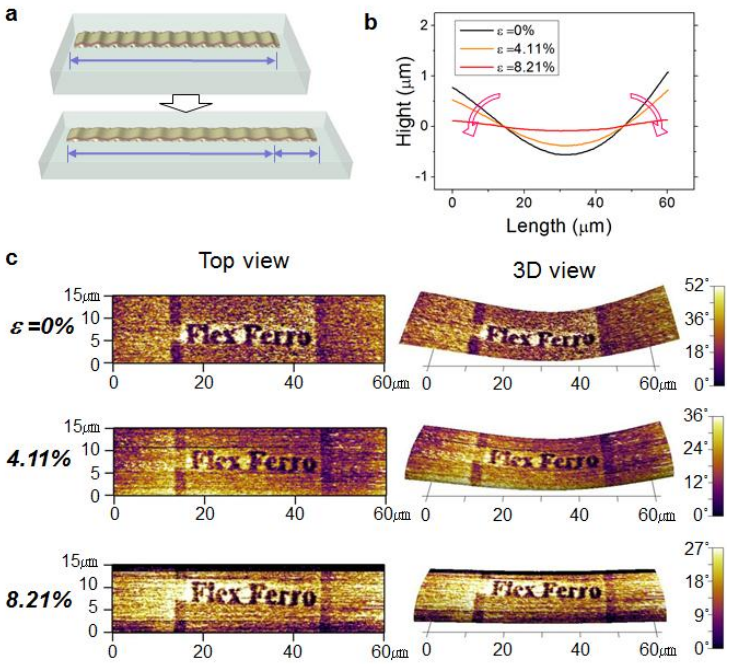

Figure 4.14 (a) Schematic illustration of wavy PZT nanoribbons under tensile uniaxial strain; (b) cross sections and (c) PFM phase images of wavy PZT nanoribbons under various strain.

For the third case, a 20^{o} twisted deformation was induced to the whole sample, as shown in Figure 4.15 (a) and a smaller PFM scan shows that very good domain patterns remained under this state, as seen in Figure 4.15 (b), confirming the ferroelectricity is robust under mechanical deformation, including compression, stretching, and twisting,

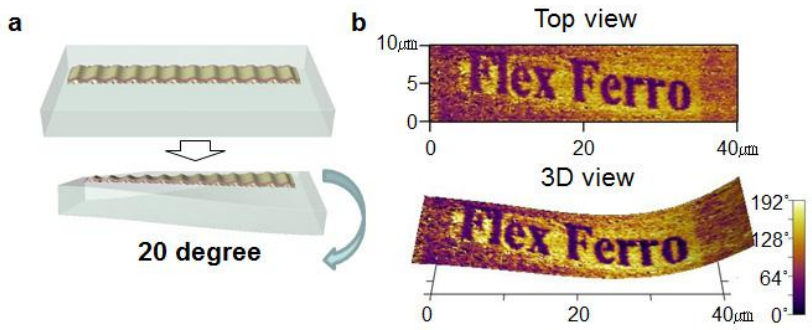

Figure 4.15 (a) Schematic illustration of wavy PZT nanoribbons under twist deformation, and (b) PFM phase images of wavy PZT nanoribbons.

In summary, PFM was adopted to characterize the performance of the piezo-ribbons, coupled with stretchable PDMS. It is observed that the wavy PZT nanoribbons exhibit ferroelectricity and piezoelectricity comparable to flat PZT films on rigid silicon substrates. PFM characterizations under different deformation are also carried out, confirming that its good piezoelectricity and ferroelectricity are not negatively affected by mechanical stretching, compression, and twisting.

Reference

1 R. H. Silverman, D. E. Kruse, D. J. Coleman, and K. W. Ferrara, Investigative Ophthalmology & Visual Science **40,** 1373 (1999).

2 D. Rallan and C. C. Harland, Clinical and Experimental Dermatology **28,** 632 (2003).

3 J. Lee, C. Lee, H. H. Kim, A. Jakob, R. Lemor, S. Y. Teh, A. Lee, and K. K. Shung, Biotechnology and Bioengineering **108,** 1643 (2011).

4 Q. Zhou, S. Lau, D. Wu, and K. Kirk Shung, Progress in Materials Science **56,** 139 (2011).

5 C. R. Martin; and I. A. Aksay, Journal of Electroceramics **12,** 53 (2004).

6 M. Alexe, C. Harnagea, A. Visinoiu, A. Pignolet, D. Hesse, and U. Go¨sele, Scripta Materialia **44,** 1175 (2001).

7 S. Clemens, S. Röhrig, A. Rüdiger, T. Schneller, and R. Waser, Nanotechnology **20,** 075305 (2009).

8 A. Gruverman and A. Kholkin, Reports on Progress in Physics **69,** 2443 (2006).

9 D. Li and D. A. Bonnell, Ceramics International **34,** 157 (2008).

10 M. Alexe, C. Harnagea, W. Erfurth, D. Hesse, and U. Gösele, Applied Physics A **70,** 247 (2000).

11 V. Nagarajan, A. Stanishevsky, and R. Ramesh, Nanotechnology **17,** 338 (2006).

12 S. Bühlmann, P. Muralt, and S. Von Allmen, Applied Physics Letters **84,** 2614 (2004).

13 L. Zhang, S. Ducharme, and J. Li, Applied Physics Letters **91,** 172906 (2007).

14 C. R. Martin and I. A. Aksay, J. Phys. Chem. B **107,** 4261 (2003).

15 T. Tanimoto, K. Okazaki, and K. Yamamoto, Jpn. J. Appl. Phys. **32,** 4233 (1993).

Chapter 5 Piezoresponse Force Microscopy and Nanoimprint Lithography of Ferroelectric Nanostructures

In this chapter, we describe the preparation of P(VDF-TrFE 65:35) copolymer thin film using spin coating, and a nanoimprinting lithography technique for patterning polymeric nanostructures. We develop a rapid nanoimprinting process using air cushion press to pattern a large area of polycrystalline ferroelectric P(VDF-TrFE) copolymers into regular arrays. Optimal imprinting conditions for efficient and excellent pattern transfer between the imprinting mold and imprinted polymer film was identified. To characterize the P(VDF-TrFE) thin films before and after nanoimprinting, x-ray diffraction (XRD), atom force microscopy (AFM), scanning electron microscopy (SEM), and ferroelectric hysteresis measurement were carried out. The results establishes good crystalline structure and excellent ferroelectricity of nanoimprinted P(VDF-TrFE) nanostructures.

5.1 P(VDF-TrFE) Thin Films

5.1.1 P(VDF-TrFE) Thin Films by Spin Coating

P(VDF-TrFE) copolymers with a molar ratio of 65:35 were obtain from Solvay Solexis Inc., and dissolved in Methyl Ethyl Ketone (MEK) purchased from Mallinckrodt Baker Inc. at room temperature, and were mix thoroughly for 1 hour. The weight concentration of the P(VDF-TrFE) were controlled to be 5%. The solution was spin

coated onto bare silicon substrate and the silicon substrate with gold electrode respectively. The spin-coater was set up in a clean fume-hood. The gold electrode was chosen because of its excellent conductivity and good adhesion with P(VDF-TrFE). Chromium with 10nm thickness was evaporated onto silicon wafer first, followed by evaporation of 100nm thick gold. Evaporation of the electrode was carried out using magnetron sputtering system at pressure around $3x10^{-5}$ torr. The thickness of electrode was controlled by sputter time and the deposition rate of electrode was set to be 0.5A/s.

Thermal annealing is often necessary to enhance the crystallinity of polymer materials. The P(VDF-TrFE) films were usually annealed at a temperature slightly higher than Curie temperature, when the molecular chains of P(VDF-TrFE) undergo local reorganization in their paraelectric phase. All the samples after spin coating were cured at 80^{o}C for 30 minutes to remove the residual solvent, and then annealed at 120^{o}C for 12 hours using an oven, unless otherwise noted.

5.1.2 Film Thickness

The film samples after curing were cut using blazer knife and the cross-sectional image of films were measured by Stylus profilometer to evaluate the thickness of thin films. The film thickness can be controlled in the range of 60 nm to 2000 nm by changing the concentration of P(VDF-TrFE) in the solution as well as the spin speed. The

concentration of P(VDF-TrFE) in MEK was set to be 0.5%, 1.0%, 2.0%, 3.0%, 4.0%, 5.0% and 10.0% by mass fraction for film on silicon substrate. The dependence of film thickness on the spin speed and P(VDF-TrFE) concentration are shown in Figure 5.1. It is observed that for the film spin coated by 1% P(VDF-TrFE) concentration, the film thickness does not vary with spin speed much when it is over 1000 revolution per minute (rmp); for films spin coated by 2% concentration, the film thickness is stabilized when the spin speed goes over 2000 rpm, as show in Figure 5.1 (a). We choose spin speed of 3000 rpm for 60 seconds in our experiments.

Film thickness also depends on the concentration of solution. Typical P(VDF-TrFE) film thicknesses as a function of solution concentration at spin speed of 3000 rpm are show in Figure 5.1 (b), with MEK as the solvent. The films thickness increases with the increase of solution concentration, and the thickness were found highly non-uniform when the solution concentration is lower than 0.5% or higher than 10%. The film thickness is around 75 nm for 0.5% solution. Multilayer films can be constructed to prepare thicker films in the micron meter range using 10% P(VDF-TrFE) solution with repeated spin coating.

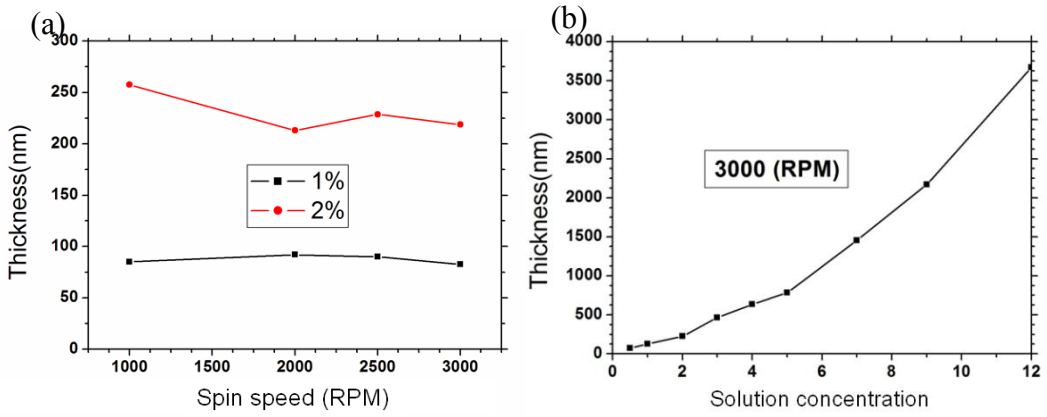

Figure 5.1 The relationship of P(VDF-TrFE) film thickness with spin speed and solution concentration; MEK was used as solvent.

5.1.3 Crystallinity

X-ray diffraction (XRD) was utilized to characterize the crystalline structure of P(VDF-TrFE) thin films with thicknesses of 225 nm and 778 nm on bare Si wafer or gold coated Si substrate. Typical diffraction peaks due to reflections from (110) plane of the β phase are observed at 2θ=20.09, as shown in Figure 5.2, and it evident that thicker film shows better crystallinity.

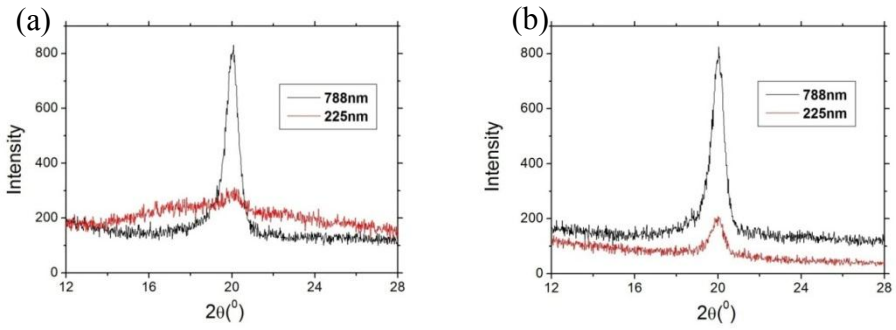

Figure 5.2 X-ray diffraction patterns for thin films with thickness of 225nm and 788nm on silicon substrate (a) and gold coated Si substrate (b).

5.1.4 Ferroelectricity of P(VDF-TrFE)

The ferroelectric hysteresis loops were measured on annealed P(VDF-TrFE) films using Radiant Precision LC ferroelectric tester over a macroscopic area. The Sawyer-Tower circuit method was used as schematically shown in Figure 5.3. As with the impedance analyzer, an AC voltage is used to charge and discharge the sample, and there is a capacitor in series with the sample. The voltage across both the sample (V_S) and the capacitor (V_C) are measured. Since the capacitance of the capacitor is known the charge on the capacitor can be calculated, which by conservation of charge, is the same as the charge on the sample. The polarization can then be calculated using Q/A, where Q is the charge on the sample surface, and A is the sample area. As a result, the polarization versus voltage hysteresis loop can be obtained.

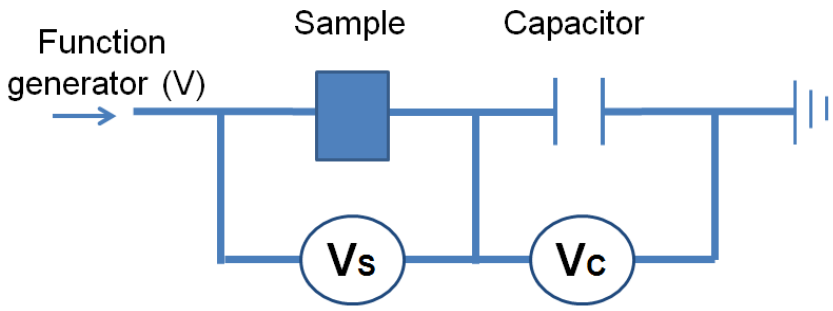

Figure 5.3 The schematics of Sawyer-Tower circuit for polarization hysteresis measurement.

In our experiment, P(VDF-TrFE) copolymer with 788nm thickness film was spin coated on gold coated Si substrate, as described before. Then silver paint was coated on

the film surface as the top electrode, with a copper wire sticking on it. The top electrode coated area is around 1cm^2. The polarization versus the applied electric field is shown Figure 5.4.

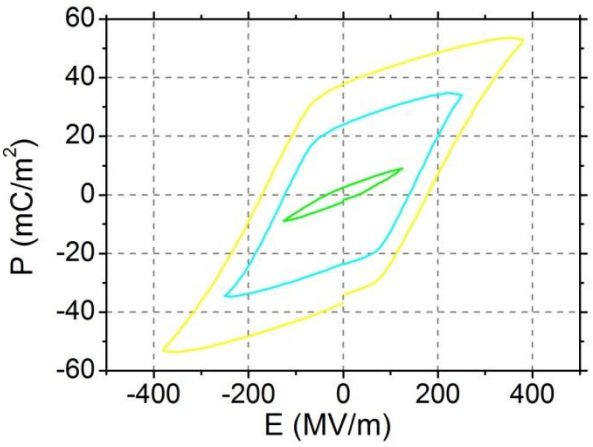

Figure 5.4 Hysteresis loop of P(VDF-TrFE) film obtained with different biases ranging from -190 MV/m to 190 MV/m, -220 MV/m to 220 MV/m, and -390 MV/m to 390 MV/m.

Three loops under different maximum biases were obtained, as shown in Figure 5.4, with the voltage for first (green) loop ranging from -110 MV/m to 110 MV/m, the second (blue) from -220 MV/m to 220 MV/m, and the third (yellow) from -390 MV/m to 390 MV/m. The first curve shows evidence of hysteresis, but not switching behavior. The second and third curves show evidence of switching with coercive field at 90 MV/m. Since no clear evidence of saturation could be observed at 390 MV/m, the remnant polarization of (PVDF-TrFE) can only be estimated to be 40 mC/m^2.

5.2 Thermal Stability

A critical issue is the thermal stability of P(VDF-TrFE) copolymers film, which include two aspects: (1) Thermal effect on local morphology of ultra-thin film; and (2) How does its local microscopic ferroelectric properties vary with temperature. Note that the ferroelectric properties should be investigated and understood, not only qualitatively, but also quantitatively, to enable reliable practical applications in a realistic device setting. In this section, we will investigate the thermal effects of P(VDF-TrFE) ultra-thin film morphology and P(VDF-TrFE) thin film domain structure using AFM and PFM.

5.2.1 Thermal Effect on Local Morphology of Manomesa

There has been very interesting nanoscale structure found by Bai *et al.*[1,2] during his investigation of annealing effect on thinner P(VDF-TrFE) films with thickness less than 10 nm. These structures are referred to as 'nanomesas', which are self-organized structures formed after annealing of P(VDF-TrFE) copolymer. In this section, observation of nanomesas formation is presented, and the P(VDF-TrFE) ultra-thin film sample was provided by Stephen Ducharme's group at University of Nebraska in Lincoln (UNL).

Here we directly observe how the film as deposited forms nanomesas during annealing using AFM in combination with PolyHeater. We have observed nanomesa formation during annealing on the stage of AFM by taking images at about every 20ºC

steps. The sample was mounted on the top of the scanner with steel clamp. To reduce calibration errors between heater stage and P(VDF-TrFE) thin film surface, the temperature of the film was measured directly using Fluke 52 K/J Thermalmeter thermocouple.

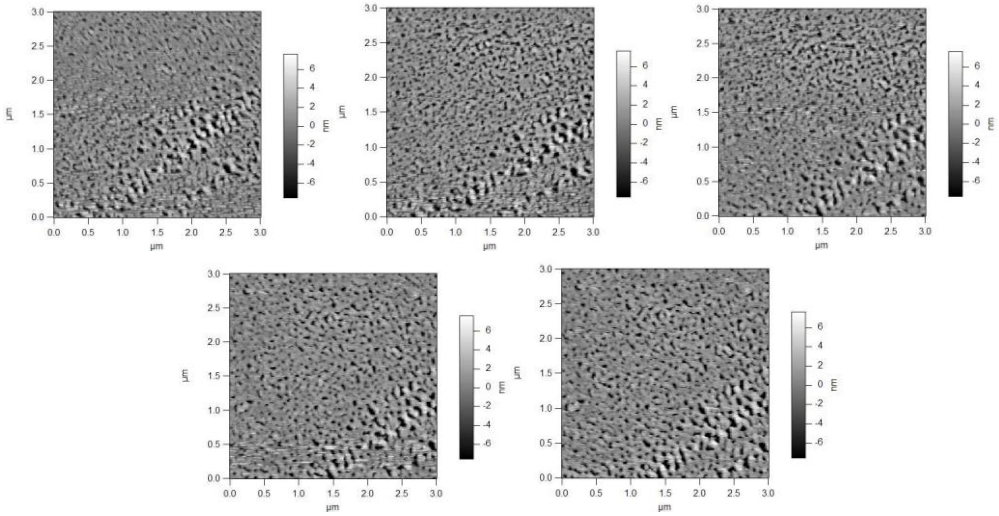

Figure 5.5 AFM images of P(VDF-TrFE) copolymer film taken during annealing at the temperature of 100^{o}C.

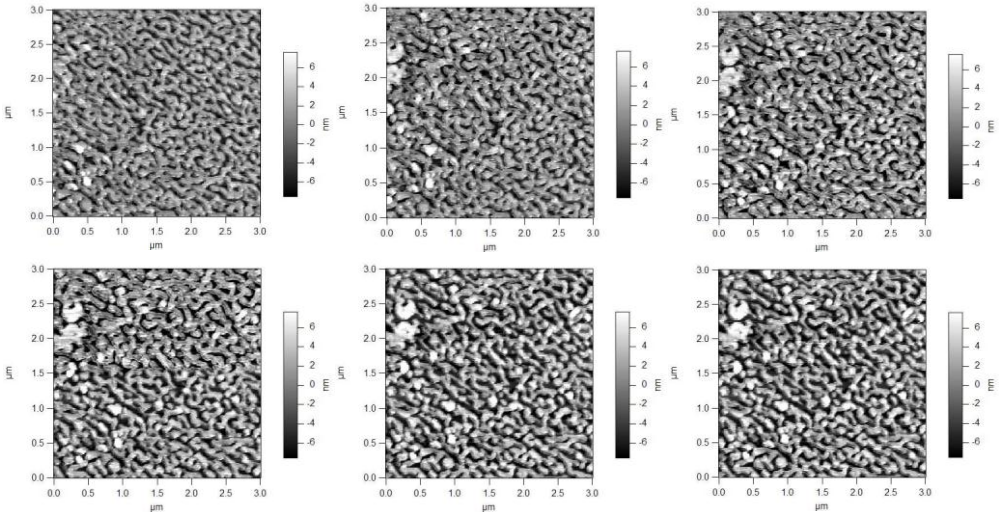

Figure 5.6 AFM images of P(VDF-TrFE) copolymer film taken during annealing at the temperature of 120^{o}C.

The temperature was increased at 10~20 ºC steps with a rate of 5 ºC/min, and then was hold at the given temperature for 5 minutes before scanning. serious series of images were recorded at each temperature stage.

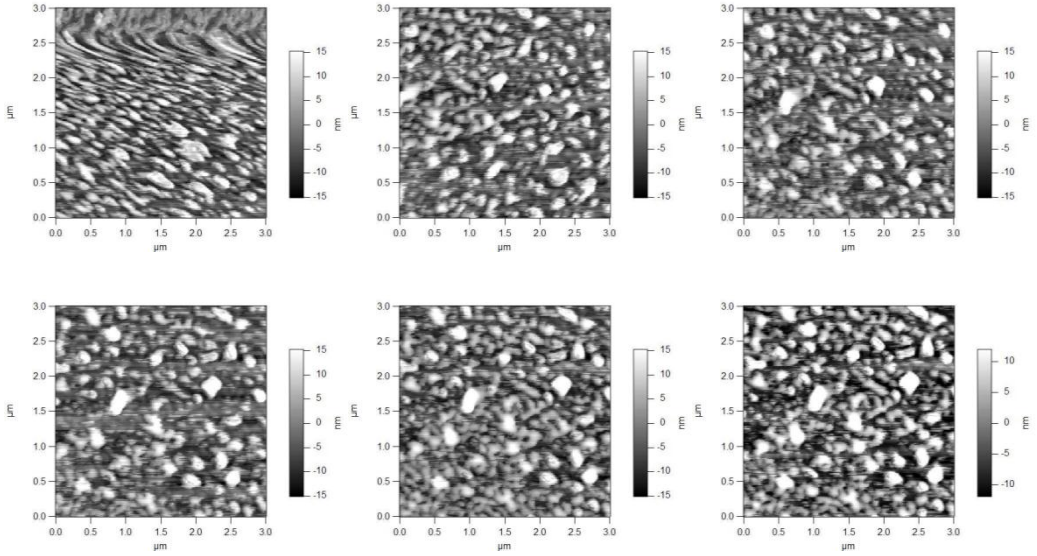

Figure 5.7 AFM images of P(VDF-TrFE) copolymer film taken during annealing at the temperature of 140^{o}C.

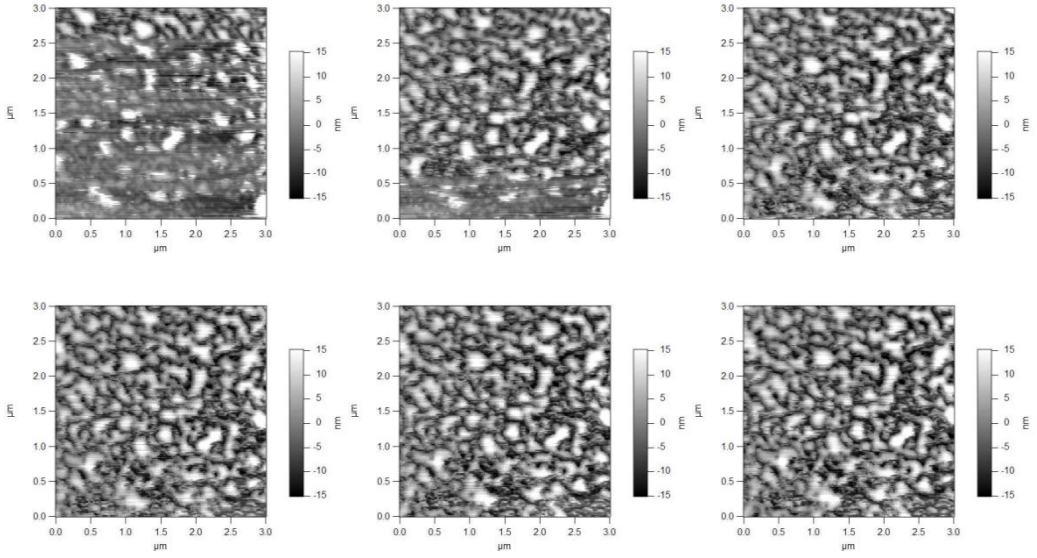

Figure 5.8 AFM images of P(VDF-TrFE) copolymer film taken during annealing at the temperature of 160^{o}C.

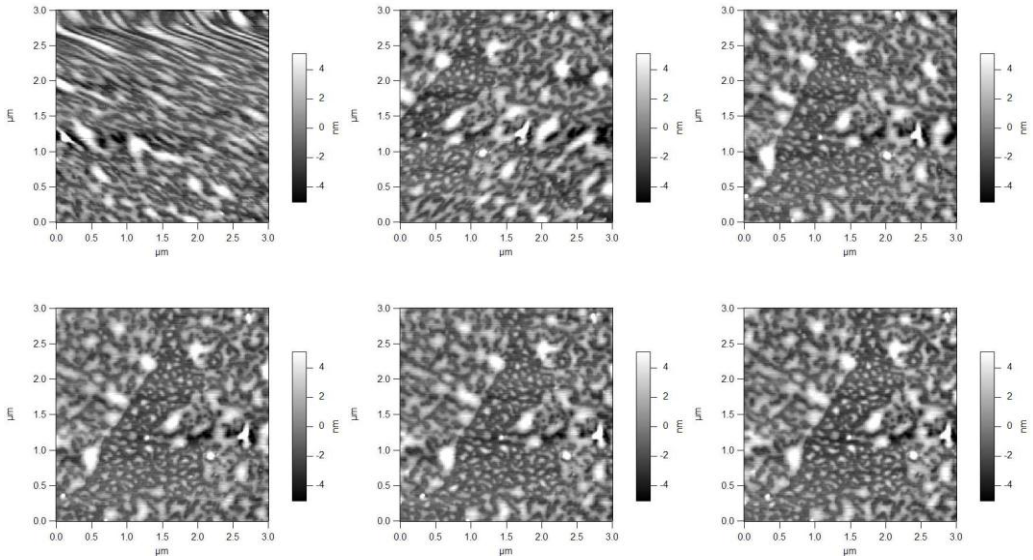

Figure 5.9 AFM images of P(VDF-TrFE) copolymer film taken during annealing at the temperature of 180^{o}C.

The set of images shown in Figure 5.5 are continuous 5 scans at temperature of 100^{o}C, showing the real-time observation of nanomesas formation. Continuous images were scanned after the temperature reaches the target point to investigate the morphology evolution. It is observed that some holes around 10nm to 100nm start to appear at 100^{o}C.

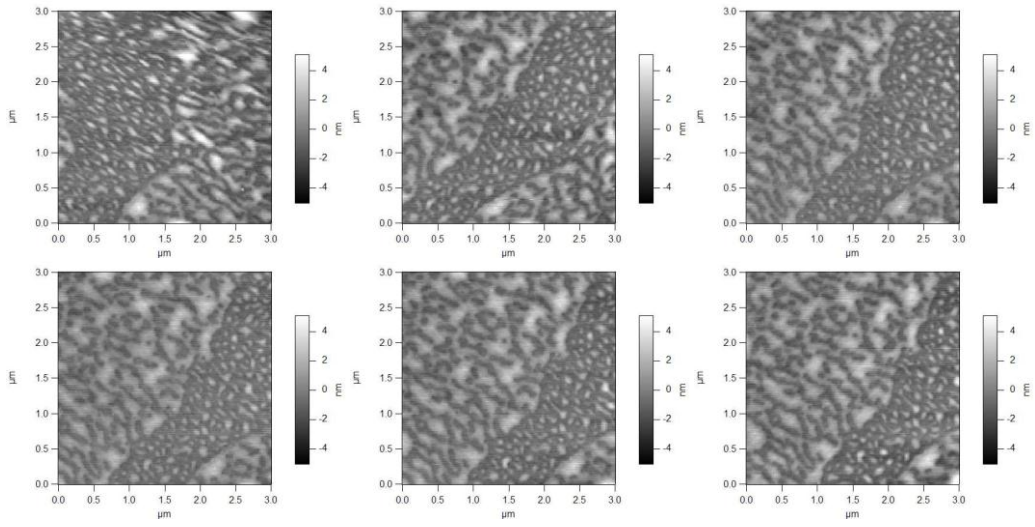

Figure 5.10 AFM images of P(VDF-TrFE) copolymer film taken during annealing at the temperature of 200^{o}C.

In Figure 5.6 to Figure 5.10, the temperature was increased and hold at the level of 120^{o}C, 140^{o}C, 160^{o}C, 180^{o}C and 200^{o}C respectively. Continuous scanning of 6 images was recorded at each temperature stage. All images represent film areas of 3 μm^2. As these images revealed, the pattern formation is not reversible process because the amount of separation occurred during annealing, which is preserved after the annealing. The pattern started to form at 100 ºC and these features started to be separated at 120ºC (Figure 5.6). These are the early form of nanomesas. The nanomesas were fully formed at 140ºC (Figure 5.7). The size and height of nanomesas increase substantially when the temperature reached 160ºC (Figure 5.8) and decrease sharply at 180ºC (Figure 5.9). Continuous scans confirm that the patterns still exist at 200 ºC (Figure 5.10).

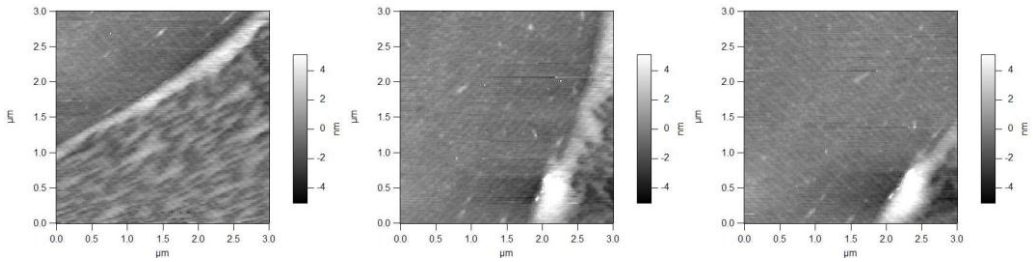

Figure 5.11 AFM images of P(VDF-TrFE) copolymer film taken during annealing at the temperature of 220^{o}C.

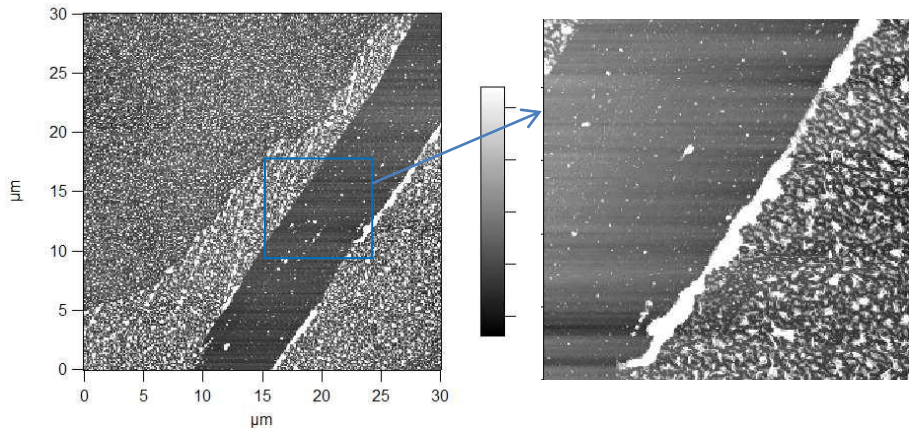

Figure 5.12 AFM images of P(VDF-TrFE) copolymer at 30 μm^2 area (left) and zoom in image (right) taken after the temperature get back to room temperature again.

Finally, the nanomesas disappeared when temperature reached 220 ºC (Figure 5.11). The topography images of P(VDF-TrFE) film after temperature gets back to room temperature is also shown in Figure 5.12. A separated area with a large gap was founded. These studies suggest that the nanomesas are fully formed between 140 ºC to 160 ºC, and start to degrade at 180 ºC.

5.2.2 Thermal Effects on Ferroelectricity

In this section, we will examine the piezoelectric and ferroelectric properties of microscopically poled P(VDF-TrFE) copolymer films at a series of temperatures up to Curie point using PFM in combination with single and dual frequency resonance tracking (DFRT) technique respectively. Meanwhile the amplitude, phase, quality factor, and resonance frequency of the piezoresponse will be determined simultaneously.

P(VDF-TrFE) copolymers powders with a molar ratio of 65/35 were dissolved in Methyl Ethyl Ketone (MEK). The weight concentration of P(VDF-TrFE) in the solution was controlled to be 5%. The solution was spin coated onto silicon wafer sputtered with 100 nm thick gold as bottom electrode, and the resulting P(VDF-TrFE) films have thickness around 600-700 nm. The coated films were baked at 80^{o}C for 30 minutes to eliminate solvents, and then annealed at 130^{o}C for over 6 hours for crystallization.

Nanolithography mode of scanning probe microscopy was used to write ferroelectric domain patterns on a P(VDF-TrFE) sample. DC voltages of -66V and 66V were applied to the conductive tip (Ultrasharp NSC18/Pt/AlBS, MicroMasch) according to the predetermined pattern while scanning the sample surface, which poled the P(VDF-TrFE) films into different polar domains. The film was then heated to different temperatures up to 120^{o}C using an AR PolyHeater, and the corresponding PFM phase and amplitude images of the written domains were examined. The temperature on the surface of the film was measured and calibrated by thermocouple (Fluke 52 K/J Thermalmeter). All the PFM characterizations were carried out on MFP-3D using a high voltage PFM module and conductive tip. Two different techniques were used, one based on single frequency, wherein an AC voltage of 6.6 V and 779.6 kHz near the second resonance was applied to the conductive tip while scanning the sample surface, and the corresponding piezoelectric vibration of the sample was measured. The DFRT technique was also used, where AC

voltage of 11V was applied to the conductive tip while scanning the sample surface under two frequencies 331kHz±7.5kHz near the first resonance, which generated two piezoresponse amplitudes during tuning process. This allows tracking resonances while scanning over the samples with varying stiffness. Furthermore, switching characteristics of P(VDF-TrFE) film at different temperatures were studied, by applying a sequence of DC voltage in the form of a triangle wave up to ±44V with a step of 1.76 V to the conductive tip, imposed by an AC voltage of 2.2 V and 795±20kHz to measure the corresponding PFM phase and amplitude with DC voltage on and off, allowing us to probe the piezoresponse phase and amplitude in term of DC bias voltage.

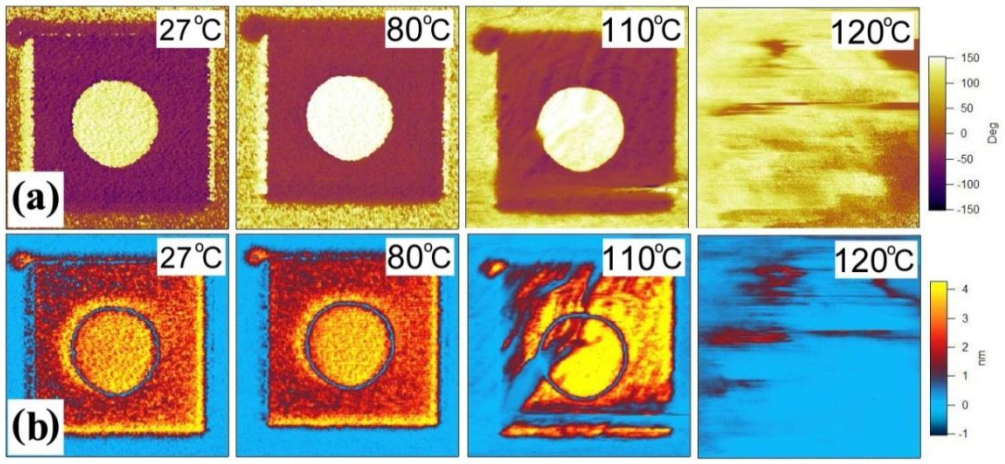

Figure 5.13 PFM phase (a) and amplitude (b) images of written domains of P(VDF-TrFE) at 27°C, 80°C, 110°C, and 120°C obtained using single frequency; the diameter of the circle is 3um, the length of the surround square is 6um, and the scanning area 8×8 um^2.

A ferroelectric domain pattern is first written on a P(VDF-TrFE) film at room temperature, with a positively polarized circle of 3μm in diameter embedded in a

negatively polarized square of 6 um in length, and its piezoresponse is examined in a 8×8 um^2 area under single frequency at different temperatures, as shown in Figure 5.13 for both PFM phase and amplitude. At 27 ^oC, the observed PFM phase and amplitude images reflect the original written pattern very well, having a clear interface between the positively polarized circle and negatively polarized square with phase contrast around 180^o, indicating their opposite polarities. Large PFM amplitude as high as 2.5 nm is observed, indicating its excellent piezoelectricity, and the positively polarized circle appear to have slightly higher piezoresponse. Outside the negatively polarized square, the PFM amplitude is substantially small, suggesting that poling is essential to the good piezoelectricity of P(VDF-TrFE) films. With temperature increasing to 80^oC, little change is observed for both PFM phase and amplitude. With further increase of temperature to 110^oC, changes in both PFM phase and amplitude images are observed. In particular, some areas in the written domain have sharply reduced PFM amplitude, indicating the reduction of piezoelectricity approaching Curie temperature. At Curie temperature of 120^oC, contrasts in PFM phase image largely disappear, and the PFM amplitude also vanishes, suggesting the loss of piezoelectricity beyond Curie temperature. To appreciate the thermal variation of piezoresponse of microscopically poled P(VDF-TrFE) films more clearly, we averaged the PFM amplitude and phase over the written domains, and plotted it as function of temperature, as shown in Figure 5.14. It is observed that up to

100°C, the phase contrast between positively and negatively polarized domains remains approximately 180°, suggesting good thermal stability of the written domains up to this temperature. The PFM amplitude, on the other hand, increases with temperature initially, reaching maximum at 60°C, and then starts to decrease, and drop to close zero sharply beyond 110°C. This can be understood from the increased dielectric permittivity and reduced spontaneous polarization when the temperature is increased toward Curie point, with both contributing to the electrostriction of P(VDF-TrFE). Even in the absence of piezoelectricity, surface vibration will be induced due to electrostatic interaction, resulting in nonzero yet small PFM amplitude beyond ferroelectric Curie temperature.

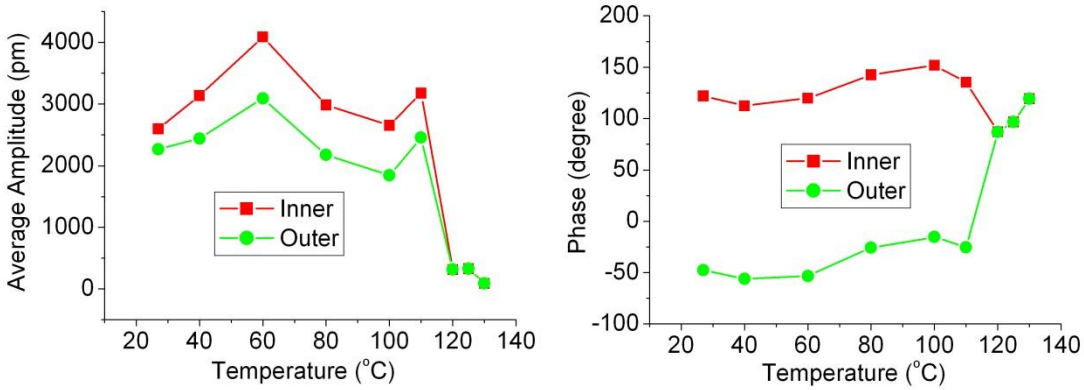

Figure 5.14 The variation of average PFM amplitude (left) and phase (right) of written domains in P(VDF-TrFE) film with respect to temperature.

The maximum PFM amplitude shown in Figure 5.14 is over 4000 pm, while the applied AC voltage is only 6.6 V, suggesting a nominal piezoelectric coefficient over 600 pm/V, more than one order of magnitude higher than 38pm/V reported for P(VDF-TrFE)

measured at room temperature. Using the essence of DFRT technique, we reexamined the piezoresponse of P(VDF-TrFE) copolymer film written into two positively and negatively polarized square domains at different temperature, as shown in Figure 5.15, with the PFM amplitude images shown in Figure 5.15 (a), and the mapping of quality factor and nature frequency shown in Figure 5.15 (b) and (c). The corresponding variations of averaged PFM amplitude (a), quality factor (b), PFM amplitude at resonance corrected by quality factor (c), and resonance frequency (d) with respect to temperature are shown in Figure 5.15 for the inner and outer written squares, as well as the unpoled edge areas outside the outer square. It is observed that the evolution of PFM amplitude image with respect to temperature is similar to that of Figure 5.14, though the value of amplitude appears to be smaller due to different orders of resonance peaks involved and the fact that DFRT uses frequencies away from resonance peak. On the other hand, new information on the quality factor Q becomes available. At room temperature of 27^{o}C, distribution of Q is rather uniform in the poled region, close to 4.9, while outside the poled domains, there are more white spots wherein the numerical procedure fails to yield a solution for Q and ω_0.

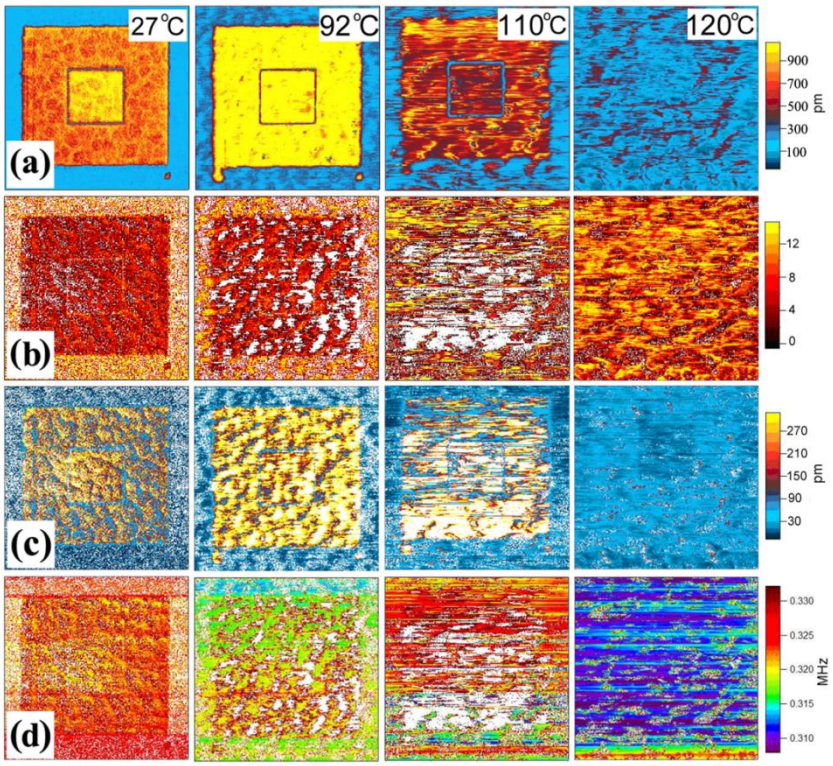

Figure 5.15 (a) PFM amplitude image, (b) mappings of quality factor, (c) mapping of resonance amplitude corrected by quality factor, and (d) resonance frequency of written domains of P(VDF-TrFE) at 27°C, 92°C, 110°C, and 120°C; the inner positively polarized square has length of 6μm, while the outer negatively polarized square has length of 15μm, and the scanning area is 20×20 μm^2.

We do observe variations of quality factor and nature frequency not only with respect to temperature, but also spatially between poled and unpoled regions for which contrasts vanish at 120^{o}C as expected. From Figure 5.15 (c), it is clear that the nature frequency decreases with increased temperature in general, consistent with thermal induced softening of the film. The variation of quality factor, on the other hand, appears to be smaller. The anomaly of Figure 5.16(b) and (c), particularly at 110^{o}C, is probably artifact due to undetermined values in large white areas. From these data, it can be estimated that

the piezoelectric coefficients d_{33} ranges from 19.4 to 23 pm/V, slightly smaller than 38pm/V reported for P(VDF-TrFE) measured at room temperature[4-6].

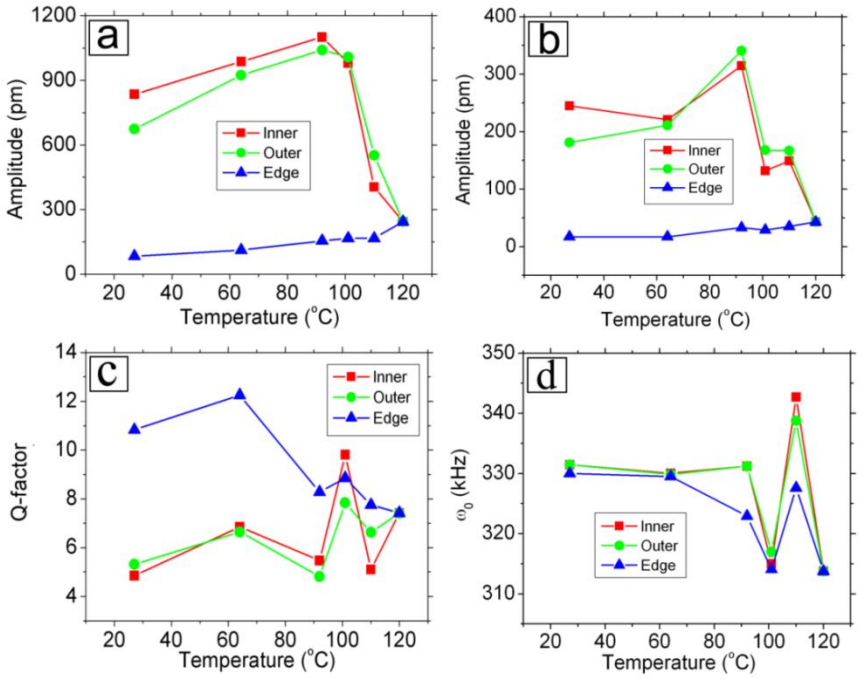

Figure 5.16 The variation in measured PFM amplitude (a), amplitude divided by quality factor factor (b), quality factor (c), and nature frequency (d) of P(VDF-TrFE) with respect to temperature, all averaged spatially.

Finally, we examined the switching characteristics of P(VDF-TrFE) film at different temperatures using local switching PFM, by applying a sequence of DC voltage in triangular wave form to switch its polarization, while simultaneously examine its piezoresponse by imposing an AC voltage. Typical phase-voltage hysteresis and amplitude-voltage butterfly loops are obtained, which are combined into a single hysteresis loop in term of $A\cos\phi$ vs. DC voltage, as shown in Figure 5.17 for the data obtained in the second cycle. Since the loops at low temperatures and high temperatures

are difficult to differentiate at this scale, they are also shown in the insert with smaller scale.

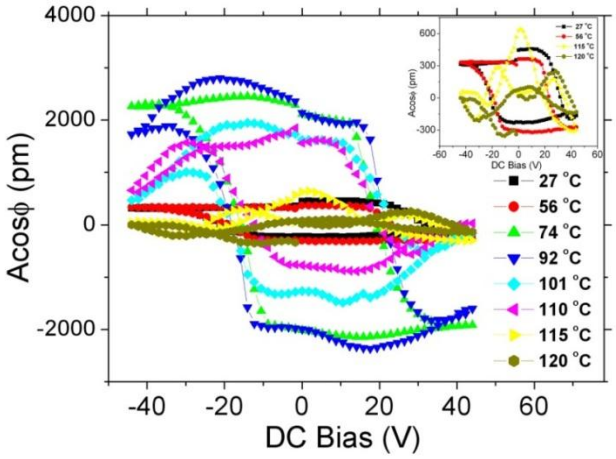

Figure 5.17 PFM hysteresis loops of P(VDF-TrFE) at different temperatures.

Typical hysteresis loops are observed up to 110^{o}C, beyond which the loops become irregular, signaling the loss of ferroelectricity. The PFM amplitudes at intermediate temperature range, from 74^{o}C to 100^{o}C, appear to be much higher than those near room temperatures, consistent with what we observe in Figure 5.16. On the other hand, the coercive fields are comparable at all temperatures, and the variation is much smaller. This is more clearly seen in Figure 5.18, where we plot coercive field and maximum PFM amplitude versus temperature.

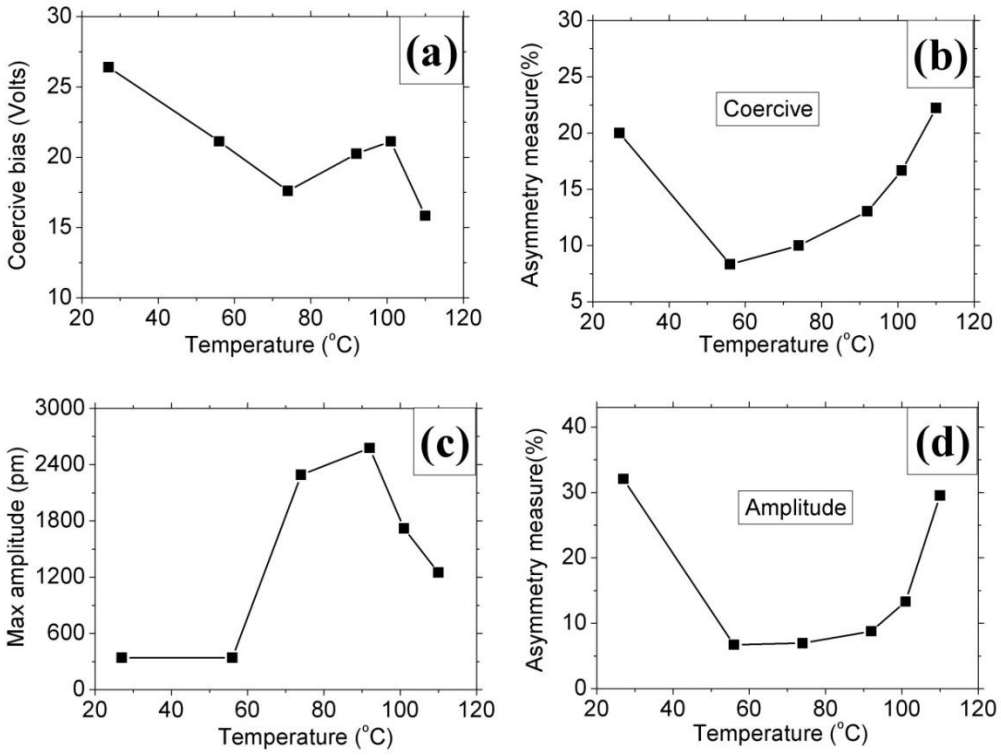

Figure 5.18 The variation in coercive field (a); the coercive field asymmetry (b); max amplitude (c); and the amplitude assymemetry field (d) with respect to temperature.

In general, the coercive field decreases with increase of temperature, as switching is enhanced by thermal fluctuation, while PFM amplitude shows a peak at intermediate temperature. To examine the asymmetry of the hysteresis loops, we define two asymmetry measures, one as $\frac{|V^+ + V^-|}{V^+ - V^-} \times 100\%$ for coercive field, representing the asymmetry in applied voltage, where V^+ and V^- are positive and negative coercive voltages read from the PFM hysteresis loop, and the other as $\frac{|(A\cos\phi)^+ + (A\cos\phi)^-|}{(A\cos\phi)^+ - (A\cos\phi)^-} \times 100\%$, representing the imprint bias of the piezoresponse,

where $A\cos\phi$ is read from the PFM hysteresis loop at zero DC bias, and the superscript + and – signs are used to denote its polarity. The asymmetry measure is in the range of 20%, reaching minimum in the intermediate temperature, and is much smaller than those observed in a random copolymer.

5.3 Nanoimprinting of Ferroelectric Nanostructure

The spontaneous formation of crystalline ferroelectric nanomesas as discussed above can create approximately 100 nm size nanostructures in P(VDF-TrFE) copolymer films, though the morphology of these nanomesas are not well controlled. As a result, nanoimprint lithography[7] are adopted in this study to fabricate the regular P(VDF-TrFE) nanostructure arrays.

5.3.1 Nanoimprint Lithography

Nanoimprint lithography (NIL) is a simple process conceptually, as shown in Fig 5.19. A polymer film is coated onto a target substrate first. An imprint mold with patterned features is then pressed against the polymer film heated above its glass transition temperature, mechanically deforming it into the inverse shape of the mold. Finally, the mold is released from the polymer, leaving the polymer film on the target substrate patterned with the reverse topology of the mold, and thus transfers the pattern from the imprinting mold to the imprinted film.

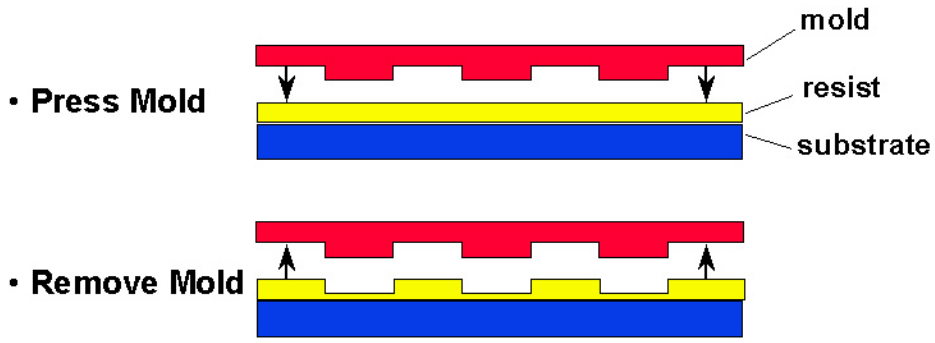

Figure 5.19 Schematics of nanoimprint lithography process.

In this study, we introduce a process using thermal plates press technique, then we develop a rapid nanoimprinting process using air cushion press to pattern a large area of polycrystalline ferroelectric P(VDF-TrFE) copolymers into regular arrays of ferroelectric patterns. Both of the imprinted patterns have feature size smaller than 200nm, which is among smallest in all the imprinted ferroelectric patterns reported in literature. The rapid nanoimprinting process takes just 3 minutes, one order of magnitude shorter than all the previous studies[8-10].

5.3.2. Nanoimprint by Hot Pressing

Thermal based NIL was the first imprinting process developed. With the thermal plate imprint process, a mold is brought to a substrate surface coated with a polymer (resist). The resist is heated above its glass transition temperature. The resist, such as P(VDF-TrFE) thin film in our study, is thermoplastic, and thus it will becomes viscous when temperature is higher than its glass transition temperature of 130^{o}C, which allows it

to deform according to the mold features. The P(VDF-TrFE) thin film is then cooled, becomes solid, and the mold is removed.

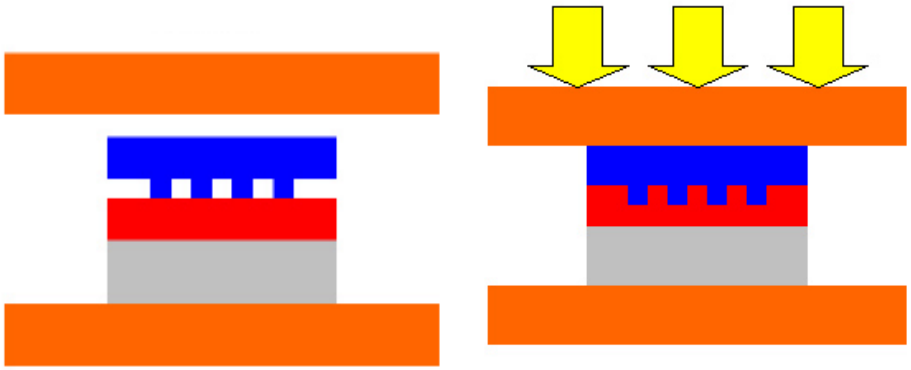

Figure 5.20 The process of thermal imprinting. The top and bottom imprint plates were heated to the imprint temperature (left); Force was applied to the plates such that the desired pressure between mold and target sample was achieved (right).

We use Specac's Atlas Series Manual Hydraulic Press with electrically heated platens as hot press, as shown in Figure 5.21, which is available in 15 and 25 ton load configurations, and can heat up to 300^{o}C.

Figure 5.21 Specac hydraulic press with electrically heated platen.

P(VDF-TrFE) thin film with 600nm thickness is deposited by 5% weight concentration solution, with 20 nm gold coated glass as the substrate. The molds for this study were fabricated through sequential electron beam lithography and reactive ion etching at National Institute Materials Science (NIMS), Japan. Molds with nanodisks were designed and prepared with dot diameter and edge-to-edge distance of 410 nm and 220 nm respectively; the active area of all of the patterns is 180 μm × 180 μm. To avoid damage, the mold and sample were embed by soft materials such as a pile of 10 mm thick paper when they undergo high pressure by hot press. It takes 20 minutes to heat the mold and sample from room temperature to imprinting temperature, which is chosen to be 135^{o}C. We hold the plates and paper-mold-sample-paper system for 1 hour. We then increase the press to 60kg and hold it constant for 2 hour before reduces it to room temperature in about 20 minutes, after which the pressure is released and the mold is removed. Figure 5.22 shows the imprinting results with optimal conditions using hot pressing technique. Excellent pattern transfer between imprinting mold and imprinted film is achieved, with the imprinted nanohole patterns being regular and uniform throughout the area.

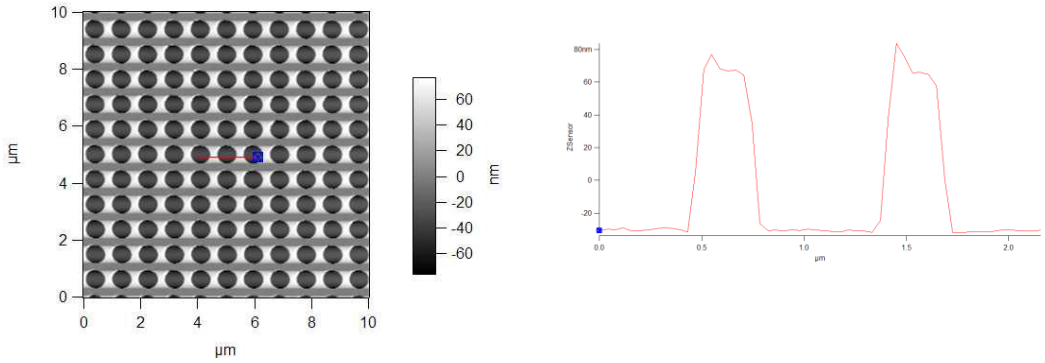

Figure 5.22 AFM topography images and cross section of P(VDF-TrFE) nanohole arrays patterned using hot pressing technique.

Thermal based NIL suffers some draw-backs, including higher imprint pressure that tends to damage the mold and samples, the imprinting results being sensitive to the surface quality of the solid plates and samples, and the imprinting pressure depending on the precise contact area. So an alternate imprinting technique using air cushion press was utilized in our following research.

5.3.3 Nanoimprinting by Air Cushion Pressing

Nanoimprinter using air cushion press technology (ACP)[11] is shown in Figure 5.23(a). ACP utilizes a gas to press the mold and substrate against each other in a chamber. Since air pressure instead of mechanical contact is used for pressing, it eliminates surface effects of the plates and samples. Thus the ACP method can enhance the imprinting quality, reduce damage to the mold, and prolong mold lifetime.

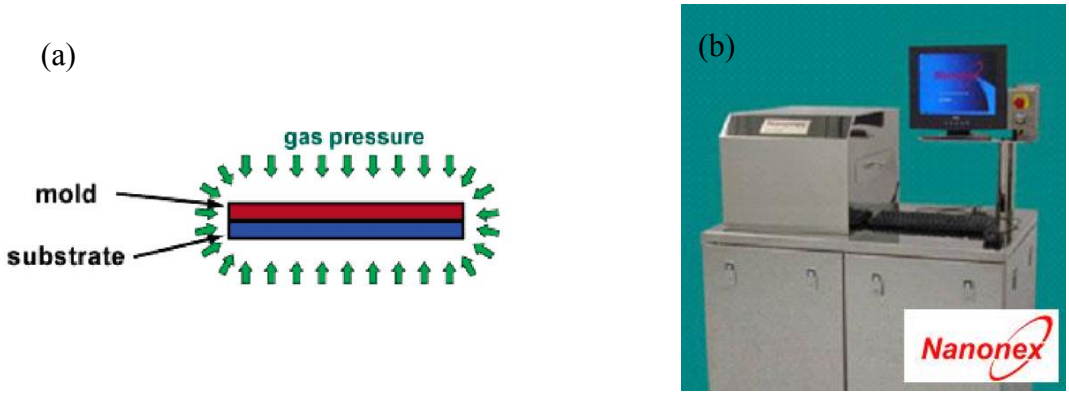

Figure 5.23 (a) Schematic of the air cushion press (ACP), and (b) NX-1000 (Figure courtesy He Gao, Princeton University)

NX-1000, as show in Figure 5.23 (b), is one of the thermal NIL instruments using ACP technique. Typical heating and cooling cycles are shown in Figure 5.24, and it is observed that the heating take 6 seconds from room temperature to 130°C, and cooling takes about 20 seconds. The whole process including evacuating the chamber takes 57 second to complete. Temperature and pressure in the process can be controlled within 1%.

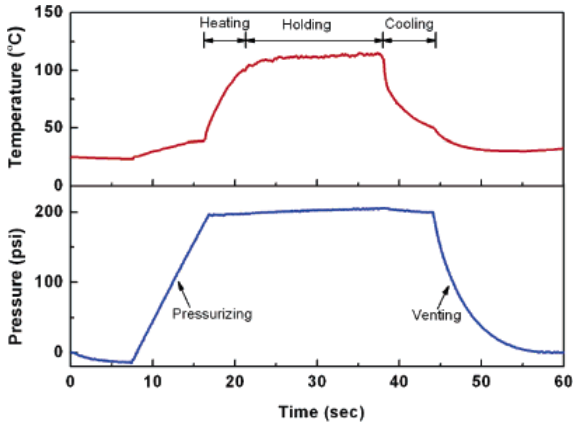

Figure 5.24 The temperature and pressure recorded during one typical cycle of NX-1000 heating and cooling. (Figure courtesy He Gao, Princeton University)

Three types of gratings are used as the imprinting molds: two one-dimensional line gratings obtained from LightSmyth Technologies, Inc. (Eugene, OR), one has a period of 833.3nm, line width of 416 nm, and pattern depth of 200 nm, and the other has a period of 278 nm, line width of 139 nm, and pattern depth of 110 nm; the third one is a two-dimensional square grating obtained from MikroMasch USA (San Jose, CA) with a period of 3 μm, line width of 1.1 μm, and pattern depth of 1.0 μm. The molds are either untreated and used as received, or cleaned by oxygen plasma etching for 3 minutes to produce a hydrophilic surface, or cleaned by oxygen plasma using Barrel oxygen plasma etching for 3 minutes followed by vapor deposition of a layer of trichloro (1H,1H,2H,2H-perfluorooctyl)-silane (97%, Sigma-Aldrich Inc., Saint Louis, MO) in a vacuum desiccator to create a hydrophobic surface.

In our study, a silicon mold is used to cover the full 20mm diameter area of PVDF thin film. Imprinting temperatures of 130^{o}C, 135^{o}C, 140^{o}C, and 150^{o}C, are chosen for comparison. Heating the mold and sample from room temperature to imprinting temperature takes 6 to 10 seconds. The imprinting temperature and pressure are held constant for 3 minutes. The temperature is then reduced to room temperature in about 20 seconds, after which the pressure is released. The P(VDF-TrFE) samples suffer high pressure at temperature of paraelectric phase, which is sufficient for polymer chains to reorganize and produce film with good out-plane crystallinity in very short time.

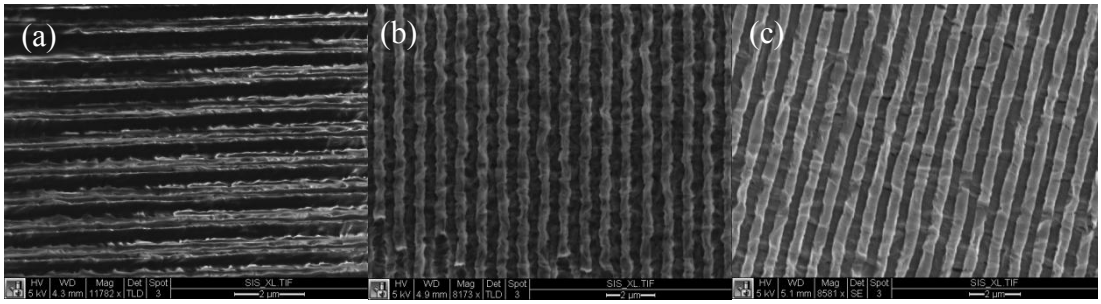

Figure 5.25 SEM images of imprinted P(VDF-TrFE) patterns using three different molds; (a) hydrophilic silicon mold treated by oxygen plasma, with imprinting temperature of 140^{o}C; (b) untreated and (c) fluorosilane -coated hydrophobic silicon molds, with imprinting temperature of 150^{o}C.

We first examine the effects of imprinting conditions, such as the imprinting molds, temperature, and film thickness on the imprinted patterns. P(VDF-TrFE) copolymers are polar in molecular structure, and thus tend to be hydrophilic in nature. To examine the effects of mold characteristics on the imprinted patterns, we use three types of imprinting molds, and the resulted structures are shown by SEM images in Figure 5.25. It is observed that the hydrophilic silicon mold treated by oxygen plasma results in patterns with substantial amount of defects, and the surface of the structure is very rough, suggesting that it is difficult to separate the mold from the imprinted film, as we would expect.

On the other hand, the pattern imprinted by silicon mold coated with a thin fluorosilane layer to make it hydrophobic has the best pattern transfer between the mold and the imprinted film, and the surface of the structure is relative smooth, suggesting that the mold separation is much easier, and does not impose a major problem. The untreated

silicon mold produces a pattern that is similar to that imprinted by coated molds, though it appears that there are slightly more defects in the pattern. This suggests that coated silicon mold is the best for nanoimprinting of P(VDF-TrFE) copolymers, and hydrophilic mold cannot produce a satisfactory pattern transfer. Thus we will limit ourselves to either coated or untreated silicon molds in the following studies.

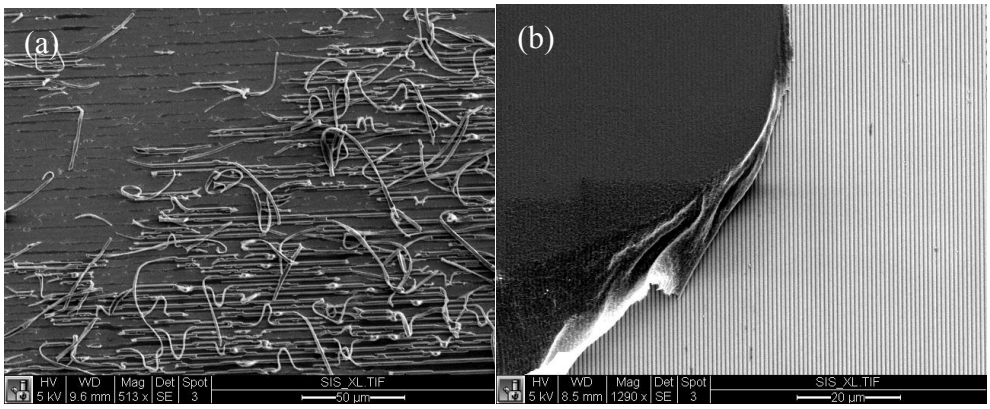

Figure 5.26 SEM images of P(VDF-TrFE) patterns imprinted at 150^{o}C; image of sample surface after mold removed (a), and overall of mold with part of film attached (b).

None of the imprinted pattern in Figure 5.25 is straight, suggesting that the imprinting temperature is not optimal. We examine the effect of different imprinting temperatures on the imprinted pattern, as shown in Figure 5.26. It turns out that it is very difficult to separate the mold from the imprinted film at an imprinting temperature of 150^{o}C, which is evident from Figure 5.26 (a); From Fig. 5.26 (b), it is seen that the imprinted pattern is peeled off from the substrate Figure 5.27 shows the image of imprinting results with temperature of 140^{o}C, the separation of the mold is much easier,

though the imprinted pattern is not straight, similar to those shown in Figure 2.12(b), (c).

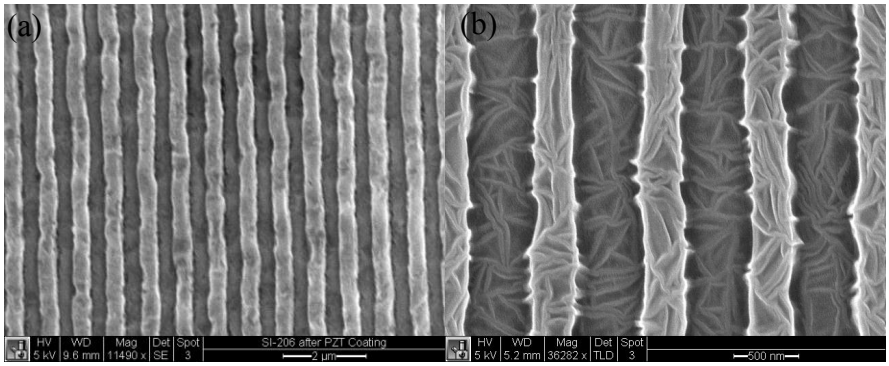

Figure 5.27 SEM images of P(VDF-TrFE) patterns imprinted at 140^{o}C with different scales.

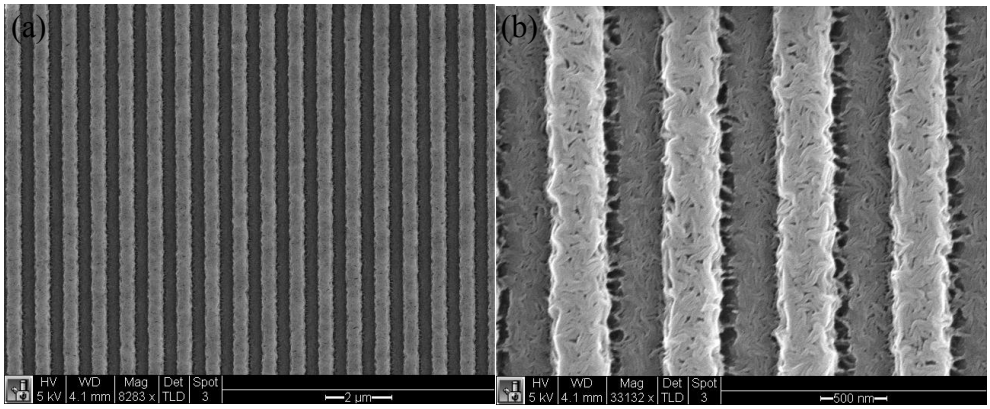

Figure 5.28 SEM images of P(VDF-TrFE) patterns imprinted at 135^{o}C; overall of pattern (a) and detailed morphology of polymeric pattern (b).

At imprinting temperatures of 135^{o}C as shown in Figure 5.28, excellent pattern transfer between imprinting mold and imprinted film is observed, with the imprinted pattern being straight and uniform throughout the area. The edge of the pattern appears to be rough, and higher magnification SEM image shown in the Figure 5.28 (b) suggest that the edge roughness is resulted from the polymer structure itself, instead of from

imprinting process. Such a polymer structures will ultimately limit the resolution of nanoimprinting of ferroelectric polymers. The pattern imprinted at 130^{o}C as shown in Figure 5.29 is similar those imprinted at 135^{o}C, and it becomes rather difficult to imprint the polymer at 120^{o}C. Thus we identify 130^{o}C to 135^{o}C as the optimal imprinting temperatures for P(VDF-TrFE) copolymers, and limited ourselves to this temperature range in the following studies.

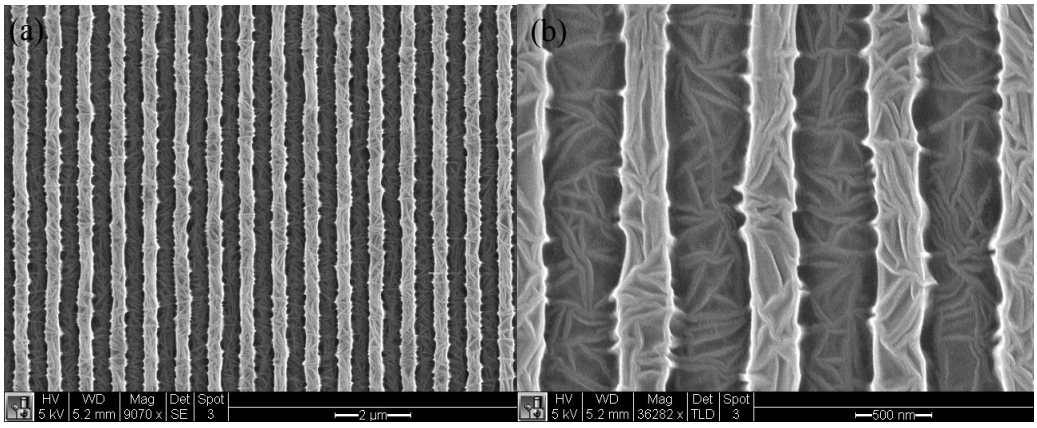

Figure 5.29 SEM images of P(VDF-TrFE) patterns imprinted at 130^{o}C; overall of pattern (a) and detailed morphology of polymer (b).

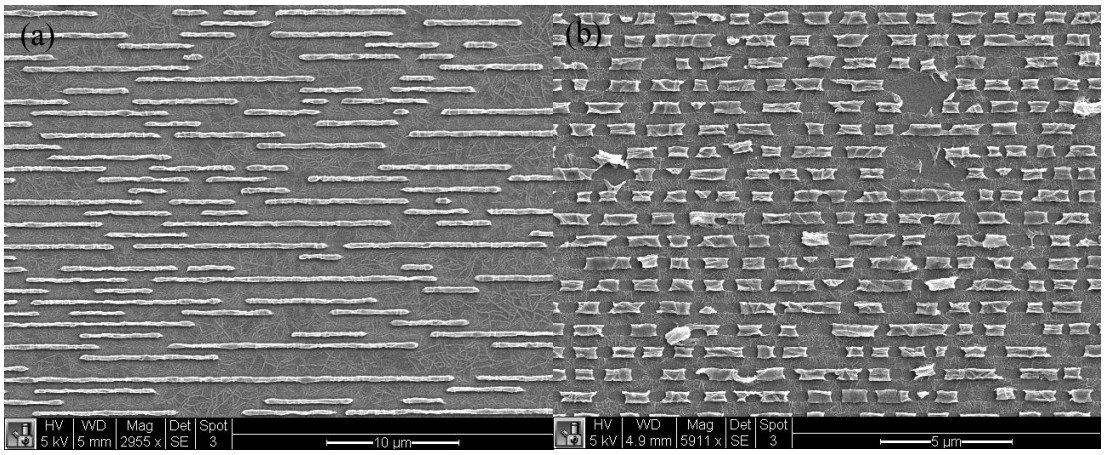

Figure 5.30 SEM images of structure imprinted from ultrathin film of 60nm.

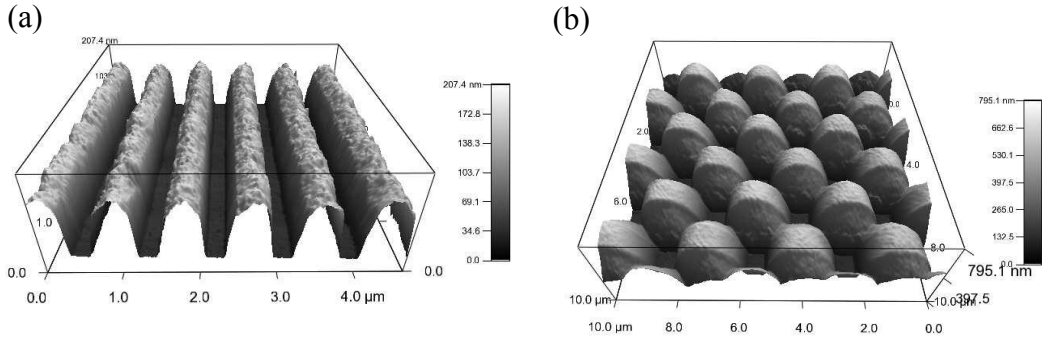

Figure 5.31 AFM topography images of one-dimensional line pattern imprinted from (a) 170nm film with 200nm mold pattern depth and (b) square pattern imprinted from 300nm thick with 1µm mold pattern depth.

A somewhat surprising phenomenon we observe is the effect of film thickness on the imprinted pattern, as shown in Figure 5.30. If we imprint an ultra-thin film of 60 nm, the imprinted pattern is broken into segments, as shown in Figure 5.30 (a) and (b). This could be resulted from the loss of stability of thin imprinted pattern at elevated temperature. For films with thickness over 150 nm, this does not appear to be an issue, but AFM images suggest that the topography of the top surface of the imprinted pattern is largely influenced by the thickness of the imprinted film and pattern depth on the imprinting mold. In order to get a flat top surface of the imprinted pattern, the film thickness cannot be much smaller than the pattern depth on the imprinting molds. Otherwise, the imprinted pattern will have round top surface, with center to be higher and edges to be lower, as shown in Figure 5.31 (a), where the film is 170 nm thick and the pattern depth on the mold is 200 nm, and in Figure 5.31 (b), where the film is 300 nm thick, and the pattern depth on the mold is 1µm. These suggest that for thinner film, the polymer is pushed up

in the center, yet it could not touch the bottom surface of the imprinting mold, resulting in a round top surface.

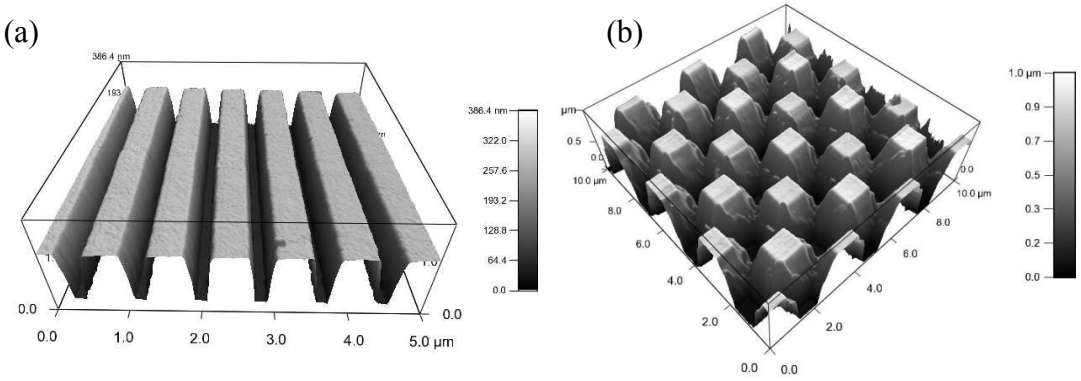

Figure 5.32 AFM topography images of one-dimensional line pattern imprinted from (a) 190nm film with 200nm mold pattern depth and (b) square pattern imprinted from1µm thick with 1µm mold pattern depth.

For thicker film, wherein the polymer is able to touch the bottom surface of the imprinted mold, then very flat top surface is observed in the imprinted pattern, as shown in Figure 5.32 (a), where the film is 190 nm thick imprinted by 200 nm deep pattern, and in Figure 5.32 (b), where the film is 1µm imprinted by 1µm pattern. Figure 5.33 shows a SEM cross-section image that confirms this analysis: the initial film thickness is around 190 nm, after imprinting, the elevated pattern is around 200 nm high, consistent with the pattern depth of the mold, and a thin residual layer around 70-90 nm thick is observed underneath it. Such a distribution of elevated pattern and residual layer is also consistent with mass conservation analysis with the initial thickness of 190 nm.

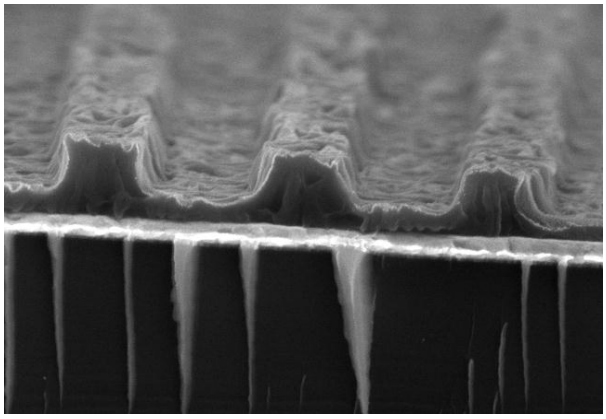

Figure 5.33 the SEM cross section image of 300nm film with 190nm mold. (same sample as of Fig 2.15 (a))

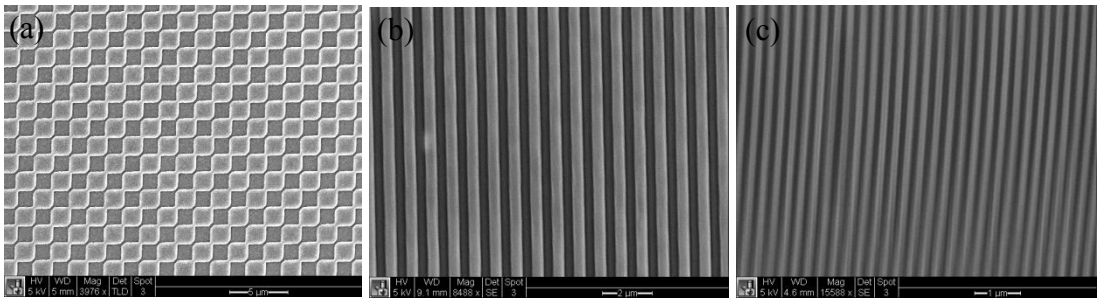

Figure 5.34 SEM images of typical patterns imprinted at optimal conditions; two-dimensional square pattern (a); one-dimensional line pattern, with feature size of 417 nm (b); one-dimensional line pattern, with feature size of 139 nm (c).

Finally, we show some typical SEM images in Figure 5.34 for ferroelectric pattern imprinted with optimal conditions. Both two-dimensional square pattern and one-dimensional line patterns are presented, with the finest feature size being 139 nm, comparable to smallest feature size of imprinted ferroelectric polymer recently reported.

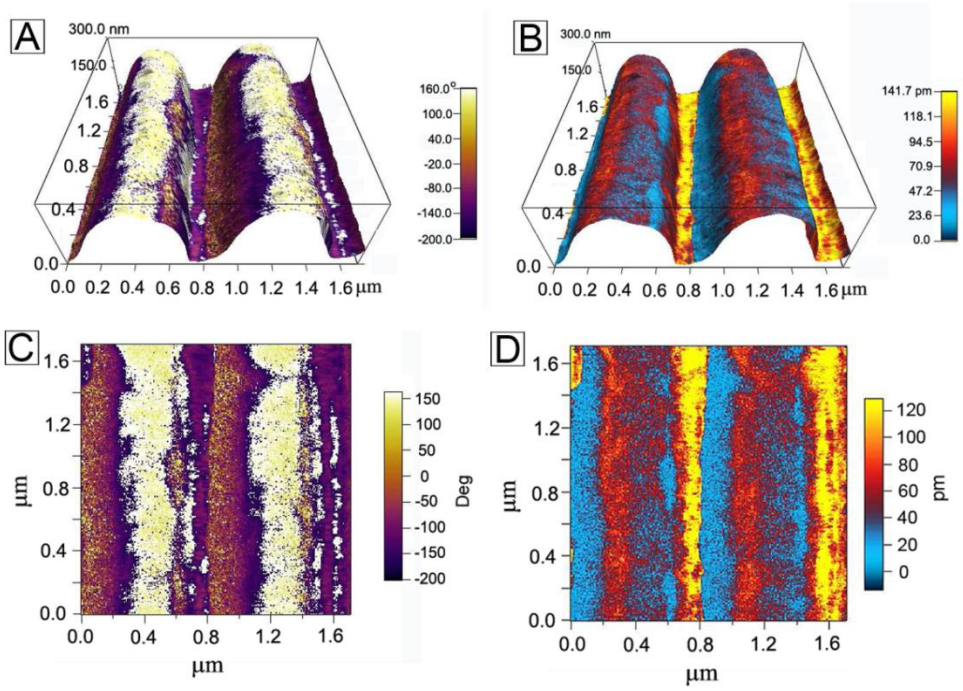

Figure 5.35 Piezoresponse force microscopy (PFM) of imprinted P(VDF-TrFE) patterns, with an AC driving voltage of 6.6 V; (A) PFM phase image and (B) PFM amplitude image, both imposed on top of the three-dimensional (3D) topography image; the topography is represented by the vertical scale in nanometer, while PFM phase and amplitude are represented by respective color scale bars in degrees or pecometers. The corresponding two-dimensional (2D) PFM phase (C) and amplitude (D) images are also shown.

5.4 Piezoresponse Force Microscopy of Nanoimprinted P(VDF-TrFE) Thin Films

5.4.1 Piezoresponse

We have utilized piezoresponse force microscope (PFM) to characterize the ferroelectricity and piezoresponse of nanoimprinted P(VDF-TrFE) films. The PFM phase and amplitude images of nanoimprinted P(VDF-TrFE) thin film with grating patterns are

shown in Figure 5.35, with both three-dimensional (3D) and two-dimensional (2D) images displayed to better illustrate the correlation between imprinted topography and piezoresponse, where in 3D images, the piezoresponse, represented by color scale bar in degree or pm, is imposed on top of the topography as represented by vertical scale bar in nm.

Quite remarkably, even though our film is imprinted at around 135°C for only 3 minutes, and there is no post imprinting annealing process, they still show rather strong piezoelectricity even without poling. This is due to the pressure applied during the imprinting, which helps the crystallization of polymers. It is also observed that the piezoresponse does not change much along the length of the pattern, but vary substantially perpendicular to it, and the highest PFM amplitude is observed in the residual layer at the bottom of the imprinted pattern. This is because at the bottom of the pattern the polymer is subjected to the largest pressure, which tends to align the polymer chains, resulting in enhanced piezoelectricity. With a modest AC driving voltage of 6.6 V, the maximum PFM amplitude is observed over 140 pm, a decent value for an unpoled ferroelectric polymer, and comparable to piezoresponse of unpoled uniform films annealed in oven for 12 hours.

5.4.2 Ferroelectric Switching

To confirm that the protruded patterns do have good ferroelectricity and piezoresponse, we apply a sequence of DC voltage on top of 2.2 V AC voltage while measuring the piezoresponse simultaneously, resulting in local domain switching and hysteresis and butterfly loops. The results for imprinted square and line patterns are shown in Figure 5.36. Between each step of DC bias (state "On"), the DC voltage is stepped back to zero (state "Off"), and piezoresponse is measured at both "On" and "Off" states to better reveal the electric interactions between AFM tip and sample surfaces. Comparisons are also made with uniform films without any annealing, uniform film heated in NIL chamber for 3 minutes but subjected no pressing from mold, and uniform film annealed in an oven for 12 hours.

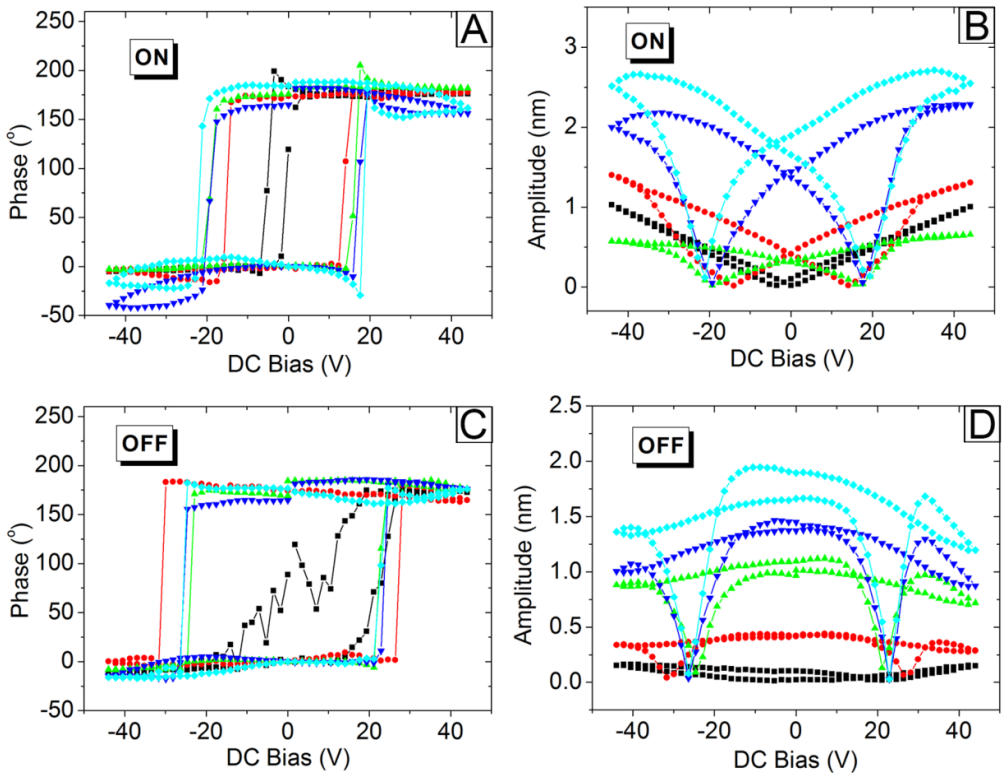

Figure 5.36 The PFM phase-voltage hysteresis loop (AC) and amplitude-voltage butterfly loop (BD) of P(VDF-TrFE) films under different processing conditions, in both "On" (AB) and "Off" (CD) states. Different films are denoted by the following legends: ▼ (NIL line); ▲ (NIL square); ◆ (uniform film annealed for 12 hours) ● (uniform film heated in NIL chamber for 3 minutes without imprinting); ■ (uniform film without annealing).

All the films are spin coated under identical conditions, with initial thickness around 600-700 nm. For PFM hysteresis under "On" state shown in Figure 5.36 (A) and (B), PFM amplitude saturates at higher DC voltage for imprinted films and uniform film under extended annealing, a strong indication that the response is mainly ferroelectric in nature. On the other hand, for films without annealing or heated in NIL chamber for just 3 minutes without imprinting, the PFM amplitude increases linearly with the applied DC

voltage and does not saturate, a strong indication that the response is dominated by electrostatic interactions. To minimize the electrostatice interactions, the hysteresis and butterfly loops in the "Off" state are also measured as shown in Figure 5.36 (C) and (D), which correlate with true ferroelectricity of the specimens much better. In particular, the linear variation of PFM amplitude with respect to DC bias is no longer present in any of these films. Again, it is noted that the PFM amplitude of nanoimprinted films without additional annealing is essentially comparable to uniform film annealed for 12 hours without imprinting, and much larger than that of films without annealing, or heated in an NIL chamber for 3 minutes without imprinting.

The amplitudes measured in "Off" state are generally smaller than those measured in "On" state, again reflecting minimized contributions from electrostatic interactions. Using the PFM amplitudes measured in "Off" state at zero DC bias and a quality factor of 10, we estimated the piezoelectric coefficient d_{33} in the range of 48-81 pm/V for nanoimprinted films and annealed uniform film. In contrast, uniform films without annealing or heated in NIL chamber without imprinting has piezoelectric coefficient d_{33} in the range of 3-19 pm/V. Furthermore, higher coercive field is observed in "Off" state than "On" state, estimated to be around 25 V for 600-700 nm films. This is comparable with bulk coercive field of 50 MV/m. The difference in coercive field between nanoimprinted films and annealed uniform films is rather small.

5.4.3 Nanolithography on Nanoimprinted P(VDF-TrFE) Copolymers Films

The ferroelectricity of the imprinted patterns enables a number of applications, such as nonvolatile memory cells for the data storage. This application utilizes the spontaneous polarization feature of ferroelectrics, which can be switched by an external electric field. We then carry out PFM nanolithography on patterned P(VDF-TrFE) copolymers films to confirm it. The tip voltage writes a domain pattern with distribution of positive and negative polarizations, forming a designed pattern of "NIL". Such a pattern can then be read from the PFM phase image, as exhibit in Figure 5.37 (A) clear showing two different phase contrasts, where the phase image is imposed on 3D topography. Before such a poling process, the PFM phase and amplitude images are similar to those shown in Figure 5.35 and thus are not presented here. It is noted that the writing process does not change the 3D topography, and even more importantly, switching appears to be rather uniform, with no cross-talk observed between adjacent cells. Some of the cells are written into two different phases, suggesting that the writing resolution can be higher than our NIL feature size. It is quite remarkable that for most area after the writing, the protruded pattern has one uniform PFM amplitude (blue in the amplitude image), and the residual layer has another uniform yet higher PFM amplitude (orange in the amplitude image), as shown in Figure 5.37 (B). In other words, within an upward or downward polarization, two different states can be differentiated, corresponding to two different magnitudes of

piezoresponse. It is also noted that these written patterns can be rewritten by applying a different distribution of positive or negative voltage during scanning. In summary, the imprinted patterns we fabricated show excellent ferroelectricity and piezoresponse without post-imprinting annealing, and this offers a promising route for patterning polymeric ferroelectric nanostructures for a wide range of functional applications.

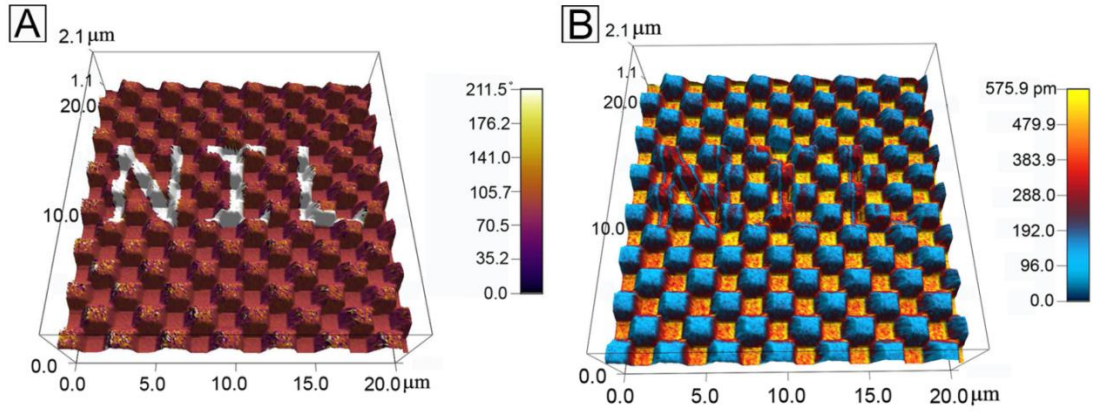

Figure 5.37 Imprinted ferroelectric film as ferroelectric nonvolatile memory cell, with an "NIL" pattern written by conductive AFM tip and read by PFM; (A) PFM phase image (indicated by color scale bar in degree), and (B) PFM amplitude image (indicated by color scale bar in pm), both imposed on 3D topography image (indicated by vertical scale bar in nm) of the imprinted film after writing.

Reference

1 M. J. Bai and S. Ducharme, Applied Physics Letters **85,** 3528 (2004).

2 M. J. Bai, M. Poulsen, and S. Ducharme, Journal of Physics-Condensed Matter **18,** 7383 (2006).

3 B. J. Rodriguez, C. Callahan, S. V. Kalinin, and R. Proksch, Nanotechnology **18,** 475504 (2007).

4 Q. M. Zhang, V. Bharti, and X. Zhao, Science **280,** 2101 (1998).

5 A. V. Bune, V. M. Fridkin, S. Ducharme, L. M. Blinov, S. P. Palto, A. V. Sorokin, S. G. Yudin, and A. Zlatkin, Nature **391,** 874 (1998).

6 K. Omote, H. Ohigashi, and K. Koga, Journal of Applied Physics **81,** 2760 (1997).

7 S. Y. Chou, P. R. Krauss, and P. J. Renstrom, Science **272,** 85 (1996).

8 Z. J. Hu, M. W. Tian, B. Nysten, and A. M. Jonas, Nature Materials **8,** 62 (2009).

9 L. Zhang, S. Ducharme, and J. Li, Applied Physics Letters **91,** 172906 (2007).

10 S. J. Kang, Y. J. Park, J. Hwang, H. J. Jeong, J. S. Lee, K. J. Kim, H. C. Kim, J. Huh, and C. Park, Advanced Materials **19,** 581 (2007).

11 H. Gao, H. Tan, W. Zhang, K. Morton, and S. Y. Chou, Nano Letters **6,** 2438 (2006).

Chapter 6 Biological Ferroelectricity in Aortic Walls

Coupling between mechanical and electrical phenomena is ubiquitous in biological systems and a wide variety of biological tissues are found to be piezoelectric and pyroelectric with spontaneous polarization. In fact, piezoelectricity is believed to be a universal property of living tissues that may play a significant role in several physiological phenomena, for example, remodeling of bones and the formation of thrombi due to injury of blood vessels. Ferroelectricity, however, has not been reported in biological tissues yet. In this chapter, we have discovered, for the first time, that porcine aortic walls and arterial elastin are not only piezoelectric, but also ferroelectric, which is confirmed by tip induced hysteresis and butterfly loops characteristic of polarization reversal.

6.1 Biological Ferroelectricity uncovered in Aortic Walls

6.1.1 Introduction

Piezoelectricity, where the electric field and mechanical deformation are linearly coupled, was first discovered in bones in 1957[1-3], and was subsequently reported in many biological tissues and systems[4-10]. A subset of piezoelectrics is known as pyroelectric with spontaneous polarization, and such pyroelectricity was observed in bones and tendons in 1966[11], and later, in other biological tissues as well[12-15]. Inorganic and

synthetic pyroelectric materials are often ferroelectric with spontaneous polarization switchable by electric fields; however, even five decades after the first reports of pyroelectricity in bones and tendons, ferroelectricity in soft biological tissues has yet to be observed.

The ability to switch the polarization of inorganic and synthetic ferroelectrics is essential to many technological applications, and the biological significances of piezoelectricity and pyroelectricity are widely recognized[15-17]. Given seemingly ubiquitous piezoelectricity in biological tissues, it is quite surprising that ferroelectricity has not been observed, even though its potential biological significance have been postulated[18,19]. Piezoresponse force microscopy (PFM) is a powerful tool to probe electromechanical coupling in piezoelectric and ferroelectric systems at the nanoscale[20-22], and in recent years, it has been applied to study a variety of biological tissues and materials. These include: human bones[23] and teeth[24], tooth dentin and enamel[25,26], collagen fibrils[27,28], insulin and lysozyme amyloid fibrils, breast adenocarcinoma cells, and bacteriorhodopsin[29], as is summarized in a recent review[22]. While these studies unambiguously established piezoelectricity in biological tissues at the nanoscale, biological ferroelectricity remains elusive. Switching PFM experiments have been attempted on single collagen fibrils, from which it was concluded that they are not ferroelectric, as neither PFM amplitude nor PFM phase varies with DC bias[25,26]. Since

electromechanical coupling of collagens is believed to underpin the piezoelectricity observed in bones and other biological tissues, this seems to explain the lack of ferroelectricity in biological tissues so far. In this work, we demonstrate that porcine aortic walls are not only piezoelectric, but also ferroelectric, which is confirmed by their hysteresis and butterfly loops characteristic of polarization reversal.

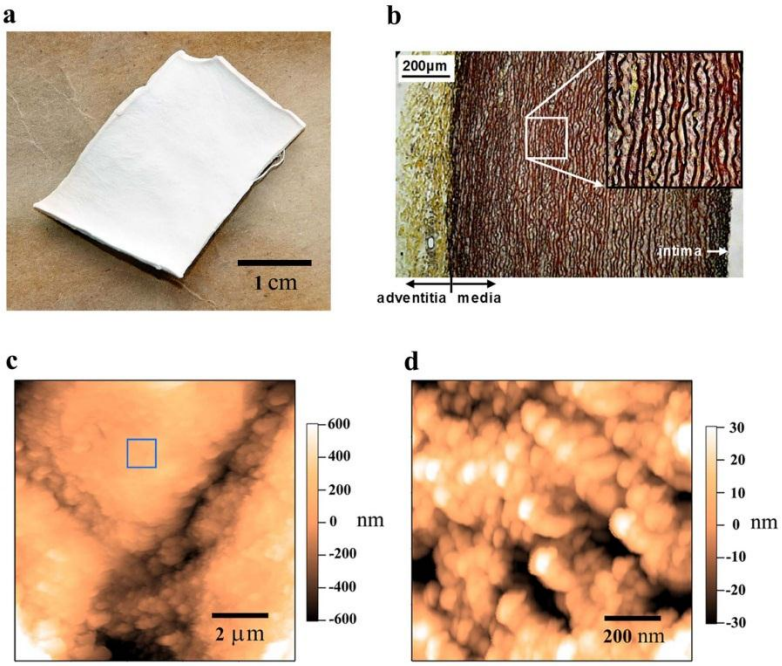

Figure 6.1 Structure of aortic wall: (a) photo of the aortic tissue sample with its inner wall on top, (b) histological image of the cross-section of artery, (c) AFM topography mapping of inner wall over a $10\times10\mu m^2$ area, and (d) AFM topography mapping of inner wall zoomed-in over a $1\times1\mu m^2$ area.

6.1.2 PFM Experiment on Porcine Aortic Wall

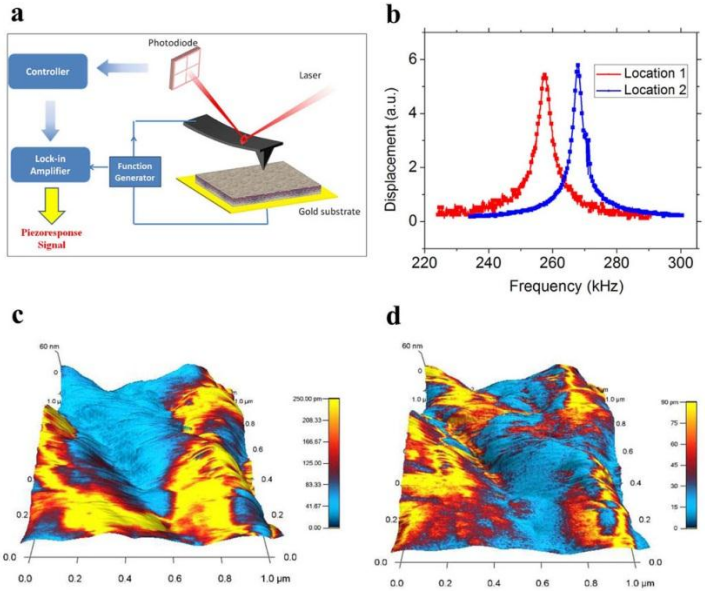

Figure 6.2 Piezoresponse force microscopy (PFM) of inner aortic wall: (a) schematics of PFM, (b) piezoresponse as a function of frequency at two different locations, and mappings of (c) vertical and (d) lateral PFM amplitude overlaid on 3D topography in a $1\times1\mu m^2$ area

The porcine aortic wall samples were provided by Prof. Yanhang Zhang of Boston University. In order to search for ferroelectricity in soft biological tissues, we carried out PFM studies on porcine aortic walls. Tissue samples were dried prior to PFM analysis, cut into 8 mm×8 mm pieces, glued onto the silicon substrate, and sputtered with 100 nm thick gold using silver paint, as seen in Figure 6.1 (a), with a thickness of approximately 0.82 mm. The aortic wall consists of three layers of intima, media, and adventitia, as observed in the Movat pentachrome stained histology image in Figure 6.1 (b). The intima consists of a monolayer of endothelial cells; the media layer is composed of concentric

rings of elastin fibers, collagen, and smooth muscle cells and a network of collagen and fibroblast cells make up the adventitia. Atomic force microscopy (AFM) topography mappings of the inner wall in Figure 6.1 (c) and (d) show the hierarchical fibrous structure composed of fine globular features. PFM was used to measure the piezoelectric effect at the inner wall by applying an AC voltage through the conductive AFM tip to excite the piezoelectric vibration of the sample, as schematically shown in Figure 6.2 (a). Since the piezoresponse for typical biological tissues is extremely small, we drove the AC voltage near the resonant frequency of the cantilever-sample system to enhance the sensitivity and the corresponding piezoresponse versus driving frequency at two different locations are shown in Figure 6.2 (b), exhibiting clear resonance peaks at different frequencies. Typical amplitude mappings of vertical and lateral PFM of aortic wall overlaid on 3D topography are shown in Figure 6.2 (c) and (d), with vertical amplitudes as high as 250 pm, while lateral amplitude in the same area is less than 90 pm; both acquired under 3 V of AC voltage. The AC frequency was set to be 265.43 kHz for the vertical PFM and 888.57 kHz for the lateral PFM. Higher lateral piezoresponse than vertical has also been observed in other regions. This is distinct from previous PFM studies on collagens, where only lateral responses have been observed. It is also noted that the aortic wall is very soft and contact scanning tends to modify the surface topography slightly, as shown by three consecutive scans in the same area, as shown in

Figure 6.3. The deflection images on the left indicate that there is a slight right shift in topography during scanning. The amplitude mappings in the middle are stable with small evolutions during different scanning. Contrasts of approximately 140^{o} are observed in the phase mappings on the right, indicating different orientations of polarization. Between different scans, small evolutions in phase contrasts are also observed, and this is the first indication that the aortic wall could be ferroelectric.

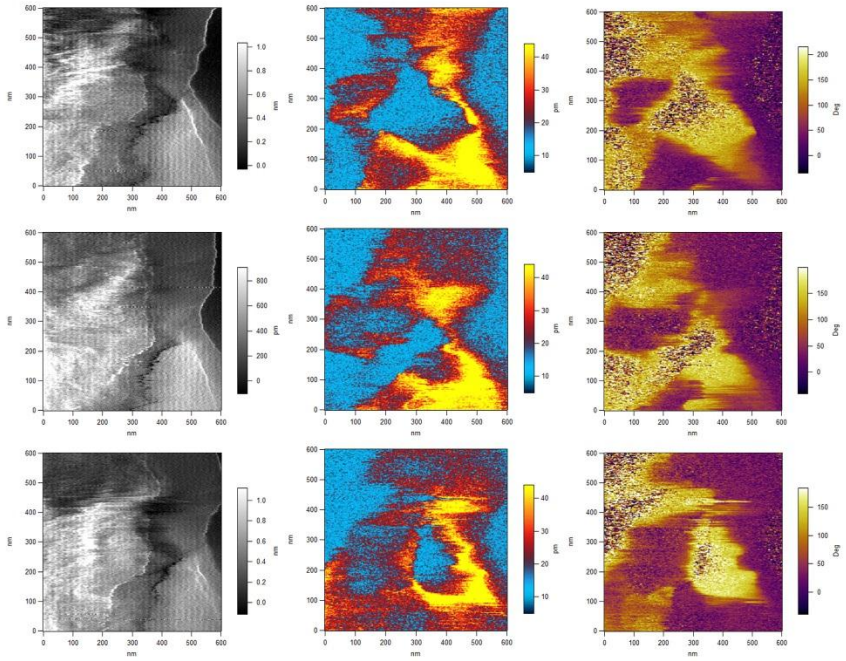

Figure 6.3 Three consecutive vertical PFM scans in a 600×600 nm^2 area using a 15 V AC drive voltage of 261.65 kHz. The deflection images (left), amplitude mappings (middle), and the phase mappings (right) are shown.

The large piezoresponse is impressive considering the modest driving voltage, yet it is not intrinsic, since it is enhanced by resonance. Substantial variations in amplitude

mapping are observed in both vertical and lateral PFM, and it is not clear whether such variation is due to the change in piezoelectricity or is caused by variation in resonance frequency instead. As seen in Figure 6.2 (b), the resonant frequency at different locations can be quite different, which can result in considerable reduction in piezoresponse magnification when the driving AC voltage is locked at a particular frequency. To avoid such a problem and enable quantitative piezoresponse analysis of aortic walls, we adopt DFRT techniques, as illustrated in Figure 6.4 (a), using actual experimental data. This allows us to track the resonance frequency when it shifts during scanning. As Chapter 2 discusses, the cantilever-sample system can be regarded as a damped harmonic oscillator, with the amplitude and phase at a particular frequency, given by:

$$A = \frac{A_0}{\sqrt{(1-\omega^2/\omega_0^2)^2 + (\omega/\omega_0 Q)^2}} \quad \text{and} \quad \phi - \frac{\pi}{2} = \tan^{-1}[Q(\omega/\omega_0 - \omega_0/\omega)],$$

which is confirmed by fittings of experimental data shown in Figure 6.4 (a). As a result, measurements at two distinct frequencies allow us to solve for amplitude and phase at the resonance, as well as the resonant frequency and quality factor.

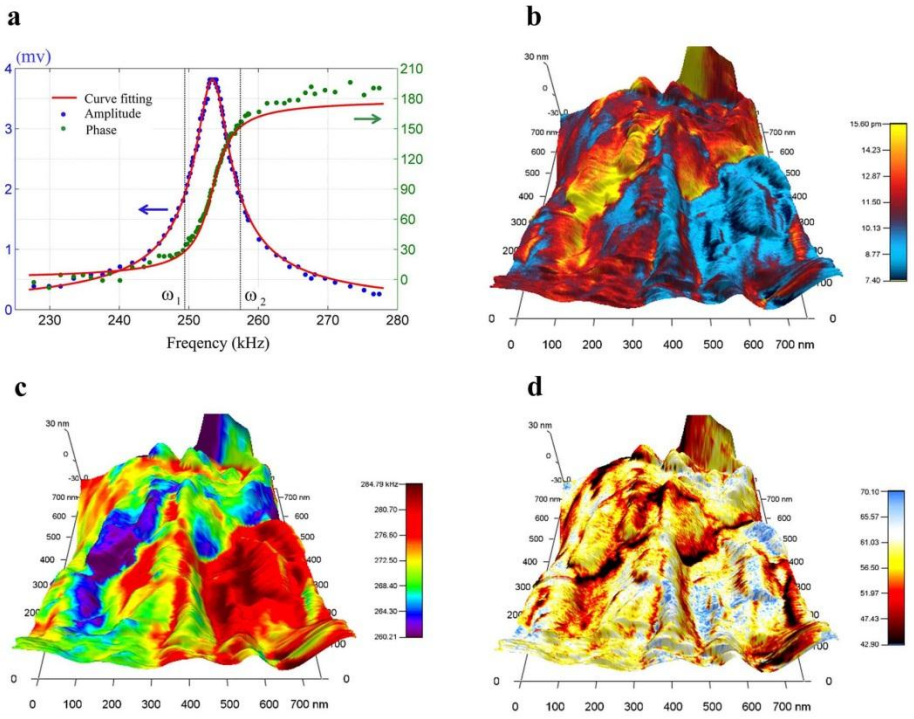

Figure 6.4 Quantitative PFM of inner aortic wall by dual frequency resonance tracking (DFRT): (a) schematics of DFRT with actual experimental data and mapping of PFM, (b) amplitude, (c) resonant frequency, and (d) quality factor in a 700×700 nm^2 area, all overlaid on 3D topography.

PFM results obtained by the DFRT mode make it possible to determine the intrinsic piezoresponse mapping by correcting the resonance magnification using the quality factor, as shown in Figure 6.4 (b) with the uncorrected amplitude mapping given in Figure 6.5 (a). It is evident that the intrinsic piezoresponse is substantially smaller after correction, with a maximum amplitude of less than 16 pm despite a relatively large driving votage of 22 V. This leads to an estimate of piezoelectric coefficient in the order of 1 pm/V, two orders of magnitude larger than that reported by Fukada and Hara for

blood vessel walls measured at the macroscopic scale, yet is comparable with the PFM measurements of other tissues. Although variation in the PFM amplitude is still observed in Figure 6.4 (b), the range of variation from 7 to 16 pm is much smaller because of the resonance tracking, suggesting that the large variation seen in Figure 6.2 (c) is not intrinsic. Such an ability to track the resonance is critical, since resonant frequency indeed varies from 260 to 285 kHz, as seen in Figure 6.4 (c), which reflects the contact stiffness changes resulting from structure heterogeneity. Variation in the quality factor, ranging from 40 to 70, is also observed, as shown in Figure 6.4 (d), and this reflects differences in energy dissipation at different locations. For all these mappings, no correlation with topography is observed, and it appears that the high piezoresponse region tends to have smaller resonant frequencies and quality factors, and thus, is softer. Little variations in phase contrast mapping is observed, as shown in Figure 6.5 (b), suggesting that the polar distribution in the probed area shows little spatial variation and exhibits no domain structures, even though large phase contrast is also observed in other areas, as shown in Figure 6.3.

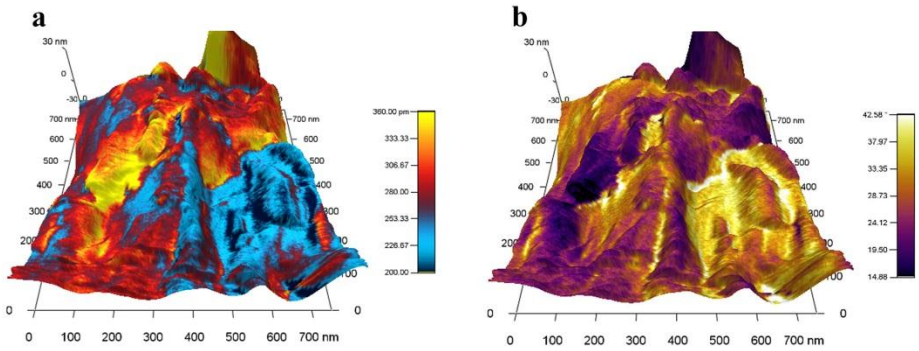

Figure 6.5 PFM mappings corresponding to those shown in Figure 6.4: (a) PFM amplitude mapping at resonance before corrected by quality factor, and (b) PFM phase mapping at resonant frequency

To verify the ferroelectricity in aortic walls, we applied a sequence of DC voltages in a triangle sawtooth form to the sample in an attempt to switch its polarization, as shown in Figure 6.6 (a), with a 3 V AC voltage simultaneously applied to measure the corresponding piezoresponse. During the switching PFM and SSPFM, two cycles of DC bias were applied, starting from negative maximum to the positive, with the period set to be 5s and each "on" and "off" steps maintained for 50 ms. The second cycle data was chosen for analysis. In order to minimize the effects of electrostatic interactions, the piezoresponse is measured during the "off" state at each step, and the phase-voltage hysteresis loop is evident, as shown in Figure 6.6 (b) for three representative loops measured at different points. Reversal in the piezoresponse phase occurs when a coercive voltage is exceeded, at approximately 8.4 V on the positive side, and -10.8V on the negative side, which are rather modest considering the thickness of the sample, and the

phase contrast is approximately 180°, a clear indication of polarization switching. Associated with the phase reversal, amplitude-voltage butterfly loops are also observed, as shown in Figure 6.6 (c), which saturates at a relatively high voltage, suggesting that the response is piezoelectric instead of electrostatic, and thus, the phase reversal does signal polarization switching and ferroelectricity.

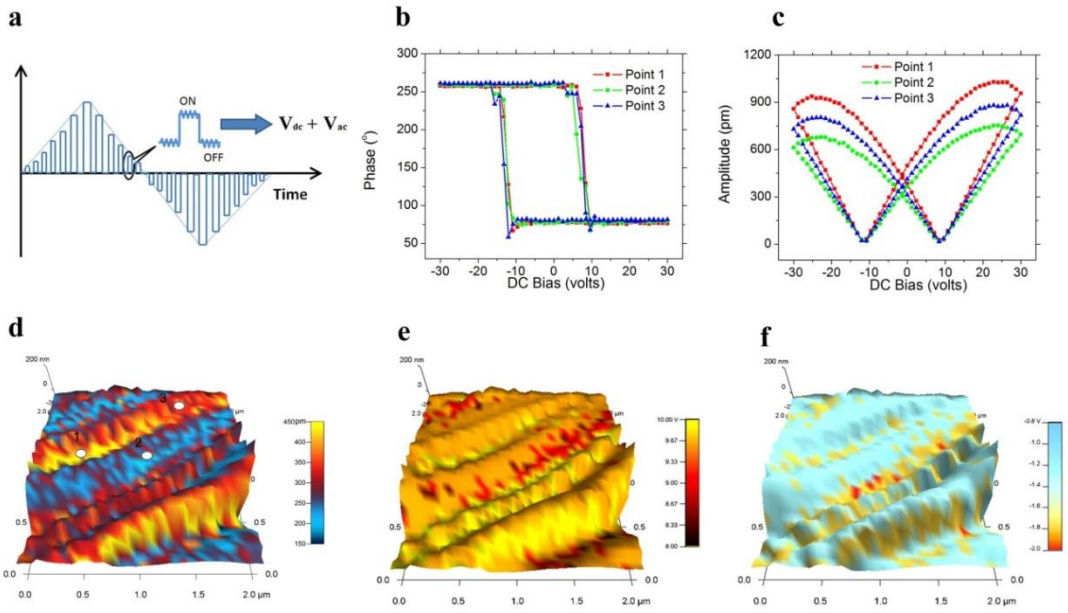

Figure 6.6 Ferroelectric switching of inner aortic wall by PFM: (a) schematics of switching PFM, (b) phase-voltage hysteresis loop, (c) amplitude-voltage butterfly loop measured at a single location, SSPFM mapping of (d) remnant PFM amplitude, (e) coercive voltage, and (f) nucleation bias in a 2×2 μm^2 area.

This is also confirmed by the corresponding loops measured during the "on" state, as shown in Figure 6.7, where the coercive voltage is substantially smaller with the help of DC voltage. The responses are more than 150% higher than those measured during the

"off" state and do not saturate at a high voltage, due to strong contributions from electrostatic interactions. The differences between "on" and "off" states are evident, confirming the phase reversal observed during the "off" state is indeed ferroelectric. In addition, the ferroelectricity of aortic walls appear to be insensitive to the structure heterogeneity at the area probed, as revealed by switching spectroscopy piezoresponse force microscopy (SSPFM) studies.

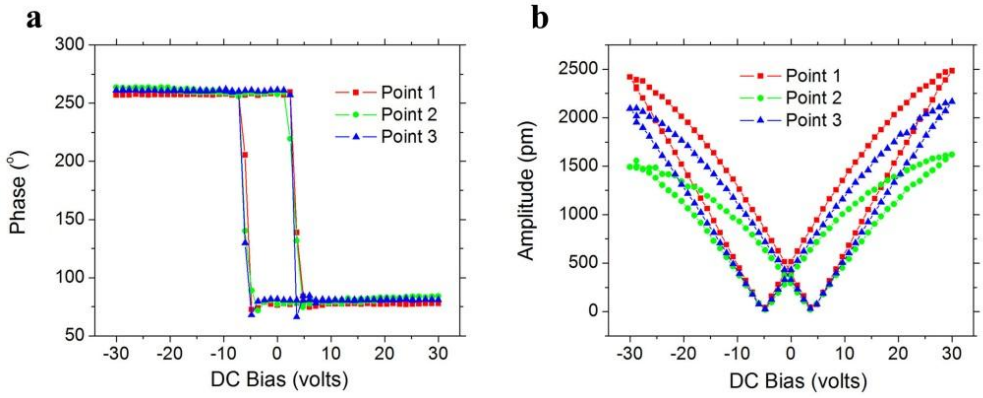

Figure 6.7 PFM phase-voltage hysteresis loop (a), and amplitude-voltage butterfly loop measured during "on" state (b), which corresponds to the loops shown in Figure 6.6.

Hysteresis and butterfly loops similar to those in Figure 6.6 (b) and (c) were obtained on a grid of 32×32 points over 2×2 um^2 area, and the resulting mapping of the piezoresponse amplitude at zero DC voltage is shown in Figure 6.6 (d), overlaid on a chain-like topographic structure consisting of fine globular features. Alternating fibrous chains with high and low piezoresponse are observed, with a high response in the range of 280-430 pm and a low response in the range of 170-220 pm. The mapping of the

coercive voltage is shown in Figure 6.6 (e), ranging from approximately 8 to 10 V with little variation, and the high response chains appear to have slightly higher coercive voltage. It is also observed from Figure 6.6 (b) and (c) that the hysteresis and butterfly loops are slightly asymmetric toward negative voltage, and the resulting piezoresponse amplitude is slightly higher at a positive saturation voltage. Such switching asymmetry appears to be common in the area probed, as shown by the mapping of nucleation bias in Figure 6.6 (f), which is defined as the average positive and negative coercive voltages obtained from SSPFM. For most of the grid points, the nucleation bias is around -1.2 V.

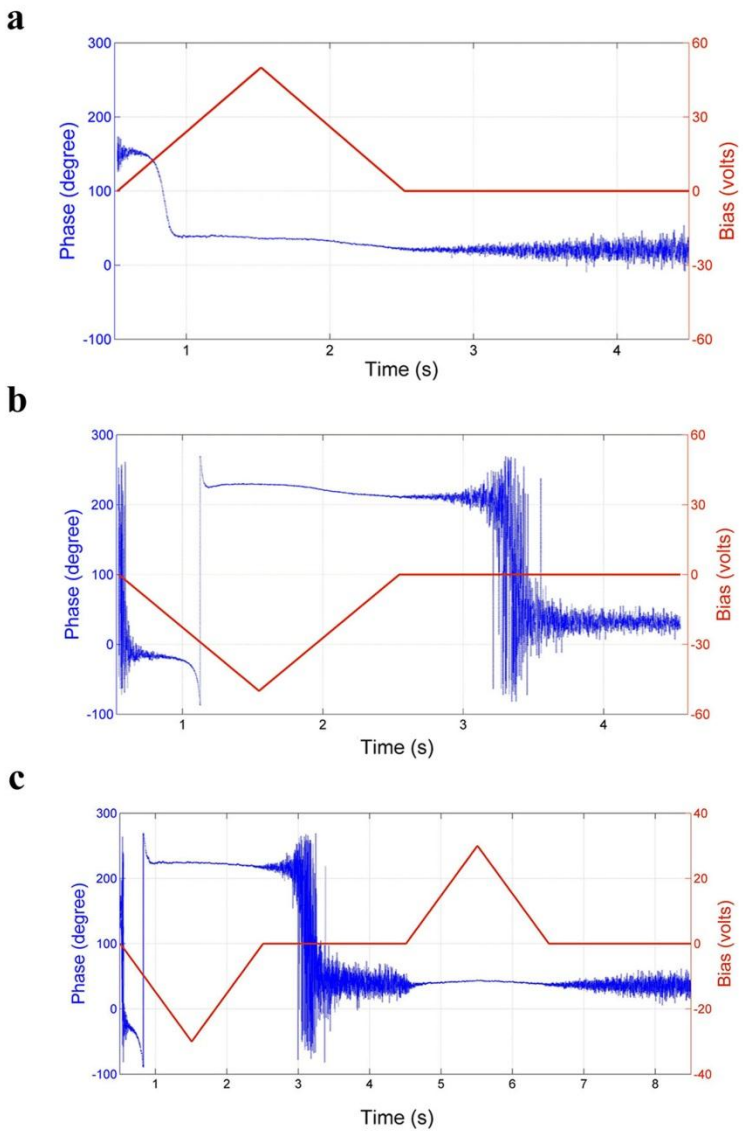

Figure 6.8 Variation of the PFM phase with respect to time under triangle DC voltages, showing relaxation and stability of polarization switched by (a) positive, (b) negative, and (c) negative and positive DC voltages.

The asymmetry in the nucleation bias during switching suggests that the polarization in the aortic wall is internally biased outward, which is consistent with the negative potential in the inner walls measured in vivo previously reported. To verify this, we

applied a sequence of triangle DC voltages, as shown in Figure 6.8, and measured the corresponding phase changes in the process, especially its relaxations after removing the DC voltage. When a positive DC voltage is applied, as shown in Figure 6.8 (a), a phase change occurs when the coercive voltage is reached, and after removal of the DC voltage, no phase flip is observed, suggesting that the polarization switched by a positive voltage is stable. On the other hand, if a negative DC voltage is applied, as shown in Figure 6.8 (b), a phase change occurs again when the coercive voltage is reached, but shortly after removal of the DC voltage, a 180^{o} phase flip is observed. This suggests that the polarization switched by a negative voltage is not stable and reverses to more stable orientation spontaneously after removal of the negative voltage. If a positive DC voltage is applied after the negative voltage, as shown in Figure 6.8 (c), then this positive voltage will not change the phase after it is reversed spontaneously, confirming that the spontaneously reversed polarization is indeed stable.

6.2 Glucose Suppresses Ferroelectric Switching in Aortic Elastins

6.2.1 Introduction

Elastin is an intriguing extracellular matrix protein present in all connective tissues of vertebrates, rendering essential elasticity to aortas, lungs, ligaments, and skins subjected to repeated physiological stresses. Long thought to be purely structural,

compelling evidence has emerged on its physiological significance for example, in vascular morphogenesis and homeostasis. Glycation of elastins naturally occurs during aging and is accelerated by elevated sugar level. It degrades structures and functionalities of elastin and is connected to aging of skins and a number of diseases, such as diabetic macroangiopathy, arteriosclerosis, and hypertensions. Using PFM, we show that elastin is ferroelectric and is switchable by an electric field, and the ferroelectricity of elastin is suppressed by glucose treatment.

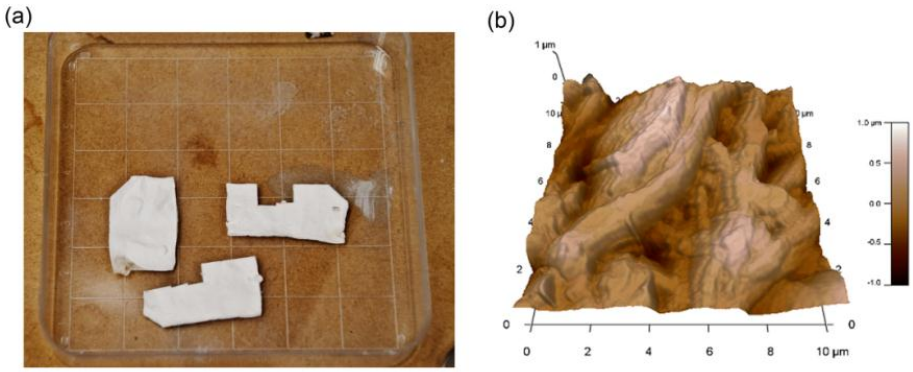

Figure 6.9 (a) Photo of a typical elastin samples, and (b) AFM topography of elastin sample.

6.2.2 PFM Experiment

Elastins were purified from thoracic aortas, as provided by Prof. Yanhang Zhang of Boston University. A photo of typical samples is shown in Figure 6.9, along with atomic force microscopy (AFM) topography mapping. It shows the hierarchical fibrous structure composed of fine globular features. Piezoresponse force microscopy (PFM) was used to

measure the piezoelectric effect of the elastin by applying an AC voltage through the conductive AFM tip to excite the piezoelectric vibration of the sample. The thickness of the PFM sample is approximately 0.62 mm.

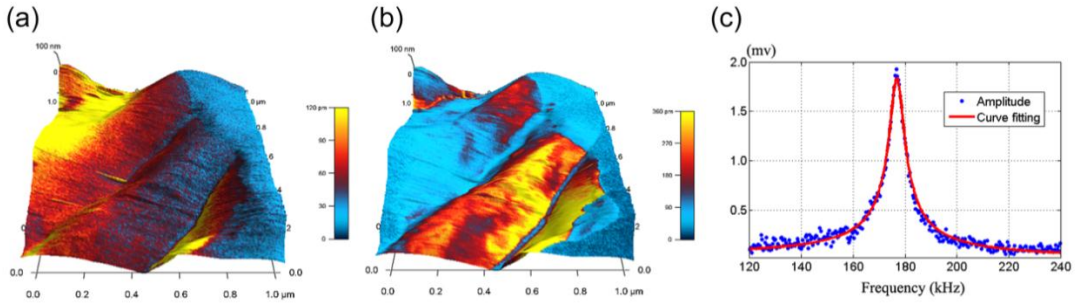

Figure 6.10 Piezoelectric response of elastin; (a) vertical and (b) lateral PFM amplitude mappings overlaid on 3D topography; (c) PFM amplitude versus driving frequency, and its fitting by damped harmonic oscillator model.

Both vertical and lateral responses were observed, with typical vertical and lateral PFM amplitude mappings overlaid on the 3D topography shown in Figure 6.10 (a) and (b). It reveals three elastin fibers approximately parallel to each other. One of the fibers shows a high vertical response of up to 120 pm with a relatively small lateral response, while the other one exhibits a high lateral response of up to 360 pm with a relatively small vertical response, suggesting their orientations are rotated with respect to each other. These responses were driven by a 5 V AC voltage near the resonance, as shown in Figure 6.10 (c), which was fitted very well by a damped harmonic oscillator model (DHOM), as the previous section discusses, yielding a quality factor of 32 and a resonant frequency of 176.9 kHz. The corrected PFM amplitude is 6.25 pm, suggesting that the

piezoelectric coefficient of elastin is in the order of 1 pm/V. The resonant frequency is smaller than the aortic walls that contain stiffer collagens, suggesting that it is much softer than expected. Such analysis is also confirmed by detailed mappings of the corrected PFM amplitude and resonant frequency derived from the dual frequency resonance tracking (DFRT) using DHOM, as exhibited in Figure 6.11.

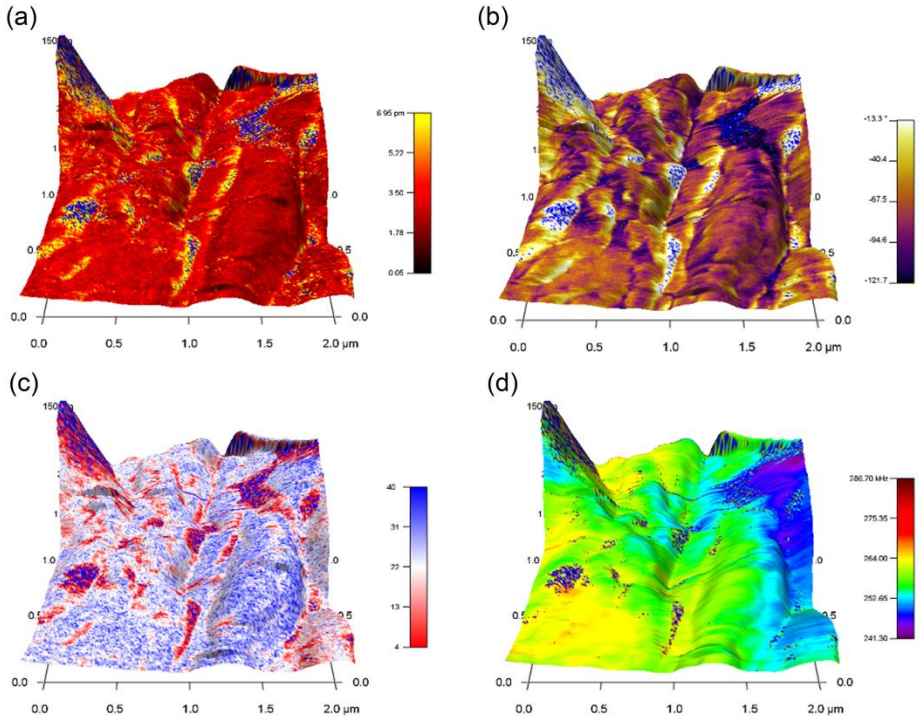

Figure 6.11 DFRT mappings of elastin obtained using 15 V AC voltage: (a) corrected amplitude, (b) phase, (c) quality factor, and (d) resonant frequency.

Switching spectroscopy piezoresponse force microscopy (SSPFM) is then carried out on the 32×32 grid points over a 10×10 μm^2 area, as shown in Figure 6.12, which demonstrates consistent ferroelectric switching throughout the region, similar to what we

observed in the aortic wall. A sequence of DC voltages of up to 80 V is applied to switch the polarization, and the corresponding PFM response is measured by a 10 V AC voltage simultaneously during the "off" state to minimize the electrostatic interactions, as schematically shown in Figure 6.12 (a). Phase-voltage hysteresis and amplitude-voltage butterfly loops characteristic of ferroelectric switching are obtained throughout the probed areas, with three representative points shown in Figure 6.12 (b) and (c). Such switching behavior is highly repeatable throughout the sample, confirming the ferroelectricity of elastin without ambiguity.

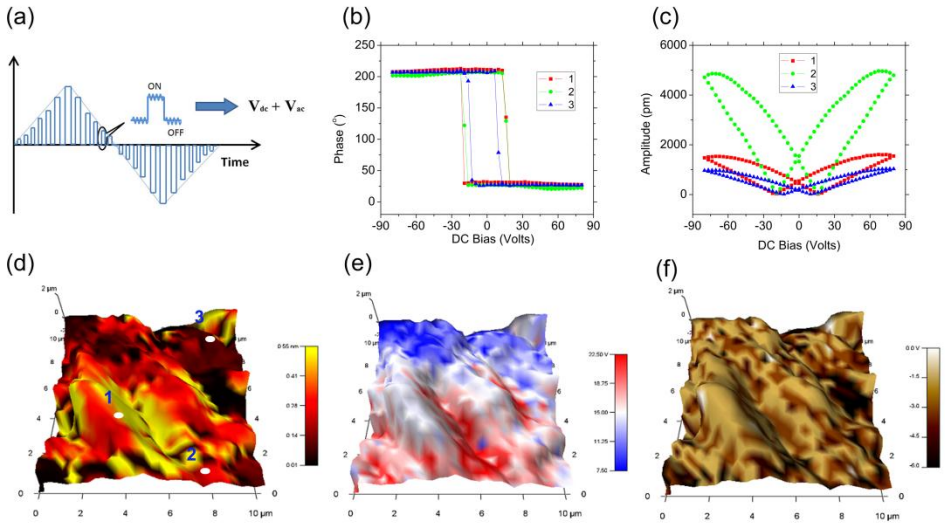

Figure 6.12 Ferroelectric switching of elastin; (a) schematics of wave form; (b) phase-voltage hysteresis loops; (c) amplitude-voltage butterfly loop; and SSPFM mapping of (d) remnant amplitude, (e) coercive voltage, and (f) nucleation bias.

In fact, no switching behavior was reported before in collagens despite several attempts. This suggests that the ferroelectricity we observed in aortic walls originates

largely from elastin, and it is reasonable to expect biological ferroelectricity in other connective tissues containing elastins, such as skins and ligaments. Indeed, detailed SSPFM mappings of elastins overlaid on the 3D topography exhibits similar characteristics as aortic walls. Fibrous chains with high and low piezoresponse are observed, as shown in Figure 6.12 (d), with high response in the range of 286-544 pm and low response in the range of 13-77 pm. The coercive voltage ranges from approximately 4 to 27 V, as seen in Figure 6.12 (e), showing larger variation than the aortic wall, even though the probed area is much larger. The nucleation bias, defined as the average of the positive and negative coercive voltages, is consistently negative, ranging from -9.6 to 0 V, with most points around -2.2 V, as shown in Figure 6.12 (f). This suggests the internal asymmetry of the polarization in elastin is similar to the aortic wall, which can also be deducted from the small asymmetry shown in the hysteresis and butterfly loops. It is also emphasized that for pure elastin, even points where the PFM amplitude is rather small, as seen in Figure 6.12 (d), can be consistently switched with characteristics like hysteresis and the butterfly loop, in sharp contrast to what we observe in glucose-treated elastin, as will be discussed next.

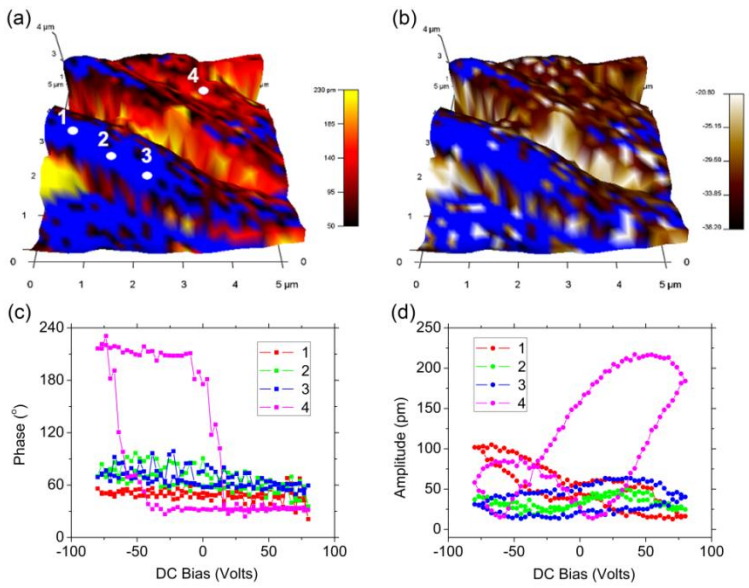

Figure 6.13 Suppression of ferroelectricity in elastin by glucose treatment; SSPFM mapping of (a) remnant amplitude and (b) nucleation bias, where points with no switching are marked by blue; (c) representative phase-voltage loops; (d) the corresponding amplitude-voltage loops.

While SSPFM mappings convincingly established consistent switching in elastins that underpin the biological ferroelectricity of aortas, we also found that such switching is largely suppressed by glucose, as seen in Figure 6.13. The SSPFM mapping of remnant polarization on a grid of 32×32 points over a 5×5 um^2 area for glucose-treated elastin is shown in Figure 6.13 (a), with the experimental parameters identical to those of Figure 6.12. While many points are switched with a relatively large PFM amplitude, large areas marked as blue are also identified, which shows no switching characteristics. This is illustrated in Figure 6.13 (c) and (d), where representative phase-voltage and amplitude-voltage loops are shown. While the point outside of blue area shows clear hysteresis and

butterfly loops, three representative points inside the blue area show very small variation in phase and rather irregular amplitude loops, indicating no switching occurs in these points. Similar observations are made throughout the blue areas, suggesting that the ferroelectricity is suppressed in these areas by glucose. Such observations are highly repeatable throughout the glucose-treated sample, as well. In fact, even for the points outside of the blue areas that are switched, the amplitude-voltage butterfly loops become highly asymmetric with much higher PFM amplitudes at positive voltages, while the corresponding nucleation bias moves toward more negative values, suggesting that the switching characteristics is substantially altered by glucose, if not completely suppressed. This is confirmed by the SSPFM mapping of the nucleation bias, shown in Figure 6.13 (b), which ranges from -20 to -38 V, much larger than those observed in untreated elastins. This suggests that glucoses seem to freeze the internal asymmetric polar structures of elastins, making it much harder to switch or suppress the switching completely.

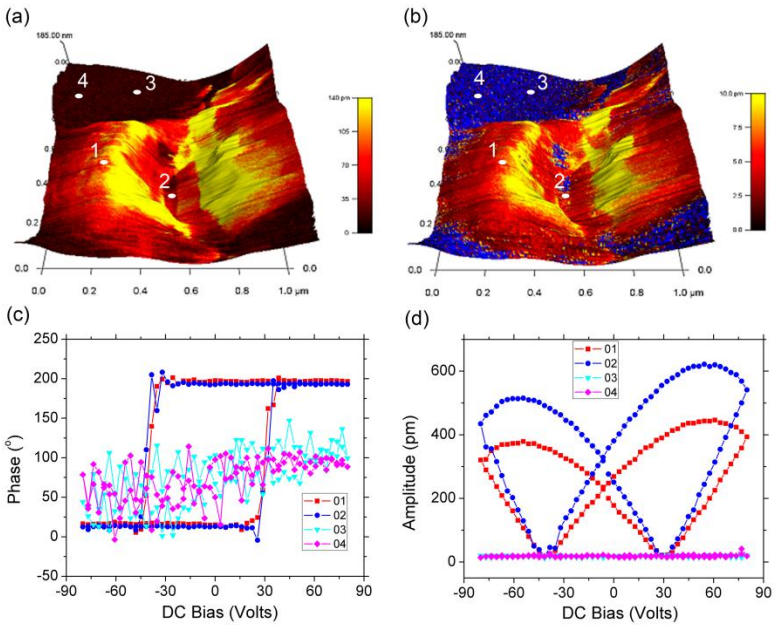

Figure 6.14 Correlation between reduced piezoresponse and suppressed ferroelectricity in glucose-treated elastin; (a) PFM amplitude mapping; (b) corrected PFM amplitude mapping by DHOM, wherein points with no solution from DHOM are marked by blue; (c) phase-voltage loops; (d) amplitude-voltage loops.

To further understand the suppression of ferroelectricity in elastins by glucose treatment and to correlate the changes of ferroelectricity to its piezoelectric response, we also carried out a detailed PFM mapping for glucose-treated elastin using DFRT with a 15 V AC voltage, as seen in Figure 6.14 (a), overlaid on a 3D topography, which shows two elastin fibers with both high and low PFM amplitudes. Interestingly, it is observed that points within high response areas exhibit clear switching characteristics, while those within low response areas are largely non-switchable, as evident in Figure 6.14 (c) and (d). Further analysis revealed that for non-switched points, the induced piezoelectric response is rather small, and it cannot be fitted by DHOM. This is evident from a

corrected PFM amplitude mapping in Figure 6.14 (b), which shows large amounts of blue points, for which DHOM yields no solution. While it is difficult to compare the piezoelectric response of elastins with and without glucose treatment quantitatively since a PFM experiment is sensitive to a number of parameters, the statistical distribution of PFM amplitude over four 1×1 μm^2 areas in respective samples can reveal valuable information, as shown in Figure 6.15. In particular, glucose treatment leads to large spikes at a very weak PFM amplitude, as small as 0.2 pm, with the intensity close to or even higher than typical PFM amplitudes of around 3~4 pm, shown in Figure 6.15 (c) and (d). In addition, the median value of PFM amplitude also appears to be reduced by glucose treatment. These suggest that glucose also alters the piezoelectric response of elastin substantially, and suppression of ferroelectricity in elastin is closely associated with the reduction of its piezoelectric response. While the detailed mechanism of loss ferroelectricity remains to be uncovered, this data suggests that the loss of ferroelectricity is closely related to the cross-link of elastin fibers, which stiffens the fibers and reduces their piezoelectricity. Indeed, it is observed that the normalized tangent modulus of elastin is increased by 31.17% - 35.39% by glucose treatment, as reported by our collaborator.

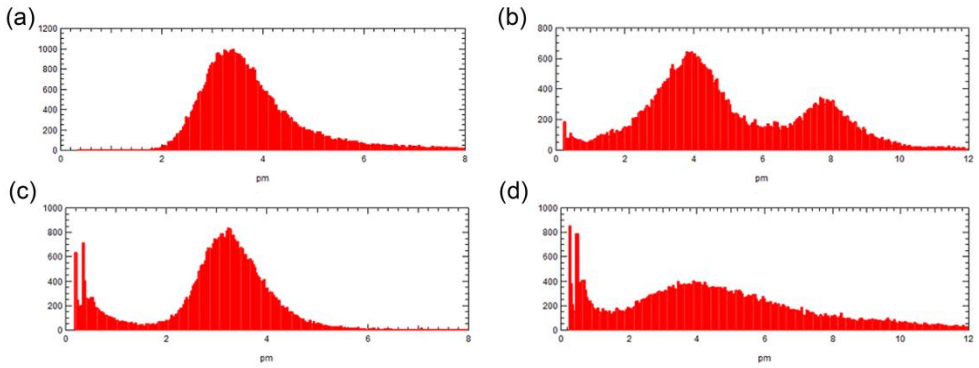

Figure 6.15 Comparison of statistical distribution of DHOM-corrected PFM amplitude over four 1×1 μm^2 regions in untreated (a and b) and glucose-treated elastin (c and d).

References

1 E. Fukada and I. Yasuda, Journal of the Physical Society of Japan **12,** 1158 (1957).

2 C. A. L. Bassett and R. O. Becker, Science **137,** 1063 (1962).

3 M. H. Shamos, M. I. Shamos, and L. S. Lavine, Nature **197,** 81 (1963).

4 M. Braden, A. G. Bairstow, I. Beider, and B. G. Ritter, Nature **212,** 1565 (1966).

5 R. W. Morris and L. R. Kittlema, Science **158,** 368 (1967).

6 E. Fukada and K. Hara, Journal of the Physical Society of Japan **26,** 777 (1969).

7 E. Fukada and H. Ueda, Japanese Journal of Applied Physics **9,** 844 (1970).

8 H. Athenstaedt, Archives of Oral Biology **16,** 495 (1971).

9 R. M. Zilberst, Nature **235,** 174 (1972).

10 T. Li and K. Zeng, Acta Materialia **59,** 3667 (2011).

11 S. B. Lang, Nature **212,** 704 (1966).

12 H. Athenstaedt, Nature **228,** 830 (1970).

13 S. B. Lang and H. Athenstaedt, Science **196,** 985 (1977).

14 H. Athenstaedt, H. Claussen, and D. Schaper, Science **216,** 1018 (1982).

15 H. Athenstaedt, Annals of the New York Academy of Sciences **238,** 68 (1974).

16 M. H. Shamos and L. S. Lavine, Nature **213,** 267 (1967).

17 A. A. Marino and R. O. Becker, Nature **228,** 473 (1970).

18 P. Boldrini, Journal of Theoretical Biology **87,** 263 (1980).

19 S. B. Lang, IEEE Transactions on Dielectrics and Electrical Insulation **7,** 466 (2000).

20 A. Gruverman and S. V. Kalinin, Journal of Materials Science **41,** 107 (2006).

21 S. V. Kalinin, A. Rar, and S. Jesse, IEEE Transactions on Ultrasonics Ferroelectrics and Frequency Control **53,** 2226 (2006).

22 S. V. Kalinin, B. J. Rodriguez, S. Jesse, E. Karapetian, B. Mirman, E. A. Eliseev, and A. N. Morozovska, in *Annual Review of Materials Research*; *Vol. 37* (Annual Reviews, Palo Alto, 2007), p. 189.

23 C. Halperin, S. Mutchnik, A. Agronin, M. Molotskii, P. Urenski, M. Salai, and G. Rosenman, Nano Letters **4,** 1253 (2004).

24 A. Gruverman, D. Wu, B. J. Rodriguez, S. V. Kalinin, and S. Habelitz, Biochemical and Biophysical Research Communications **352,** 142 (2007).

25 S. V. Kalinin, B. J. Rodriguez, S. Jesse, T. Thundat, and A. Gruverman, Applied Physics Letters **87** (2005).

26 B. J. Rodriguez, S. V. Kalinin, J. Shin, S. Jesse, V. Grichko, T. Thundat, A. P. Baddorf, and A. Gruverman, Journal of Structural Biology **153,** 151 (2006).

27 M. Minary-Jolandan and M.-F. Yu, ACS Nano **3,** 1859 (2009).

28 C. Harnagea, M. Vallieres, C. P. Pfeffer, D. Wu, B. R. Olsen, A. Pignolet, F. Legare, and A. Gruverman, Biophysical Journal **98,** 3070 (2010).

29 S. V. Kalinin, B. J. Rodriguez, S. Jesse, K. Seal, R. Proksch, S. Hohlbauch, I. Revenko, G. L. Thompson, and A. A. Vertegel, Nanotechnology **18** (2007).

Chapter 7 Summary and Future Work

7.1 Summary

In this dissertation, we have thoroughly investigated the characterization, manipulation, and engineering of synthetic and biological ferroelectrics using piezoresponse force microscopy (PFM) and nanoimprint lithography (NIL), as summarized below

In chapter2, the principle of scanning probe microscopy (SPM) is introduced briefly first, followed by detailed discussions on PFM with both vertical and lateral PFM modes. In order to enhance the piezoresponse sensitivity, the AC voltage is often driven near the resonance of cantilever-specimen system, magnifying the piezoresponse amplitude by orders of magnitude, and the newly developed dual frequency resonance tracking technique (DFRT) allows us to track resonance frequency, and enable the quantitative analysis using damped harmonic oscillator model. Furthermore, the switching of polarization by conductive SPM tip is demonstrated, making it possible to use PFM as a nanolithography tool to create designed polar structures with almost arbitrary pattern, by applying a distribution of positive and negative voltages based on pre-designed templates while scanning the sample. In addition, when a sequence of DC bias voltage is applied in addition to the AC modulation voltage, it is also possible to switch the polarity of the

ferroelectrics when its coercive field is exceeded, resulting in domain switching and the corresponding phase-voltage hysteresis and amplitude-voltage butterfly loops. After local domain switching at one location, the cantilever can be controlled to move to the next location and the process produces a mapping of switching characteristics, which is the so-called switching spectroscopy PFM (SSPFM), where the hysteresis loops are mapped at a grid of points.

In chapter 3, various PFM techniques introduced in Chapter 2 are applied to probe and manipulate inorganic perovskite ferroelectric films and crystals, including epitaxial $BiFeO_3$ thin films, and PMN-PT single crystals. These studies revealed characteristic domain structures in ferroelectric films and crystals, shed light on the domain switching dynamics under different voltages or times, and demonstrated domain evolutions at elevated temperatures. In chapter4, similar studies have been carried out for PZT thick films, PZT nanostructures patterned by soft lithography, as well as stretchable PZT ribbons on soft PDMS. In particular, the PFM results confirmed excellent piezoelectric and ferroelectric properties in patterned PZT and stretchable PZT ribbons that are comparable to the flat PZT films on rigid silicon substrates. In addition, a specific loading device is designed to stretch or compress the wavy PZT ribbons, and confirmed that the piezoelectric and ferroelectric properties of PZT ribbons are not negatively influenced by mechanical deformations, including stretching, compression, and twisting

In chapter 5, we use PFM to study P(VDF-TrFE) films. P(VDF-TrFE) thin films are deposited by spin coating, and the effects of various processing conditions are investigated. The thermal stability of P(VDF-TrFE) films are investigated, including changes in morphology and evolution of piezoresponse. It is observed that the piezoresponse of P(VDF-TrFE) films remains relatively stable up to 110^{o}C, and then drops rapidly to zero. Furthermore, a rapid nanoimprinting technique is developed to pattern P(VDF-TrFE) copolymers in just 3 minutes without any post-imprinting annealing. The effects of imprinting conditions such as the mold characteristics, temperature, and initial film thickness on the imprinted film properties have been thoroughly investigated, and the optimal imprinting parameters for excellent pattern transfer have been identified. The excellent piezoelectric and ferroelectric properties of nanoimprinted P(VDF-TrFE) structures are also confirmed by PFM mappings as well as switching PFM, and the application of the imprinted polymeric patterns as a ferroelectric nonvolatile memory for data storage has also been demonstrated and discussed.

In chapter 6, we extend the scope of PFM studies to biological systems. Using PFM, we discovered that the porcine aortic walls are not only piezoelectric, but also ferroelectric, confirmed by tip induced hysteresis and butterfly loops characteristic of polarization reversal. This is the first discovery of such phenomenon in biological tissues. Quantitative analysis based on damped harmonic oscillator model suggests that the

piezoelectric coefficient of aortic wall is in the order of 1pm/V, and switching experiments reveals that its coercive voltage is approximately 10V. Through detailed switching spectroscopy mapping, we also find that the polarization of the aortic walls is internally biased outward, exhibited by slight asymmetry in its nucleation bias. In addition, we discovered that elastin, an extracellular matrix protein present in all connective tissues of vertebrates, is switchable by an electric field, while switchability of collagen is inconclusive and requires further studies. The ferroelectricity in elastin points to possibly much wider occurrence in biology. Furthermore, it is observed that the ferroelectricity in elastin is largely suppressed by glucose, and such loss of ferroelectricity may have important physiological and pathological implications to elastin's functionalities.

In conclusion, we have applied a variety of PFM techniques for thorough characterization and manipulation of piezoelectric and ferroelectric properties at nanoscale, and nanoimprint lithography techniques have also been developed to pattern polymeric ferroelectric nanostructures. These studies have revealed intriguing ferroelectric domain structures and switching dynamics, and have led to the discovery of biological ferroelectricity in aortic walls and elastin.

7.2 Future work

Our investigation is by no means completed, and here we discuss some future research directions in studying synthetic and biological ferroelectricity by PFM:

A. 3D PFM Combining Vertical and Lateral PFM

Polarization in ferroelectric is 3D in general. To obtain complete information on polarization of materials, all three components should be obtained. Vertical PFM measures the out of plane polarization. Lateral PFM, on the other hand, allows us to probe the in-plane polarization perpendicular to cantilever axis. A third component of the polarization can be determined by rotating the sample by 90^{o} in-plane. Combining two lateral PFM and one vertical PFM, 3D PFM can be attempted with complete information on polarization distribution. This is particularly important for biological materials, which usually have lower symmetry and thus more complicated polarization distribution.

B. Band Excitation

Our current implementation of high resolution quantitative PFM relies on DFRT, and it is necessary to track resonance accurately, which is not always possible when there is a large shift. This limitation can be overcome through band excitation method based on nonsinusoidal excitation signals over a wide frequency range, eliminating the need for

resonance tracking. Compare to DRFT, band excitation can be interpreted as multiple frequency version of DRFT and will works on samples with very large changes in morphology or stiffness.

C. Fast PFM for Detailed Study of Switching Dynamics

PFM has low time resolution in general, and each PFM image takes several minutes to obtain. Domain switching, on the other hand, usually occurs with submicron second speed. As such, faster PFM mode is required for detailed study of switching dynamics. This can be accomplished by stroboscopic PFM with a step-by-step switching pulse train, wherein the voltage pulse is shorter than the total switching time, and thus it generates partial polarization reversal that is valuable to understand domain switching dynamics.

D. NIL of sub-100nm Structure

Our nanoimprinted ferroelectric structure has feature size over 100nm, and we hope to push the limit into sub-100 nm regime.. A custom designed imprinting mold with sub-100nm structures should be fabricated by E-beam lithography. The mold will then be used in NIL to fabricate one- and zero-dimensional ferroelectric nanostructures having feature size ranging from 10nm to 100nm. With such study, we hope to reveal size effects in ferroelectrics and identify the fundamental size limit of ferroelectricity in one- and zero-dimension.

E. The Origin and Significance of Biological Ferroelectricity

While we discovered biological ferroelectricity, its underlying biomolecular origin is still unclear, neither is its biological significance. All of these require much more in-depth studies, which we hope to carry out some in the future.

VITA

Yuanming Liu

Education

University of Washington in Seattle, WA Mechanical Engineering Ph.D., 2012

Tsinghua University, Beijing, P. R. China Engineering Mechanics M.S., 2006

Beijing Institute of Technology, Beijing, P. R. China Applied Mechanics B.S., 2001

Research Experience

Graduate Research Assistant (Ph.D.) at University of Washington in Seattle.
Advisor: Prof. Jiangyu Li.

Nanoscale Engineering and Characterization of Synthetic and Biologic Ferroelectrics.

* Nanoimprint lithography of ferroelectric nanostructures.
* Scanning probe microscopy study on ferroelectrics and multiferroics
* Piezoresponse force microscopy study of ferroelectric materials. (Vector PFM, DFRT, Nanolithography, SSPFM, etc.)
* High temperature PFM study on thermal variation of ferroelectric copolymers and single crystal.
* Nano-scales characterization on ferroelectrics and biomaterials (porcine artery, Elastin, mice bone).
* Coupling between nanoindentation and PFM characterization on ferroelectric materials.

Graduate Research Assistant (Master) at Tsinghua University, China.
Advisor: Prof. Daining Fang.

Study on the Electromechanical Deformation and Fatigue Behavior of Ferroelectric Materials

* Fatigue tests on Compact Tension PZT ceramic under various combinations of electric and mechanical load.
* Experiment on crack propagation of Vickers Indention under electric fields.
* Experiment on biaxial electromechanical constitutive laws.
* Phenomenological constitutive laws of domain-switching and fatigue of crack growth model on ferroelectrics.

Honors and Awards:

2009-2011 UIF fellowship, the Center for Nanotechnology, University of Washington.

2010 Best poster award of 8th International Tutorial Workshop on PFM and Nanoscale Electromechanics of Polar Materials

2008 Travel Grant of 'Joint CNMS and SHaRE User Meeting, Oak Ridge National Laboratory'

2007 Othmer Fellowship, University of Nebraska- Lincoln

2000-2001 People's Scholarship of Beijing Instituted of Technology (2nd Prize)

1998-2000 People's Scholarship of Beijing Instituted of Technology (3rd Prize)

Publications:

1. **Yuanming Liu**, Yanhang Zhang, Ming-Jay Chow, Qian Nataly Chen, and Jiangyu Li*. Biological Ferroelectricity Uncovered in Aortic Walls by Piezoresponse Force Microscopy. *Physical Review Letters* **108**, 078103 (2012) (Accompanied with a Physics Viewpoint; Selected as Featured and Editors' Suggestion paper; Also featured on NSF, Inside Science, Science Daily, New Scientist, and reproduced by many other media.)
2. **Yuanming Liu**, Shuhong Xie, Xiaoyan Liu, Kenji Kitamura, Jiangyu Li*. Thermal Variation of Piezoresponse in Microscopically Poled Poly(vinylidene fluoride-trifluoroethylene) Ferroelectric Copolymers approaching Curie Temperature. *Journal of Applied Physics,* **110,** 5, 052008 (2011)
3. **Yuanming Liu**, Dirk Weiss, Jiangyu Li*. Rapid Nanoimprinting and Excellent Piezoresponse of Polymeric Ferroelectric Nanostructures. *ACS Nano.* **4***,* 1, 83-90 (2010)
4. **Yuanming Liu**, Yunjie Wang, Ming-Jay Chow, Nataly Q. Chen, Yanhang Zhang, and Jiangyu Li*. Glucose suppresses biological ferroelectricity in arterial elastin. (submitted)
5. Xue Feng, **Yuanming Liu** (co-first author) and Jiangyu Li, et al. Flexible FeRAM by PZT on PDMS. (in preparation)
6. **Yuanming Liu,** Faxin Li and Daining Fang*. Anisotropy of Domain Switching in Pre-poled Lead Titanate Zirconate Ceramics under Multi-axial Electrical Loading. *Applied Physics Letters.* **90**, 3,032905 (2007)
7. Daining Fang*, **Yuanming Liu** *et al*. Patent: Double Shaft Force Electric Coupling Loading Driving and Charge Detecting Device. *in Chinese, CN1945266* (2007)
8. Christopher T. Nelson, Peng Gao, Jacob R. Jokisaari, Colin Heikes, Carolina Adamo, Alexander, Melville, Seung-Hyub Baek, Chad M. Folkman, Benjamin Winchester, Yijia Gu, **Yuanming Liu**, Kui Zhang, Enge Wang, Jiangyu Li, Long-Qing Chen, Chang-Beom Eom, Darrell G. Schlom, Xiaoqing Pan*. Domain Dynamics During Ferroelectric Switching. *Science.* **334**, 968 (2011)
9. Peng Gao, Christopher T. Nelson1, Jacob R. Jokisaari1, Yi Zhang, Seung-Hyub Baek, Chung Wung Bark, Enge Wang, **Yuanming Liu**, Jiangyu Li, Chang-Beom Eom, Xiaoqing Pan1*. Direct Observations of Retention Failure in Ferroelectric Memories. *Advanced Materials*. **24**, 8, 1106 (2012)
10. Xue Feng*, Yang Byung Duk, **Yuanming Liu**, *et al*. Stretchable Ferroelectric Nanoribbons with Wavy Configurations on Elastomeric Substrates. *ACS Nano.* **5,** 4, 3326-3332 (2011)
11. Shuhong Xie, Anil Gannepalli, Qian Nataly Chen, **Yuanming Liu**, Yichun Zhou, Roger Proksch and Jiangyu Li*. High Resolution Quantitative Piezoresponse Force Microscopy of BiFeO3 Nanofibers with Dramatically Enhanced Sensitivity. *Nanoscale.* **4**, 2, 408-413 (2012)
12. Qian Nataly Chen, Yanyi Liu, **Yuanming Liu**, Shuhong Xie *et al*. Direct Observation of Enhanced Li-ion Intercalation in $LiFePO_4$ Nanocrystals with Controlled Crystallinity. *Applied Physics Letters* (in press)
13. Shuhong Xie, Jiangyu Li*, Roger Proksch, **Yuanming Liu**. Nanocrystalline multiferroic $BiFeO_3$ ultrafine fibers by sol-gel based electrospinning. *Applied Physics Letters.* **93**, 22, 222904 (2008)
14. Xiaoyan Liu; Kenji Kitamura, **Yuanming Liu**, *et al.* Thermal-induced Domain Wall Motion of Tip-

inverted Micro/nanodomains in Near-stoichiometric $LiNbO_3$ Crystals. *Journal of Applied Physics.* **110**, 5, 052009 (2011)

15. Shuhong Xie, Feiyue Ma, **Yuanming Liu**, *et al*. Multiferroic $CoFe_2O_4$-$Pb(Zr_{0.52}Ti_{0.48})O_3$ Core-shell Nanofibers and Their Magnetoelectric Coupling. *Nanoscale,* **3***,* 8, 3152-3158 (2011)
16. Shuhong Xie, **Yuanming Liu**, Xiaoyan Liu, Qifa Zhou, *et al*. Local Two-way Magnetoelectric Couplings in Multiferroic Composites via Scanning Probe Microscopy. *Journal of Applied Physics.* **108**, 5, 054108 (2010)
17. Feiyue Ma, Yun Ou, Yang Yang, **Yuanming Liu***, et al.* Nanocrystalline Structure and Thermoelectric Properties of Electrospun $NaCo_2O_4$ Nanofibers. *Journal of Physical Chemistry C.* **114***, 50,* 22038-22043 (2010)
18. Xiaoyan Liu, **Yuanming Liu**, Takekawa S. *et al*. Nanopolar Structures and Local Ferroelectricity of $Sr_{0.61}Ba_{0.39}Nb_2O_6$ Relaxor Crystal Across Curie Temperature by Piezoresponse Force Microscopy. *Journal of Applied Physics.* **106**, 12, 124106 (2009)
19. Faxin Li, Daining Fang* and **Yuanming Liu**. Domain Switching Anisotropy in Poled PZT Ceramics Under Orthogonal Electromechanical Loading. *Journal of Applied Physics.* **100,** 8, 084101(2006)